ABSTRACT

Title of dissertation: DIRECT NUMERICAL SIMULATIONS OF TRANSITIONAL PULSATILE FLOWS IN STENOTIC VESSELS

Nikolaos Beratlis
Doctor of Philosophy, 2008

Dissertation directed by: Professor Elias Balaras
Department of Mechanical Engineering

In the present work a numerical study of transitional pulsatile flow through planar and cylindrical constrictions is presented. First, a simulation carefully coordinated with an experiment is carried out for validation purposes and results are in good agreement with the experiment. The parametric space that we adopted is similar to the one reported in a variety of past experiments relevant to the flow through stenosed arteries. In general, the flow just downstream of the constriction is dominated by the dynamics of the accelerating/decelerating jet that forms during each pulsatile cycle. It is found that the disturbance environment upstream of the stenosis has an effect on the spatial and temporal localization of the transition process in the post-stenotic area. The flow in the reattached area further downstream, is also affected by the jet dynamics. A 'synthetic', turbulent-like, wall-layer develops, and is constantly supported by streamwise vortices that originate from the spanwise instabilities of the large, coherent structures generated by the jet. The relation of these structures to the phase-averaged turbulent statistics and the turbulent kinetic

energy budgets is discussed. The flow physics in the cylindrical configuration are qualitatively similar to those in the planar cases. The effect of blood rheology on the flow characteristics is also assessed by employing a biviscosity model in the simulations and it is found not to have a big effect on the turbulent intensities.

DIRECT NUMERICAL SIMULATIONS OF TRANSITIONAL PULSATILE FLOWS IN STENOTIC VESSELS

by

Nikolaos Beratlis

Dissertation submitted to the Faculty of the Graduate School of the
University of Maryland, College Park in partial fulfillment
of the requirements for the degree of
Doctor of Philosophy
2008

Advisory Committee:
Professor Elias Balaras, Chair/Advisor
Professor Kenneth Kiger
Professor Richard V. Calabrese
Professor Panos Dimitrakopoulos
Professor Arnaud Trouvé

Acknowledgment

I would like to express my sincere gratitude to my advisor, Prof. Elias Balaras for his help during my graduate studies at the university of Maryland. During my Ph.D. adventure he has guided me through my academic and professional choices and helped me overcome difficulties.

I would also like to thank the members of the committee, Prof. Kenneth Kiger, Prof. Richard V. Calabrese, Prof. Panos Dimitrakopoulos, Prof. Arnaud Trouvé for reading this dissertation and offering many constructive comments. To Prof. Kiger in particular, many thanks for helping me early on during my Ph.D. project with the coordination of the simulations with the experiment and also providing guidance on the analysis of the flow.

I would also like to thank Prof. Piomelli for teaching me three courses in fluid mechanics and numerical simulations. His lectures were very interesting and I learned a lot of things that I used in my research. To Prof. Wallace, for his course in physics of turbulence.

My thanks to my colleagues; Dr. Viktor Ovchinnikov for giving us the subroutine for the synthetic noise, to Dr. Senthilkumaran Radhakrishnan for so patiently helping me with programming and linux difficulties I had throughout my Ph.D. studies and to Marcos Vanella for his help in the golfball project and mainly valuable discussions and support in the office.

Table of Contents

List of Figures iv

List of Abbreviations x

1 Introduction 1
1.1 Turbulence in Biological Flows . . . 1
1.2 Relevance of Hemodynamics to Atherosclerosis . . . 5
1.3 Flow in Stenotic Vessels: State of the Art . . . 9
1.4 Outline . . . 13

2 Methodologies 15
2.1 Mathematical model . . . 15
2.2 Numerical Methods . . . 15
2.3 Poisson Solver . . . 18
2.4 Embedded Boundary Method . . . 19
2.5 Parallelization of Code . . . 24

3 Computational setup and validation 30
3.1 Experiment . . . 30
3.2 Computational setup . . . 35
3.3 Coordination between experiments and simulations . . . 38
3.4 Comparison and grid resolution . . . 43
3.5 Inflow conditions for the axisymmetric configuration . . . 54

4 Flow Physics 60
4.1 Parametric Space . . . 60
4.2 Planar Configuration . . . 64
4.2.1 Instantaneous Flow Dynamics . . . 64
4.2.2 Statistics and budgets . . . 79
4.3 Axisymmetric configuration . . . 86
4.3.1 Instability of the start-up structure . . . 88
4.3.2 Initial stages of the non-linear instability . . . 99
4.3.3 Phase averaged statistics . . . 105

5 Blood Rheology 113
5.1 Validation of non-Newtonian model in Laminar Flows . . . 118
5.2 DNS of Non-Newtonian fluid downstream of an Axisymmetric Stenosis 121

6 Summary and conclusions 125

Bibliography 129

List of Figures

1.1 Schematic showing a large artery with atherosclerosis. Lipids and monocytes transported by the blood in the lumen are recruited in the endothelium leading to the formation of fatty streaks and lesions. Migration and proliferation of smooth muscles cells are responsible for intimal thickening, a key characteristic of lesion-prone regions. . . 6

2.1 Collocation points of velocity in a) Cartesian grid cell; b) cylindrical grid cell . . 17

2.2 A set of equally spaced marker points are use to describe the interface of the immersed body. The fluid is always to the left of the solid as one moves in the direction of increasing parameter s 20

2.3 Generalized interpolation stencil 23

2.4 Schematic representation of domain redistribution in cylindrical coordinates. . . 26

2.5 Parallel scaling of the code for various grids 28

3.1 Schematic of the experimental setup. 32

3.2 (a) Geometrical parameters that define the stenosis. (b) Waveform of $U_b(t)$: --- cases 1 and 2; —— perfect sinusoid. 36

3.3 Grid spacing versus coordinate for (a) streamwise direction and (b) wall normal direction. The stenosis is located at $x/h = 0$. 37

3.4 Present experimental results. (a) Reynolds number variation during the pulsatile cycle: ∘ experiment; --- theoretical prediction based on a purely sinusoidal pressure gradient. (b) Profiles of the axial velocity, $\tilde{u}$, at $x/H = -10$. (c) Profiles of u''_{rms} at $x/H = -10$. ∘ , $\hat{t}_1 = 2\pi$; ▫ $\hat{t}_2 = 0.86\pi$; × , $\hat{t}_3 = 1.52\pi$; ◇ , $\hat{t}_4 = 2\pi$. 39

3.5 (a) z-locations of the inflection points of the streamwise velocity profiles at the inflow plane as a function of the phase angle; (b) profiles of u''_{rms} at $x/H = -13$ for instances in the cycle noted by the vertical lines in (a). ∘ , $\hat{t}_1 = 0.9\pi$; ▫ , $\hat{t}_2 = 1.3\pi$; ◇ , $\hat{t}_3 = 1.75\pi$ 41

3.6 Phase-averaged statistics of the streamwise velocity at $\hat{t} \sim 3/2\pi$. ∘ experiment, —— Case 1, --- Case 2. (a) $\tilde{u}$; (b) u''_{rms}. 44

3.7 Phase-averaged statistics of the streamwise velocity at $\hat{t} \sim 2\pi$. ∘ experiment, —— Case 1, --- Case 2. (a) $\tilde{u}$; (b) u''_{rms}. 46

3.8 Phase-averaged statistics of the streamwise velocity at $\hat{t} \sim \pi$. $\circ$ experiment, —— Case 1, --- Case 2. 48

3.9 Spatiotemporal evolution of the phase-averaged statistics of (a) $< U > /U_m$ and (b) u''_{rms}/U_m at $x/h = 4$. ····· present experiment; —— case 1. Index values for the contour levels of $< U > /U_m$ are given by A=-0.18; B=0.38; C=0.76; D=1.13; E=1.15; F=1.89; G=2.26; H=2.63; I=3.01 50

3.10 Spatiotemporal evolution of the phase-averaged statistics of (a) $< U > /U_m$ and (b) u''_{rms}/U_m at $x/h = 12$. ····· present experiment; —— case 1. Index values for the contour levels of $< U > /U_m$ are given by A=0.23; B=0.46; C=0.70; D=0.97; E=1.16; F=1.40; G=1.62; H=1.85 51

3.11 Autoregressive power spectra at $x/h = 4$ for segment of U between $t/T = 0.80 - 0.90$. —— case 1; --- present experiment. (a) $z/h = -0.5$ and (b) $z/h = 0.5$. In both cases the kinetic energy in the segment has been used for normalization. . 51

3.12 Time average velocity statistics at $x/H = 2$, $x/H = 4$, $x/H = 6$. ····· Case A; —— Case B; —·— Case C; --- Case D. 54

3.13 Phase-averaged statistics of the streamwise velocity at $t/T = 0.25$. —·— Case 6A, —— Case 6B, --- Case 6C. (a) $\tilde{u}$; (b) u''_{rms}. 58

3.14 Phase-averaged statistics of the streamwise velocity at $t/T = 0.42$. —·— Case 6A, —— Case 6B, --- Case 6C. (a) $\tilde{u}$; (b) u''_{rms}. 58

3.15 Phase-averaged statistics of the streamwise velocity at $t/T = 0.70$. —·— Case 6A, —— Case 6B, --- Case 6C. (a) $\tilde{u}$; (b) u''_{rms}. 59

4.1 Filled iso-contours of spanwise vorticity and velocity streamlines for case 1 at four instances during the acceleration (a-d) and detailed iso-contour lines of spanwise vorticity following the downstream edge of the vortex sheet (e-h). The dotted line in (e-h) represents the iso-contour of zero spanwise vorticity. (from top to bottom (a,e); $t/T = 0.23$, (b,f); $t/T = 0.28$, (c,g); $t/T = 0.32$, (d,h); $t/T = 0.36$). 65

4.2 Selected iso-contours of spanwise vorticity and velocity streamlines at a characteristic instance during the initial shear layer roll-up. The dotted line represents the iso-contour of zero spanwise vorticity. (a) case2, $U_{red} = 6.6$, $t/T = 0.41$; (b) case3, $U_{red} = 26.5$, $t/T = 0.32$; (c) case5, $U_{red} = 53.1$, $t/T = 0.26$; (d) case4, $U_{red} = 106.2$, $t/T = 0.26$. 67

4.3 Early stages of the formation and evolution of coherent spanwise structures in case 1 visualized by iso-surfaces of Q. The time instants for the left and right parts correspond to the ones shown in figures 4.1c and d respectively. Selected contours of $(dU/dy)h/U_m$ are shown at a slice through the vortex in (a). Values of contours are ± 0.1, ± 0.2, ± 0.3 and ± 0.4, with negative values represented by dotted lines. Only the bottom half of the channel is shown and filled iso-contours of $\omega_x h/U_m$ are plotted on the wall. 68

4.4 (a) A snapshot of the dominant coherent structures in case 1 visualized by iso-surfaces of Q, shortly before the maximum flowrate ($t/T = 0.4$). Only the bottom half of the channel is shown and iso-contours of streamwise vorticity, $\omega_x h/U_m$ are plotted on the wall. (b)-(c) Instantaneous distribution of $\omega_x h/U_m$ at the two y-z planes indicated on part (a) of the figure. In-plane, instantaneous velocity vectors are also shown. Arrows in all parts of the figure point to the hairpin-like structures. 69

4.5 Spanwise averaged turbulent kinetic energy (case 1). Streamwise variation at $z/h = -0.5$ at three instances in the pulsatile cycle: —— $t/T = 0.4$; - - - $t/T = 0.45$; —·— $t/T = 0.5$ 72

4.6 Iso-contours of instantaneous spanwise vorticity ($\omega_y h/U_m$) at two instances during the deceleration in case 1; $t/T = 0.58$ (a), $t/T = 0.77$ (b) and plot of $\omega_y h/U_m$ on the bottom wall at $t/T = 0.58$ (c). 73

4.7 A snapshot of the dominant coherent structures in case 1 visualized by iso-surfaces of Q at $t/T = 0.58$. Only the bottom half of the channel is shown and iso-contours of streamwise vorticity, $\omega_x h/U_m$ are plotted on the wall. (b)-(c) Instantaneous distribution of $\omega_x h/U_m$ at the two y-z planes in the braid regions marked on part (a) of the figure. 74

4.8 Iso-contours of the instantaneous velocity fluctuations, u''/U_m, at an x-y plane above the bottom wall ($z/h = 0.1$) at a characteristic instances after the maximum flow rate for each case(from top to bottom: case1; $t/T = 0.75$, case2; $t/T = 0.75$, case3; $t/T = 0.5$ and case4; $t/T = 0.75$). 75

4.9 Vortex shedding frequencies vs phase in cycle for case 1: ▫ 'slotting' technique from the wall-normal velocity signal at $x/h = 2$ and $z/h = 0.5$; —— theoretical values based on thickness and velocity difference across the shear layer at $x/h = 0.5$. . 76

4.10 (a) Scatter plot of u''/U_m, w''/U_m events in case 1 at location $x/h = 17$ and $z/h = 0.1$; (b) The quadrant decomposition of the Reynolds shear stress, $\widetilde{u''w''}$, across the channel at the $x/h = 17$. —— Q_1: 1^{st} quadrant $(u'' > 0, w'' > 0)$; - - - Q_2: 2^{nd} quadrant $(u'' < 0, w'' > 0)$; —·— Q_3: 3^{rd} quadrant $(u'' < 0, w'' < 0)$; ····· Q_4: 4^{th} quadrant $(u'' > 0, w'' < 0)$. For both parts $t/T = 0.025$. 78

4.11 Contours of $\tilde{k}/U_m^2$ for a) $x/h = 4$, b) $x/h = 12h$, and c) $x/h = 20$, and $\widetilde{u''w''}/U_m^2$ for d) $x/h = 4$, e) $x/h = 12h$, and f) $x/h = 20$ for case 1 plotted in t/T versus z/h space. 81

4.12 Budgets of the phase-averaged turbulent kinetic energy for case 1 at $t/T = 0.5$ for three downstream locations (a) $x/h = 4.8$, b) $x/h = 9.2$, and c) $x/h = 17.0$. The terms are shown as follows: $\circ$ P_k; ····· ϵ_k; - - - T_k; —— C_k; —·— $\partial k/\partial t$. 82

4.13 Budgets of the phase-averaged turbulent kinetic energy for case 1 at $t/T = 0.75$ for three downstream locations (a) $x/h = 4.8$, b) $x/h = 9.2$, and c) $x/h = 17.0$. The terms are shown as follows: $\circ$ P_k; ····· ϵ_k; - - - T_k; —— C_k; —·— $\partial k/\partial t$. 83

4.14 (a) near wall maxima of the phase-averaged turbulent kinetic energy and (b) turbulent kinetic energy production as a function of time at $x/h = 14$ downstream of the mean reattachment point, —— ; case 2 ($Re = 600$, $U_{red} = 6.6$), - - - ; case 3 ($Re = 600$, $U_{red} = 26.5$), —·— ; case 4 ($Re = 600$, $U_{red} = 106.2$), ····· ; case 5 ($Re = 1200$, $U_{red} = 53.1$). 87

4.15 Filled iso-contours of spanwise vorticity and velocity streamlines for case 6 at three instances during the acceleration (a-c) and detailed iso-contour lines of spanwise vorticity following the downstream edge of the vortex ring (d-f). The dotted line in (d-f) represents the iso-contour of zero azimuthal vorticity. (from top to bottom (a,d); $t/T = 0.14$, (b,e); $t/T = 0.24$, (c,f); $t/T = 0.31$. 89

4.16 (a) Iso-contours of axial vorticity fluctuations for case 1 at $x/R = 14$, (b) Auto-variance of the radial velocity fluctuations at$x/R = 14$, $r/R = 0.75$. Both plots correspond to phase $t/T = 0.31$ 91

4.17 3D representation of the shear layer and the roll-up at $t/T = 0.31$. Iso-contours of the azimuthal vorticity at ($\omega_\theta = 9.2$) are shown in white color, while isocontours of axial vorticity at $\omega_x = 3.5$ are shown in red and blue color. 91

4.18 Iso-contours of (a) total rate of change of ω_x, stretching and reorientation of ω_z in (b) radial (c) azimuthal and (d) axial direction r/θ plane slicing at $x/R = 13.85$ at $t/T = 0.31$. 92

4.19 Iso-contours of the Q criterion colored by axial vorticity. On the background are plotted contours of azimuthal vorticity at selected r-z planes. From top to bottom the phase in the cycles are (a) $t/T = 0.35$, (b) $t/T = 0.36$, (c) $t/T = 0.37$ and (d) $t/T = 0.38$ 94

4.20 Filled iso-contours of spanwise vorticity and velocity streamlines for (a) cases 1 at $t/T = 0.15$ and (b) case 3 at $t/T = 0.25$. 97

4.21 Auto-variance of the radial velocity fluctuations at early stages of the shear layer roll-up (a) case 1: $t/T = 0.35$ and $x/R = 0.80$, $r/R = 0.55$; (b) case 3: $t/T = 0.35$ and $x/R = 0.25$, $r/R = 0.50$. 97

4.22 Iso-contours of the Q criterion colored by axial vorticity. On the background are plotted contours of azimuthal vorticity at selected r-z planes. On the right of each figure are plotted the velocity vectors superimposed on contours of axial vorticity on a selected $r - \theta$ plane at a x/R location indicated by the black line. From top to bottom the phase in the cycles are $t/T = 0.37$ and $t/T = 0.95$ respectively. . . 98

4.23 Iso-contours of the Q criterion colored by axial vorticity at $t/T = 0.25$. On the background are plotted contours of azimuthal vorticity at selected r-z planes. . . 99

4.24 A representative picture of the shear layer instability at $t/T = 0.92$. (a) Iso-contours of the Q criterion colored by axial vorticity and contours of azimuthal vorticity at selected r-z planes on the background. (b) Contours of radial vorticity at $r - \theta$ plane at $x/R = 8$ cutting through the second vortex ring. (c) Auto-covariance of the radial vorticity fluctuations at $x/R = 8.0$ and $r/R = 0.5$. (d) Power spectra of the axial vorticity fluctuations at $x/R = 8.0$ and $r/R = 0.5$. . . 100

4.25 Selected iso-contour of the Q criterion colored by axial vorticity and contours of azimuthal vorticity at selected r-z planes on the background at (a) $t/T = 0.93$ and (b) $t/T = 0.94$ 101

4.26 Selected iso-contour of the Q criterion colored by axial vorticity and contours of azimuthal vorticity at selected r-z planes on the background at (a) $t/T = 0.94$ and (b) $t/T = 0.95$ 102

4.27 Phase-averaged turbulent kinetic energy (case 6). Streamwise variation at r/R=0.5 at four phases in the pulsatile cycle: - - - $t/T = 0.40$; —·— $t/T = 0.45$; ····· $t/T = 0.50$; ——— $t/T = 0.70$ 103

4.28 Selected iso-contour of the Q criterion colored by axial vorticity and contours of azimuthal vorticity at selected r-z planes on the background at $t/T = 0.13$ 103

4.29 Contours of $\tilde{k}/U_m^2$ for a) $x/h = 10$, b) $x/h = 20h$, and c) $x/h = 32$, and $\widetilde{u''w''}/U_m^2$ for d) $x/h = 10$, e) $x/h = 20h$, and f) $x/h = 32$ for case 6 plotted in t/T versus z/h space. 105

4.30 (a) near wall maxima of the phase-averaged turbulent kinetic energy and (b) turbulent kinetic energy production as a function of time at $x/R = 16$ downstream of the mean reattachment point, ——— ; case 7 ($Re = 600$, $U_{red} = 6.6$), - - - ; case 6 ($Re = 600$, $U_{red} = 26.5$), —·— ; case 8 ($Re = 1200$, $U_{red} = 26.5$). 111

4.31 Spatio-temporal evolution of the phase-averaged statistics of the skin friction coefficient. (a) $\tilde{c}_f$; (b) c_f''. The dashed line corresponds to $\tilde{c}_f = 0$. 112

5.1 Viscosity dependence on shear rate for various levels of hematocrit (H). In blood with no red cells the shear rate is constant. As the percent of hematocrit increases blood behaves as non-Newtonian fluid. From [10]. 116

5.2 Blood viscosity dependence on red cell deformability. NP=normal red blood cells in plasma; NA=normal red blood cells in 11% albumin to prevent formation of *rouleaux*; HA = hardened red blood cells in 11% albunim to prevent deformation of cells. From [9]. 117

5.3 Relative turbulent intensities 20 diameters downstream of a sharp stenosis as a function of hematocrit at various Reynolds numbers. From [55]. 119

5.4 Comparison of of the axial velocity profiles (Beratlis; -, Nakamura; .) at three locations; $x/R = 1$, $x/R = 4$, and $x/R = 8$. a) Re=20, He=0 (Newtonian) b) Re=20, He=376 (biviscosity model). 120

5.5 Contours of azimuthal vorticity normalized by the bulk velocity and radius of the pipe averaged over time and azimuthal direction in $r - x$ space. The Reynolds number in both cases is 320. a) non-Newtonian b) Newtonian case. 122

5.6 Contours of axial turbulent intensity normalized by the bulk velocity averaged over time and azimuthal direction in $r - x$ space. The Reynolds number in both cases is 320. a) non-Newtonian b) Newtonian case. 122

NOMECLATURE

Abbreviations

DNS	Direct Numerical Simulations
LES	Large Eddy Simulations
LDV	Laser Doppler Velocimetry
MHV	Mechanical Heart Valve

Roman symbols

C_k	convection of turbulent kinetic energy
D_k	diffusion of turbulent kinetic energy
h	Half-channel height
H	Channel height
k	turbulent kinetic energy
K	non-dimensional amplitude of oscillations ($K = U_{max}/U_m$)
P_k	production of turbulent kinetic energy
R	Radius of pipe
Re	Reynolds number ($Re = Uh/\nu$)
Re_m	Reynolds number based on time-averaged bulk velocity
T	period of pulsation
T_k	turbulent transport of turbulent kinetic energy
U_m	time-averaged bulk velocity
U_{max}	maximum bulk velocity
U_{red}	Reduced velocity $U_{red} = U_m T/h$

Greek symbols

α	Womersley number
ϵ_k	dissipation of turbulent kinetic energy
ν	kinematic viscosity
Π_k	transport of turbulent kinetic energy by pressure velocity correlations

Superscripts and subscripts

$\bar{()}$	Time-averaged quantity
$\tilde{()}$	Phase-averaged quantity
$()'$	Fluctuation from the time-averaged mean
$()''$	Fluctuation from the phase-averaged mean
$()_{rms}$	Root-mean-square of a variable

Chapter 1

Introduction

1.1 Turbulence in Biological Flows

The study of blood flow in the circulatory system is a very challenging task in part due to its highly dynamic and variable nature. While blood flow under normal physiologic conditions is most likely to remain laminar, there are situations in which transitional and turbulent flow patterns may appear. Transition to a turbulent or quasi-turbulent state depends on the local geometry of the arterial tree, and two main non-dimensional numbers: the Reynolds and Womersley number. The Reynolds number ($Re = U_m R/\nu$) usually based on the mean velocity inside the blood vessels U_m, the radius of the vessels, R, and the kinematic viscosity of the blood, is a measure of the ratio of inertial forces to viscous forces. The Womersley number ($\alpha = R\sqrt{\omega/\nu}$) takes into account the pulsing frequency of the heart, ω, and measures the ratio of unsteady to viscous effects. Some of the early work demonstrating that turbulence can be generated in the circulatory system was carried out by Nerem and co-workers in the 70s [36, 35, 52]. In their experiments they used a hot-film anemometer system, suitable for use within the arteries, to measure in vivo the velocity of blood inside the aorta of dogs. The Reynolds number based on the peak centerline velocity and the diameter of the aorta varied from 1200 to 5400, while the Womersley number varied from 5.2 to 20.2. They classifieds the signals, by

visual inspection into three types: those with negligible high-frequency components were termed undisturbed and were representative of laminar flow. Those with high frequency components present only at the peak systolic velocity were termed disturbed and were thought to represent a transitional state. Those with high frequency components persisting throughtout the deceleration phase of the systole were termed highly disturbed and were thought to be representative of turbulence. To quantify the differences between laminar and turbulent conditions they computed the power spectra of the velocity fluctuations. For the case of laminar flow only 0.01% of the energy was contained at higher harmonics, while for the highly disturbed flow conditions the figure was 0.25%. They also observed that for lower Reynolds numbers, disturbed flow was only present in the ascending part of the aorta while in the descending part the flow remained laminar. Thus, they speculated that at these conditions the disturbances were most probably originating from the heart, perhaps from the vortex that forms in the ventricle during filling or disturbances around the cups of the aortic valve. As the Reynolds number increased, disturbances were observed both in the ascending and descending part of the aorta and were generated anew with each heart beat. They speculated that for these conditions turbulence originates from an instability in the aortic boundary layers associated with inflection points in the velocity profiles during deceleration. This hypothesis was also supported by the fact that the Reynolds number was close to or larger than the critical Reynolds number predicted by stability theory for a decelerating boundary layers.

Common occurrences of turbulence and disturbed flow patterns in the circu-

latory system are usually associated with diseased conditions (i.e. atherosclerosis) or medical implants such as mechanical heart valves (MHV), stents, etc. In MHV, for example, highly disturbed flow downstream of the devices has been reported [62]. For the case of a valve with caged-ball design, the flow that goes through the annulus and around the ball forms a circumferential shear jet that separates behind the ball forming a wake that becomes turbulent. Turbulent shear stresses as high as 3500 $dynes/cm^2$ have been estimated in the region between the vessels walls and the ball occlusion. Even with modern MHV designs, namely thinning disc and bileaflet valves, the shear layers that form at the edges of the leaflets or disc evolve into a region with turbulent flow characteristics. Turbulent shear stresses of 1500 $dynes/cm^2$ are common in these two designs.

In the case of atherosclerosis, which typically takes a few decades to develop, formed elements of blood, particularly monocytes and lipids, are recruited to the arterial walls where a cascade of biological responses results in the formation of fatty streaks called plaque (see 1.1). The deposition of plaque on the endothelium reduces the vessel diameter and during advanced stages of the disease the blood vessels become considerably narrower, creating a constriction (or stenosis) that significantly alters the local blood flow dynamics. Early work on analyzing the flow disorder in pulsatile stenotic flows came from *in vivo* measurements of blood velocity. Khalifa et Giddens [24], for example, studied the velocity signal in the descending thoracic aorta of dogs with surgically induced stenosis. They considered Reynolds numbers in the range of $1000 < Re_m < 1200$ (Re_m is based on the average bulk velocity during the pulsatile cycle and the un-occluded diameter upstream of the

stenosis), and varied the degree of stenosis, defined as the percent reduction of the un-occluded cross sectional area, up to a maximum of 88%. They observed that even mild occlusions yielded flow disorder immediately downstream of the stenosis. The instabilities commenced around the peak systolic velocity, and as the degree of occlusion increased, so did the duration of flow disorder. Energy frequency spectra were calculated for four short intervals during the cycle. It was found that as the degree of stenosis increased, the spectra during the deceleration phase exhibited a higher and broader energy content. Another example of *in vivo* measurements of intravascular pressure fluctuations and blood flow velocity in a surgically induced stenosis at the pulmonary artery of calves has been reported by [29]. Their work was motivated by the fact that the turbulence in the post-stenotic region generates acoustic sounds and murmurs, with a postulate that proper interpretation of these murmurs can prove a diagnostic tool of cardiovascular diseases. They also divided the pulsatile cycle into four time intervals and computed pressure and velocity spectra for each interval. They found that the energy spectra exhibited a $-5/3$ slope during early through late systole up to approximately 100 Hz and then broke into a $-10/3$ slope. They attributed this change of slope (or break) to transfer of turbulent kinetic energy into acoustic fluctuations. Support for this conjecture was drawn from the fact that the sound (or pressure) spectra exhibited a rise in intensity at a frequency immediately following the break in frequency of the energy spectra. In addition, the break frequency in the pressure spectra was not dependent upon the percent of stenosis or the jet peak velocity.

1.2 Relevance of Hemodynamics to Atherosclerosis

From the above examples it is evident that the presence of stenosis has a significant impact of the local blood flow patterns and the mass and momentum transport near the vascular boundary. Some interesting question one can ask are: What is its role of hemodynamics in this particular disease process? How does turbulent or disturbed flow affect the function of the endothelial cells, red cells, platelets and other cells which participate in the disease process? Do the cells even differentiate between laminar and turbulent flow?

The fact that atherosclerosis is focal in nature suggests that local hemodynamics might play a role in this particular disease process. Atherosclerosis is mainly found in medium and large size arteries near bifurcations and branching of arteries, regions of arterial narrowing and regions with curvature. [33, 50, 16, 14, 3]. These sites are characterized by unique flow patterns such as flow separation, recirculation and reattachment. As a result the endothelium in these regions is exposed to highly complex spatio/temporal normal and shearing forces [18]. Endothelial cells which line the innermost layer of the vessels (intima) are directly subjected to these complex hemodynamic stress environment and are believed to be one of the key factors of mechanotransduction (mechanisms by which cells convert mechanical stimulus into chemical activity). This is the reason that the biological response of endothelial cells to shearing stresses has been the focus of extensive studies.

Davies *et al.* [1] demonstrated that vascular endothelial cells respond distinctly to turbulent and laminar flow shear stresses. In their studies, bovine aortic

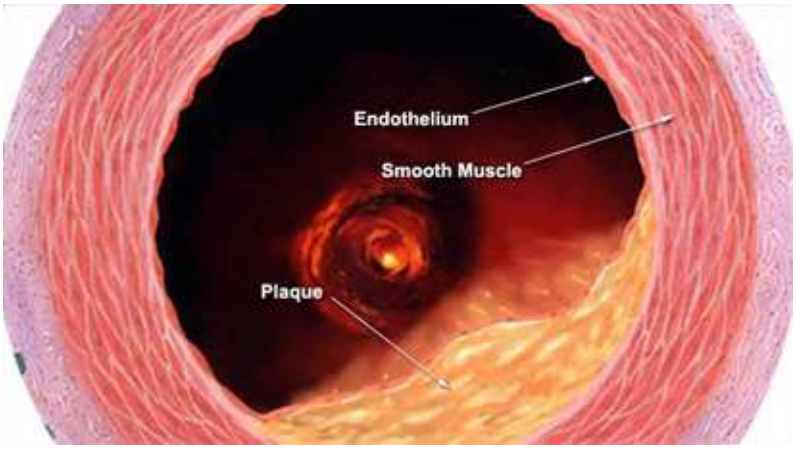

Figure 1.1: Schematic showing a large artery with atherosclerosis. Lipids and monocytes transported by the blood in the lumen are recruited in the endothelium leading to the formation of fatty streaks and lesions. Migration and proliferation of smooth muscles cells are responsible for intimal thickening, a key characteristic of lesion-prone regions.

endothelial cells were subjected for various periods of time to laminar and turbulent flow conditions generated by a cone-plate apparatus. Laminar flow was generated by using a cone angle of $1/2^{\circ}$ and mean shear stress values of 8 $dynes/cm^2$ were obtained. Turbulent flow was generated by using a cone angle of 5° and mean shear stresses as low as 1.5 and as high as 14 $dynes/cm^2$ were obtained. The root-mean-square amplitude of the shear stress fluctuations did not exceed 25% of the mean value. The results showed that endothelial cells subjected to laminar flow for 24 hours became ellipsoidal in shape and aligned with the direction of the flow. In contrast endothelial cells subjected to turbulent shear stress were more rounded and randomly aligned. In addition, endothelial cell turnover (rate at which cells are lost and regenerated through cell division) was substantially increased in turbulent flow. This biological response is of interest in this type of studies because lession-prone

regions during the early stages of atherogenesis exhibit increased cell turnover. This work suggested that the small-scale, high frequency fluctuations, and the rapidly changing turbulent shear stresses may better correlate to biological responses linked to atherosclerosis than the mean shear stress. A possible reason for this behavior is the fact that in turbulent flow the scales of the smallest eddies approach the size of the endothelial cells and significant shear stress gradients exist over distances comparable to cellular dimensions.

Subsequent work has focused on the effects of shear stress gradients on the biological response of endothelial cells [18, 11, 27]. The most commonly employed in vitro models expose the cells to flow downstream of backward facing step. The flow patterns in this configuration, namely a recirculation zone, stagnation point and reattachment region, match the flow patterns encountered in lesion-prone regions such as arterial bifurcation and branches. In general endothelial cells below the recirculation zone and after reattachment appear to be less round than those near the reattachment point. Liu *et al.* [29] showed that these morphological changes were also accompanied by changes in cytoskeleton of the cells. The F-actin filaments in cells exposed to high shear were aligned in the direction of the flow, whereas near the stagnation point the actin filaments tended to localize in the periphery of the cells. In addition, cell turnover was enhanced enhanced near the reattachment point. Haidekker *et al.* [18] looked at the effects of the temporal shear stress gradients by varying the time duration of the onset of the flow in a backward-step flow chamber. In the experiments the flow onset was either sudden ($200ms$) or slowly ramped ($15s$) but the endothelial cells remain exposed to the steady flow

patterns for 4 hours after the onset. They estimated that in the sudden onset the temporal shear stress gradients were about 300 times larger than those in the ramped onset. The proliferation rate of endothelial cells was much higher in the case of sudden onset and matched the spatial distribution of exposure to temporal shear stress gradients. In light of the fact that the duration of the exposure to temporal gradients of shear stress was very short in comparison to the total duration of flow exposure, their results demonstrated that endothelial cells are sensitive to very short transient stimulation events.

The blood flow dynamics of atherosclerotic sites, in particular during advanced stages of the disease, may also play a major role in the hemolysis of red blood cells. Hemolysis is associated with the failure of the red blood cell membrane and the release of hemoglobin in the blood stream. In the case of severe stenosis the increased levels of shearing stresses in the constriction and the elevated turbulent stresses in the shear layers downstream, can cause hemolysis of the red blood cells. Sallam *et al.* [49] investigated the effects of turbulent shear stresses on the damage of red blood cells downstream of an annular jet of PBS solution. A laser Doppler anemometer system was used to carefully survey the flow field characteristics before the introduction of red blood cells. A specially designed aspirator was used to sample red blood cells from any location in the flow field. Incipient hemolysis was detected at a level of Reynolds shear stress of approximately $400 N/m^2$, below which a sublethal level of zero hemolysis took place. A clear trend of increase in red blood cell hemolysis with increased levels of turbulent shear stresses was evident.

From the above examples it is evident that the complex flow patterns asso-

ciated with highly disturbed flow at atherosclerotic cites, can trigger some unique biological responses. Therefore in-depth understanding of the origin and dynamics of turbulence in these cites is imperative illuminating several aspects on the initiation, progression and treatment of the disease.

1.3 Flow in Stenotic Vessels: State of the Art

Although *in vivo* studies have highlighted the turbulent characteristics of the post-stenotic region, they failed to elucidate the detailed mechanisms that caused the flow to transition. This was due to limited measurement capabilities and inherent difficulties in conducting animal experiments under closely controlled conditions. Significant progress, however, in understanding the fluid dynamics of post-stenotic flows has been made utilizing idealized *in vitro* studies. A variety of experiments by Giddens and co-workers [7, 25, 2, 28], [37], and [54] among others, have been reported over the past decades. In most cases, the experimental conditions were not representative of a specific segment of the human anatomy, but rather designed to isolate the main phenomena that dominate the dynamics of the flow. In particular, the arteries were assumed to be rigid, straight pipes with sharp or contoured constrictions, and various degrees of stenosis. The flow conditions were selected to be within the same range as in previous *in vivo* studies mentioned above, and in most cases the flow upstream of the constriction was laminar throughout the pulsatile cycle. In the post-stenotic region, however, a highly complex, multi-step process of transition to turbulence was observed. Initial disturbances appear during

the higher velocity portion of the pulse, preceded by a large, low-frequency fluctuation. Based on flow visualizations and velocity measurements, Giddens *et al.* [7] [2] speculated that the latter was caused by a 'start-up' vortex forming downstream of the constriction, and swirling into the region near the wall. Following this structure, a quasi-periodic array of vortices is generated, probably as a result of a Kelvin-Helmholtz type instability in the shear layer. [28] found that the amplitude and shedding frequency of the vortices can change by a factor of two during the pulsatile cycle. The breakdown of these structures and their interaction with the wall, primarily during the deceleration phase leads to very high turbulent intensities in the region just after the mean reattachment point.

While such experiments have successfully demonstrated the existence of a shear layer instability and vortex shedding, they did not provide adequate resolution to quantify the spatio-temporal evolution of the turbulent structures. Thus, in recent years numerical tools have also been utilized to analyze the post-stenotic flow field. A significant amount of computational work has concentrated on solving the Reynolds-Averaged Navier-Stokes (RANS) equations coupled with a turbulence model to predict the phase-averaged flow field ([59], [23], [56]). Although such simulations have a relatively low-computational cost and allow for long integration times due to the relaxed spatial and temporal resolution, they suffer from inherent difficulties associated with turbulence modeling. One difficulty comes from the fact that most of these models were developed for equilibrium turbulent wall bounded flows, and as such, they are not well suited for flows with separation and reattachment zones or transitional flow patterns such as the ones shown in the experiments. [51]

tested various turbulence models for the unsteady RANS equations using a Direct Numerical Simulation (DNS) database of turbulent pulsatile channel flow. Their results showed that the Reynolds stresses, turbulent kinetic energy, and dissipation were significantly overestimated. The development of suitable closure models, if advisable at all, would be contingent on first having a detailed knowledge on how turbulent kinetic energy is produced, dissipated and transported in the post-stenotic region.

In order to circumvent the uncertainties posed by such modeling strategies, one can approach the problem through the use of increased resolution (and expense) by performing DNS and/or Large-Eddy Simulations (LES) of the flow. Recently, [32] reported DNS and LES of pulsatile flow in a planar model of an asymmetric stenosis with 50% occlusion and a mean Reynolds numbers in the range of $375 < Re_m < 1000$. The imposed asymmetry forced the shear layer that separates at the lip of the stenosis to tilt towards the opposite side of the channel. For all cases with $Re_m > 500$ the separated shear layer rolled up into a series of vortices reminiscent of a Kelvin-Helmholtz type instability. The effect of these transitional patterns on the wall region after the reattachment point were assessed by spectral analysis. The frequency spectra of the streamwise velocity in that region exhibited a break from $-5/3$ to a -7 slope at roughly the frequency corresponding to the frequency of vortex shedding. This suggested the existence of possible turbulent-like flow with a well-defined inertial subrange. More recently, [53] performed a numerical study of both steady and pulsatile axisymmetric stenotic flows with a smooth 75% constriction at mean Reynolds numbers in the range of $250 < Re_m < 550$. Floquet

stability analysis revealed that all the leading unstable modes arise through a period-doubling bifurcation whose main characteristic was to alternately tilt the vortex rings forward and backwards. Subsequent flow visualizations from DNS confirmed the existence of such a mode and showed that the breakdown of the vortex rings leads to the formation of streamwise oriented vortical structures. In addition to these phenomena, a shear layer oscillation was observed only when high-frequency and low-amplitude perturbations where added at the inflow.

From the brief literature survey above, it is evident that significant progress has been made in understanding the basic mechanisms that lead to transitional flow patterns in stenotic pulsatile flows. Central in this process appears to be the formation of large vortical structures that undergo complex three-dimensional instabilities transforming primarily spanwise into streamwise vorticity. There are, however, several outstanding questions:

- How do these vortices interact with the wall and breakdown, and what is the effect of the breakdown process on the reattached layer?
- Are the structures that emerge in the reattached layer similar to the ones observed in turbulent wall bounded flows?
- How is turbulent kinetic energy produced, transported and dissipated in the post-stenotic region?

To clarify these issues, we have performed a series of DNS in both planar and axisymmetric geometries. An outline of the thesis is given below.

1.4 Outline

The outline of this dissertation is as follows:

In chapter 2 the numerical code used to perform the simulations is described in detail. The code, which is a Navier-Stokes finite difference solver, is discretize on a Cartesian or cylindrical coordinate grid. The stenosis which is not aligned with the grid is thus accounted for using an embedded boundary formulation. The details of the scheme used to interpolate the velocity near the stenosis such that on the surface of the stenosis the velocity satisfies the non-slip condition is explained. Finally, the parallelization of the code is also discussed. The key features in fine-tuning the code and optimizing the parallel communication calls are explained. Performance results for simulation with grids up to 1.1 billions points and 500 processors are shown.

In chapter 3 we establish the accuracy of the code by directly comparing results from the simulations with those from an experiment carried out by Prof. Kiger and Mr. Parvinian at the university of Maryland. It is explained how we coordinated the simulations with the experiment so as to more closely reproduce the disturbance environment upstream of the stenosis. The effect of the noise environment at the inlet on the downstream post-stenotic flow is also assessed. Besides comparison with the experiment, a grid independency study is performed to ensure that velocity and turbulence statistics do not change with grid resolution or domain size.

In chapter 4 a series of simulations in an idealized planar geometry covering a parametric range representative of physiological conditions are presented first. The spatial and temporal evolution of the structures responsible for the generation of

turbulence and their effect on the phase averaged statistics and turbulent kinetic energy budgets is discussed. The instantaneous flow dynamics in a tube with an axisymmetric stenosis is also presented. The mechanisms by which these vortical structures originating in the shear layer transform into turbulent-like structures in the reattached wall region are identified. The effect of Reynolds number and reduced velocity on the transition process is discussed.

Chapter 5 the rheology of blood and the phenomena responsible for its shear thinning behavior are first explained. Various viscosity models that are commonly used to account for the non-Newtonian nature of blood are presented. A simulation for a laminar flow inside a tube with a stenosis is presented first to validate the implementation of a bi-viscosity model. Then results for simulation at a Reynolds number of 600 inside a tube with a sharp stenosis are discussed. This study was motivated by an *in vitro* experiment by Stein *et al.* [55] that showed a dramatic increase of turbulent intensities downstream of a sharp constriction when blood with various levels of hematocrit was used compared to plasma. The effect of the shear thinning behavior of a bi-viscosity model on the turbulence characteristics downstream of a sharp constriction is assessed.

Finally in chapter 6 conclusions are given.

Chapter 2

Methodologies

2.1 Mathematical model

In the majority of the numerical simulations presented in this body of work we treat blood as a Newtonian incompressible fluid and the vascular walls as rigid tubes. Therefore the problem can be described by the Navier-Stokes equations:

$$\frac{\partial u_i}{\partial t} = -\frac{\partial (u_i u_j)}{\partial x_j} - \frac{\partial p}{\partial x_i} + \frac{1}{Re}\frac{\partial^2 u_i}{\partial x_j \partial x_j} \tag{2.1}$$

$$\frac{\partial u_i}{\partial x_i} = 0 \tag{2.2}$$

where x_i and x_j (i,j = 1,2,3) are the Cartesian coordinates, and u_i and u_j are the velocity components in the corresponding directions. The equations are written in dimensionless form. The velocity components and distances have been scaled by a reference velocity U and a reference length L respectively. The pressure is normalized by ρU^2, with ρ being the density of the fluid, and Re is the Reynolds number defined as $Re = \rho UL/\mu$.

2.2 Numerical Methods

To perform a direct numerical simulation the above equations are discretized on a staggered Cartesian or cylindrical coordinate grid. In the staggered configuration each velocity component is located at the center of each face as shown in

figure 2.1, while the pressure and viscosity are located in the center of the cell. The equations have been integrated directly in time without introducing any model. In particular, a standard second-order central-difference scheme is used to approximate spatial derivatives while the fractional step method is used to integrate the governing equations in time. The time integration scheme for the Cartesian coordinates is explicit and either a second-order Adams-Bashforth (AB2) scheme or the low-storage third-order Runge-Kutta (RK3) scheme is used:

$$\frac{\hat{u}_i^k - u_i^{k-1}}{\Delta t} = \gamma_k A(u_i^{k-1}) + \rho_k A(u_i^{k-2}) - \alpha_k \frac{\partial p^{k-1}}{\partial x_i}, \tag{2.3}$$

$$\frac{\partial^2 \phi^k}{\partial x_i \partial x_i} = \frac{1}{\alpha_k \Delta t} \frac{\partial \hat{u}_i^k}{\partial x_i}, \tag{2.4}$$

$$u_i^k = \hat{u}_i^k - \alpha_k \Delta t \frac{\partial \phi^k}{\partial x_i}, \tag{2.5}$$

$$p^k = p^{k-1} + \phi^k \tag{2.6}$$

where k is the time subscript and ranges from 1 to 3 for the Runge-Kutta scheme and is 1 for the Adams-Bashforth scheme. The velocity $\hat{u}_i$ is the intermediate velocity which does not satisfy the continuity equation. Therefore the Poisson's equation for pressure 2.4 is solved directly and the scalar ϕ is used to project $\hat{u}_i$ into a divergence-free field. The spatial operator A contains the convective and viscous fluxes which are evaluated at the cell faces. The discretization of the above equations on a staggered grid in computational space is described in detail in [4, 61]. Δt is the time step and the coefficients for the RK3 scheme are:

$$\alpha_1 = 8/15, \gamma_1 = 8/15, \rho_1 = 0$$

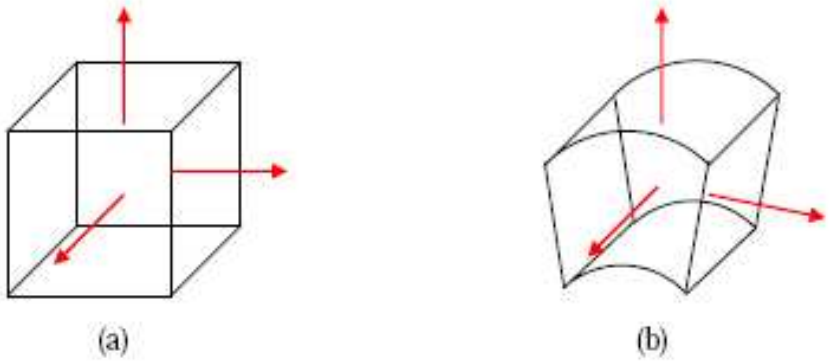

Figure 2.1: Collocation points of velocity in a) Cartesian grid cell; b) cylindrical grid cell

$$\alpha_2 = 2/15, \gamma_2 = 5/12, \rho_2 = -17/60$$

$$\alpha_3 = 1/3, \gamma_3 = 3/4, \rho_3 = -5/12$$

with

$$\sum_{k=1}^{3} \alpha_k = \sum_{k=1}^{3} (\gamma_k + \rho_k) \tag{2.7}$$

and the AB2 coefficients are:

$$\alpha_1 = 1, \gamma_1 = 3/2, \rho_1 = -1/2 \tag{2.8}$$

with

$$\alpha_1 = \gamma_1 + \rho_1. \tag{2.9}$$

The following stability criterion (or the generalized CFL number including the time step constraint from the viscous terms) is adopted [57]:

$$CFL = \Delta t \left[\frac{|u|}{\Delta x} + \frac{|v|}{\Delta y} + \frac{|w|}{\Delta z} + 2\nu \left(\frac{1}{\Delta x^2} + \frac{1}{\Delta y^2} + \frac{1}{\Delta z^2} \right) \right] \tag{2.10}$$

The CFL number used in the simulations for the RK3 scheme is 1.5 while for the AB2 a much lower number is used, e.g. CFL=0.6. In this study all simulations have been carried out using the RK3 scheme using a constant CFL.

2.3 Poisson Solver

The Poisson equation shown in vector form in eq. 2.4 can be expressed in discrete form in Cartesian coordinates as:

$$\left(\frac{\delta^2}{\delta^2 x} + \frac{\delta^2}{\delta^2 y} + \frac{\delta^2}{\delta^2 x} \right) \phi_{i,j,k} = f_{i,j,k} = \frac{1}{a_n \Delta t} \nabla \cdot \hat{u}_i^n \tag{2.11}$$

where $\phi = p^n - p^{n-1}$ and n is the substep index for RK3 or AB2 scheme. In cylindrical coordinates the equation becomes:

$$\left(\frac{1}{r} \frac{\delta}{\delta r} (r \frac{\delta}{\delta r}) + \frac{1}{r^2} \frac{\partial^2}{\partial^2 \theta} + \frac{\partial^2}{\partial^2 x} \right) \phi_{i,j,k} = f_{i,j,k} \tag{2.12}$$

With second order spatial derivatives the above equations would result in a hepta-diagonal matrix for the coefficients of ϕ which is impossible to solve directly. In order to employ a direct solver, first the FFT of eqns. 2.11 and 2.11 is taken in the y direction (spanwise direction in the case of Cartesian coordinates and azimuthal direction in the case of cylindrical coordinates). Thus the flow is assumed to be homogeneous and periodic in that direction and the grid must be uniform in y. In discrete space the fast Fourier transform method from FFTPACK [58] is used. This

renders eq. 2.11 in wave space as:

$$\left(\frac{\delta^2}{\delta^2 x} + k_l\prime + \frac{\delta^2}{\delta^2 x}\right)\hat{\phi}_{i,j,k} = \hat{f}_{i,j,k} \tag{2.13}$$

where k_l is the modified wave number expressed as:

$$k_l\prime = \frac{2}{\Delta y^2}\left[1 - cos(\frac{2\pi l}{N_y})\right] \tag{2.14}$$

and l is the wave number, N_y is the number of grid cells in the periodic direction (not including ghost cells) and Δ_y is the cell size in y. Since the above equations include only derivatives in x and z the resulting coefficient matrix is penta-diagonal. The set of N_y uncoupled equations in wave space are solved independently using the "BLKTRI" routine from the FISHPACK library, in which a generalized cyclic reduction algorithm is implemented [58]. The solution is then transformed back to real space by taking the fast inverse transform of $\hat{\phi}$.

2.4 Embedded Boundary Method

The stenosis, which is not aligned with the grid lines, is introduced using an embedded-boundary formulation. For a stationary object such as the stenosis the velocity near the wall is locally reconstructed in such a way that the no-slip conditions are satisfied. With this strategy, we can extend the range of applicability of highly efficient Cartesian solvers to complex configurations. The present approach is second-order accurate both in space and time, and maintains the optimal conservation properties of Cartesian solvers that are essential in performing DNS. We

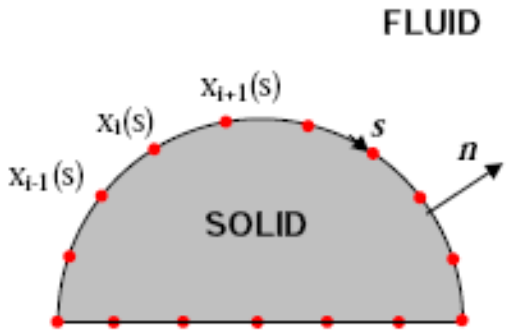

Figure 2.2: A set of equally spaced marker points are use to describe the interface of the immersed body. The fluid is always to the left of the solid as one moves in the direction of increasing parameter s

begin by describing how this local reconstruction technique is applied to immersed objects that are either two-dimensional in the case of the Cartesian coordinates or axi-symmetric in the case of the cylindrical coordinates.

An arbitrary object is represented by a evenly distributed set of marker particles as shown in figure 2.2. Their spacing is comparable to the local grid size. For each marker particle, the previous and next marker particles are used to define a second order polynomial as:

$$x(s) = a_x s^2 + b_x s + c_x, \qquad y(s) = a_y s^2 + b_y s + c_y$$

where s is the arc-lentgh coordinate. The fluid is always located on the left hand side as one moves along the interface toward increasing s. The unit normal vector at any location on the interface is defined as:

$$n_x = -\frac{y_s}{\sqrt{(x_s^2 + y_s^2}}, \qquad n_y = -\frac{x_s}{\sqrt{(x_s^2 + y_s^2}}$$

where x_s and y_s are the derivatives of the surface coordinates with respect to the arc length parameter s. These derivatives are analytically given by:

$$x_s(s) = 2a_x s + b_x, \qquad y_s(s) = 2a_y s + b_y$$

With the surface of the immersed object analytically defined, the classification of the eulerian grid points with respect to the body is performed. As a first step, the collocation points of the velocity components and the pressure are classified and tagged as points *outside* and *inside* the body. The tagging is performed as follows:

1. Determine a subdomain that encloses the immersed object. Any points that are outside this domain are flagged as *outside* or $fluid$ points.

2. Foreach Eulerian grid point inside the subdomain find the marker point s_b closest to it. Build a vector r from the marker point to the grid point and calculate the dot product between the two vectors.

3. If $\vec{r} \cdot \vec{b}$ is positive then the point is outside the body, else the point is inside the body and it is flagged as *body* point.

Next, we have to determine the points near the surface of the immersed object whose velocity is going to be reconstructed. To do this a loop is performed for all fluid points inside the bounding subdomain and those fluid points that have at least one neighbor as a *body* point are tagged $forcing$ points. A neighbor in this case is the next or previous adjacent point in the x or z direction.

The velocity at the *forcing* point is interpolated during the predictor step along the nornal to the body using two surrounding fluid points. Thus, the normal intersection of the *forcing* point with the body is calculated first. This normal passes through the forcing point (x_i, y_i) and intersects the body at (x_n, y_n) (given by s_n). Therefore the dot product of a vector tangent to the intersection with the vector defined by the forcing point and the interesction point should be zero.

$$(x_i - x_n)\frac{x_s}{\sqrt{(x_s^2 + y_s^2)}} + (y_i - y_n)\frac{y_s}{\sqrt{(x_s^2 + y_s^2)}} = 0$$
$$(x_i - x_n)x_s + (y_i - y_n)y_s = 0$$

Substituting the derivatives x_s and y_s from eq. 2.15 and also x_n and y_n from eq. 2.15 results in the following third order polynomial:

$$\begin{aligned}
&(2a_x^2 + 2a_y^2) && s_n^3 \\
&+(3a_x b_x + 3a_x b_x) && s_n^2 \\
&+(2a_x c_x + 2a_y c_y + b_x^2 + b_y^2 - 2a_x x_i - 2a_y y_j) && s_n \\
&+(b_x c_x + b_y c_y - b_x x_i - b_y y_j) && = 0
\end{aligned}$$

The above system is solved iteratively using the Newton-Rapshon method and initial guess the closing marker point. When s_n is known the interface- normal coordinates (x_n, y_n) and its unit normal vector are evaluated.

Using the normal vector we then build a compact interpolation stencil using two points in the fluid and the intersection. The two neighboring fluid points can

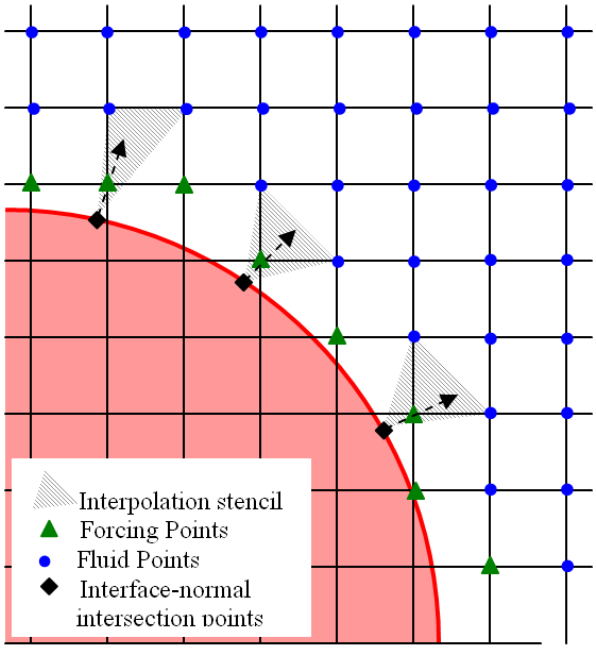

Figure 2.3: Generalized interpolation stencil

be either along the diagonal or the x or z gridlines of the cell containing the forcing point. This way the interpolation stencil remains compact which greatly facilitates the parallelization of the code. A schematic of the interpolation stencil is shown in figure 2.3.

The interpolation is then performed assuming that the velocity varies as follows:

$$\phi = b_1 + b_2 x + b_3 y \tag{2.15}$$

where x and y are with respect to the forcing point. To solve for the three coefficients b_1, b_2, and b_3 the following system of equations is solved:

$$\begin{bmatrix} b_1 \\ b_2 \\ b_3 \end{bmatrix} = A^{-1} \begin{bmatrix} \phi_1 \\ \phi_2 \\ \phi_3 \end{bmatrix} = \begin{bmatrix} 1 & x_1 & y_1 \\ 1 & x_2 & y_2 \\ 1 & x_3 & y_3 \end{bmatrix}^{-1} \begin{bmatrix} \phi_1 \\ \phi_2 \\ \phi_3 \end{bmatrix} \tag{2.16}$$

where x_1,y_1 are the coordinates of the interface-normal intersection and x_2,y_2 and x_3,y_3 are the coordinates of the fluid points near the body. The inverse of the matrix A is solved once during the beginning of the code and is stored in memory. The above interpolation scheme has been extended in 3D by addition of a term of the form, $b_4 z$, to the polynomial in eq. 2.15 but it has proven to be unstable in cylindrical coordinates where the grid aspect ratio of the cells is not unity. In particular the grid spacing in the azimuthal direction can become considerably larger than the grid spacing in the other two directions as one moves away from the centerline resulting in interpolation stencils that are ill conditioned or for which the forcing point does not lie inside the interpolation pyramid. For that reason we have implemented a different interpolation scheme for three-dimensional objects.

2.5 Parallelization of Code

The code is parallelized using a classical domain decomposition approach. The communication between processors is carried out using MPI library calls. To minimize the cost of communication the domain is evenly divided based on the number of points along the direction of the flow where the grid has the most points. The predictor and corrector step are solved independently on each processor. Each subdomain contains one layer of ghost cells to its left and right in order to evaluate

the second order spatial derivatives at the end of the subdomains. The values of the ghost cells in each processor are communicated from the first and last interior cells from the processors adjacent to it everytime during the predictor and corrector steps. However, the main communication cost arises from the solution of the Poisson solver. In order to solve the set of uncoupled equations 2.13 in parallel each processor must know the pressure in the entire $x-z$ planes. Since the domain is divided among the processors in the z direction a domain redistribution must me performed. A schematic representing this domain redesrtibution in cylindrical coordinates is shown in 2.4.

During the redistribution, the first N_{proc}/N_y $x-z$ slices of the domain of each processor have to be communicated to processor 1. Likewise the second N_{proc}/N_y $x-z$ slices of the domain of each processor have to be communicated to processor 2 until the entire domain had been redistributed as show in 2.4c. In total, the amount of data that is communicated is equal to the domain size ($N_x \times N_y \times N_z$) and it takes N_{proc}^2 communcations to do this. Of course, this domain redistribution has to been performed one more time in the reverse direction once the Poisson solver is solved. As the size of the grid becomes larger than 100million points and the number of processors increases, optimization of the MPI calls during this step is crucial. To reduce latency time each processor performs an MPI_SENDRECV call with the other $N_{proc}-1$ processors in order of processor with rank closest to it. In the schematic shown in 2.4 processor 1 would communicate first with processor 2, then 3, then 4. Likewise processor 2 would communicate first with processor 1, then 3, then 4, processor 3 would communicate first with processor 2, then 4, then

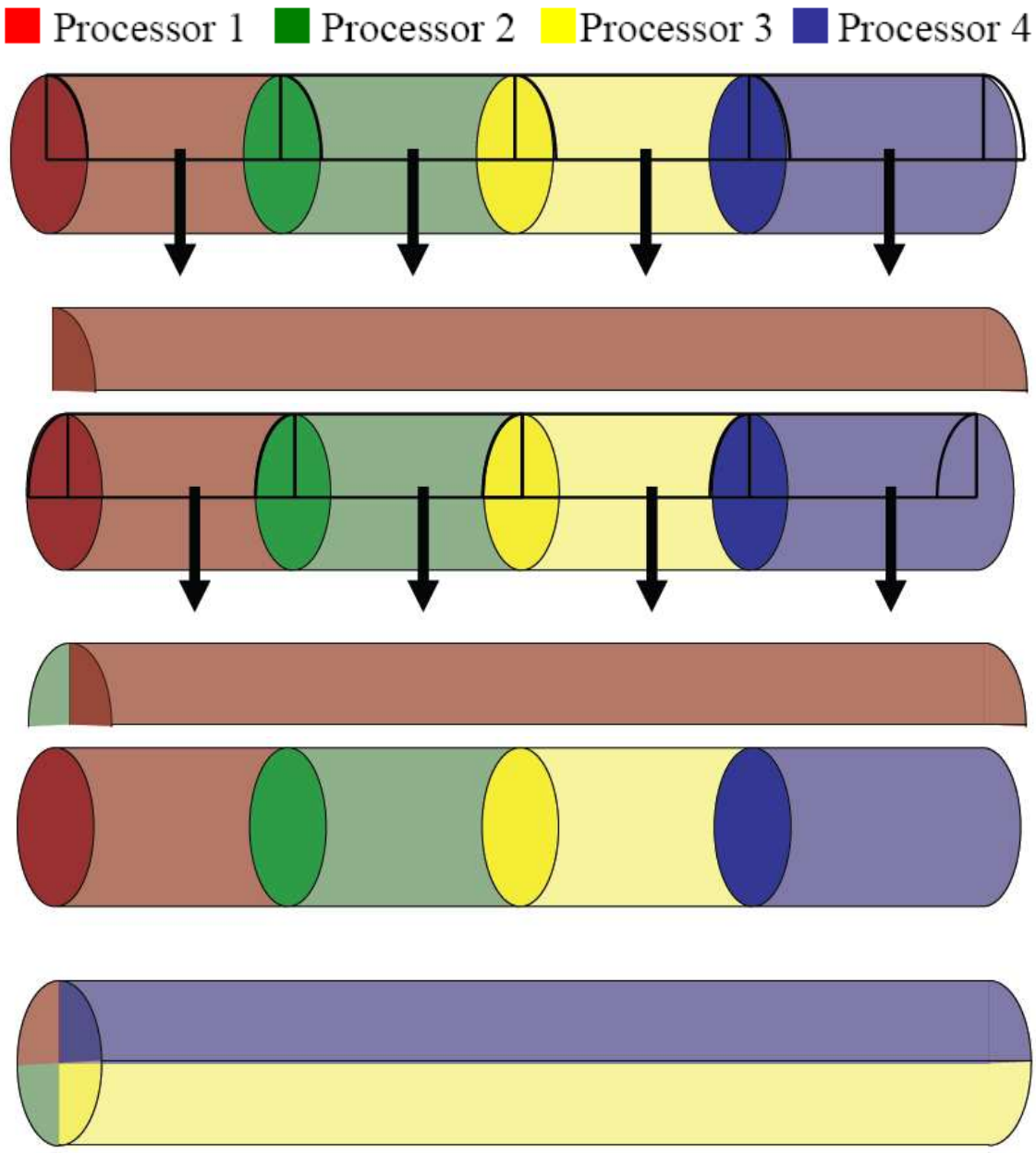

Figure 2.4: Schematic representation of domain redistribution in cylindrical coordinates.

1 and processor 4 would communicate first with processor 3, then 2, then 1. In this scenario, processor 1 would communicate to processor 4 after it has communicated with two 2 processors. But also processor 4 would communicate with processor 1 after it has communicate with two 2 processors. Besides the communication scheme another factor that affects the communication time is the speed at which information is exchanged. This parameter of course depends on the cluster specific hardware. For that reason a parallel speedup of the code for a simulation including the embedded boundary treatment had been performed on a high performance cluster employing an infiniband switch, which to date is the highest bandwidth switch. The results from these tests are listed in 2.1. The test cases presented here are not for a fixed size grid and the number of point per processor is shown versus the average time it took the slowest processor to perform one iteration. Difference between the slowest and fastest processors were not more than 5%. This is mostly due to the fact that load of the immersed boundary algorithm is not evenly distributed among processors. In some processors the subdomain does not contain any part of the immersed boundary, while others whose subdomain contains entirely part of the immersed boundary do more computational work. As shown in figure 2.5 the scaling of the code is linear for up to 500 processors and grids as large as 1.15 billions points. A typical example of breakdown of the time spent during on iteration in each major part of the code is summarized in 2.2. Approximately half of the time is spent in the Poisson solver and within the Poisson solver about 25% is spent in the set of MPI calls that redistribute the domain.

Grid Size	No. of Procs.	Grid/Proc	Refinement	Time/Iter.	Speedup
10 million	64	0.16	1	1.4	1
60 million	125	0.48	3.07	4.5	3.21
172 million	125	1.38	8.81	12.7	9.07
333 million	125	2.66	17.05	25.4	18.14
575 million	250	2.30	14.72	23.2	16.57
1.15 billion	500	2.30	15.72	22.5	16.0

Table 2.1: Cases used for assessing parallel scaling of the code for various grids

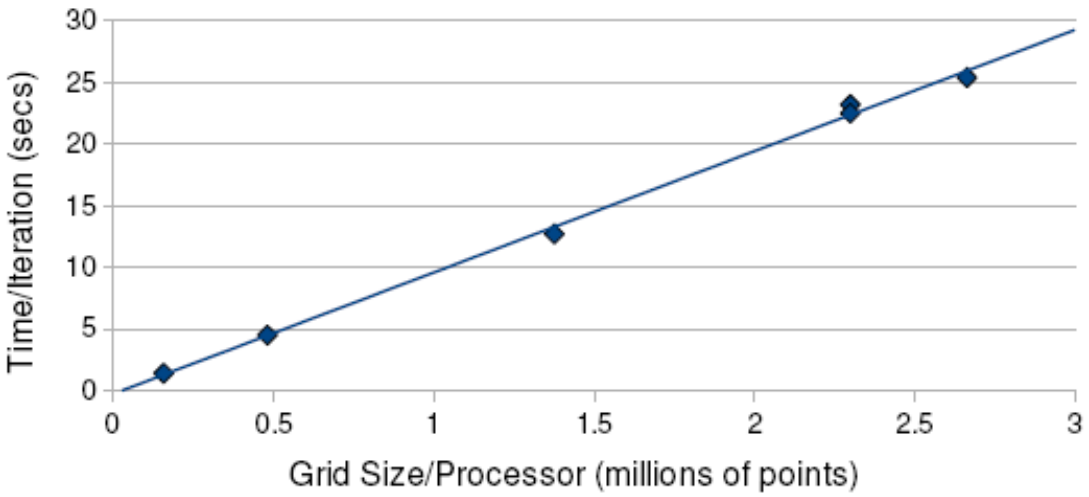

Figure 2.5: Parallel scaling of the code for various grids

Step	Time (secs)	Percentage
Right Hand Size	4.00	18.00%
Predictor	1.70	7.5%
Reconstruction	3.00	13.5%
Inversion (implicit)	2.00	9.00%
Divergence	0.50	2.20%
Poisson	11.90	53.00%
Corrector	1.17	5.20%
Pressure Update	0.71	3.18%
Input/Output	0.23	1.04%
Total	23.2	

Table 2.2: Breakdown of the time spent on each part of the code.

Chapter 3

Computational setup and validation

Pulsatile transitional flows are very sensitive to a variety of parameters, such as domain size, numerical resolution and boundary conditions especially at the inflow plane. In the present study, prior to conducting a detailed parametric study we will establish the sensitivity of the computations to the above parameters by performing a series of numerical experiments and by comparisons to laboratory experiments. The reference experiment was designed in collaboration with Prof. Kiger at the University of Maryland and was conducted by Prof. Kiger and Mr. Parvinian. In the next section the experiment will be discussed in detail. Then comparisons with the computations and some analysis on the sensitivity of the results to the disturbance environment, grid resolution and domain size will be given. The experiments were designed to simulate the flow dynamics in an ideal planar configuration to allow for faster convergence of statistics in the numerical simulations by sampling in the spanwise directions and thus eliminating uncertainties from time-averaging.

3.1 Experiment

The experiments were conducted by B. Parvinian and K. Kiger in a closed-loop pulsatile flow facility shown schematically in Fig. 3.1. The test section consists of a transparent acrylic, planar, channel with interior dimensions of $1830 \times 150 \times 12.5$

mm, in the streamwise, spanwise and wall-normal directions, respectively ($146H \times 12H \times 1H$, in terms of channel height, H). A symmetric stenosis was machined from brass in the shape of two cylindrical segments (radius of curvature of 12.5 mm and a height of 3.13 mm), giving a blockage ratio of 50%. The stenosis was placed $110H$ from the channel entrance to ensure fully developed flow upstream of the constriction, while still providing approximately $35H$ to observe the flow in the post-stenotic region. At the channel entrance, a contoured stagnation chamber with a series of open-cell foam filters and stainless steel screens was used to provide smooth, uniform flow. The flow through the channel was supplied by a constant head tank with an elevation of approximately 1 m above the exit tank free surface in order to isolate the system from the pump's impeller vibration. The oscillatory flow component was generated through the use of a custom built spool valve and stepper motor. The geometry of the spool valve orifice was designed to produce a linear variation of the flowrate with stroke position, allowing the use of a crank-arm and slider to obtain a nominally sinusoidal oscillation of the flow. In practice, however, the valve characteristics were slightly non-linear, and a small amount of play in the linkage contributed to a slight, but noticeable, dwell in the flowrate profiles as a function of time (see Fig. 3.3).

Detailed measurements of the flow characteristics were made using a single-component LDV. The measurement system consisted of a Dantec instrument (BSA P50 processor, FiberFlow 60X63 transceiver with beam expander) and computer controlled traverse system. The flow was seeded with a solution of hollow borosilicate glass spheres (Sphericel 110P8, by Potters Industries) nominally 10 μm in diameter

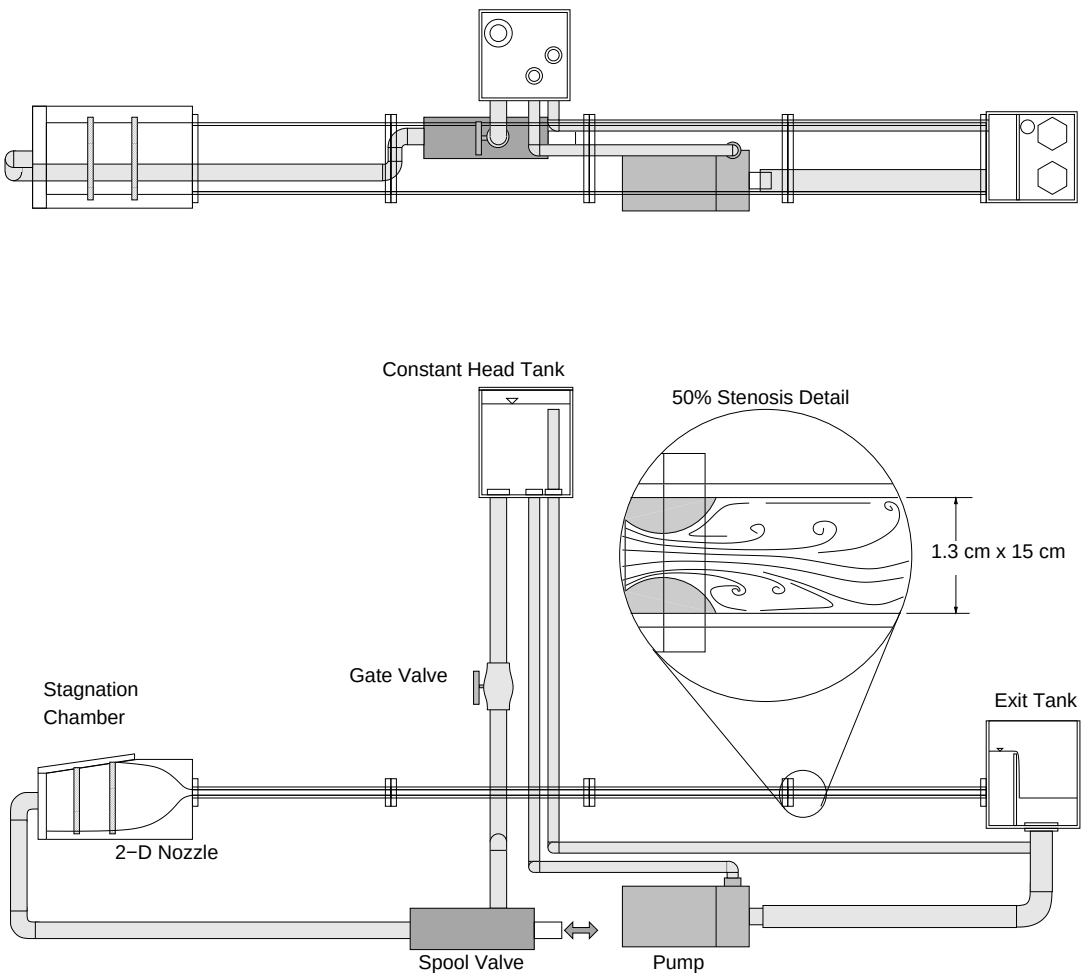

Figure 3.1: Schematic of the experimental setup.

with a specific gravity of 1.1. The particles were added in sufficient concentration of allow a mean sampling rate of 150 Hz. The mean bulk velocity was set to $\overline{U}_b = 0.082$ m/s, with an oscillatory amplitude of $\Delta\overline{U}_b$=0.06 m/s and a period of $T = 4$ sec. Water was used as the working fluid, and after several hours of warm-up operation, the temperature of the liquid stabilized to 25° C, giving a kinematic viscosity, $\nu = 9{\times}10^{-}7$ m^2/s. With the above dimensional values, the corresponding Reynolds and frequency parameter are $Re_m = \overline{U}_b H/2\nu = 570$ and $\alpha = H/2(2\pi/T\nu)^{0.5} = 8.25$, respectively. Profiles of the streamwise velocity were then recorded at 6 different streamwise stations (x/H = -10, +2, +4, +6, +10 and +20) with 0.5 mm intervals in the wall-normal direction (25 positions in each profile). Each position was sampled for a duration of 100 cycles. The arrival time of the samples was marked relative to the opening stroke of the spool valve, allowing the data to be ensemble averaged with respect to the phase of the bulk flow oscillation. In generating the phase-averaged data, each cycle was divided into 90 equally-sized bins. The number of samples in each position and phase varied depending on the velocity at that particular position in space and time, but the typical value was on the order of 600 samples per bin.

In both the experiments and simulations, two different types of averaging operators were utilized for the data reduction. A quantity, $f(x, y, z, t)$, can be averaged in time, and over lines in the homogeneous direction (y-lines) as follows:

$$\bar{f}(x, z) = \frac{1}{T_{tot} L_y} \int_0^{T_{tot}} \int_0^{L_y} f(x, y, z, t) dy dt \tag{3.1}$$

where $T_{tot} = NT$ is the total time of integration, and N is the number of periods, T, over which the equations were integrated. L_y is the spanwise length of the

computational box. Since the experiments were only conducted in the midplane of the channel, $L_y = 0$, reducing equation (1) to a simple time average. A phase-averaging operator was also constructed, which is very effective in extracting the response of the flow to the pulsatile frequency as follows:

$$\tilde{f}(x,z,t) = \frac{1}{N}\frac{1}{L_y}\sum_{n=1}^{N}\int_0^{Ly} f(x,y,z,t+nT)dy \tag{3.2}$$

The fluctuations with respect to the long-time and phase-averages will be denoted by prime and double prime respectively:

$$f'(\vec{x},t) = f(\vec{x},t) - \bar{f}(x,z) \quad f''(\vec{x},t) = f(\vec{x},t) - \tilde{f}(x,z,t) \tag{3.3}$$

In the experiments, both types of averages were conducted only in time over approximately 100 periods. In the DNS, the equations were initially integrated over 5 periods to gain independency from initial conditions. Statistics were then accumulated over 10 periods and in the spanwise direction.

Special attention was also given to calculating the frequency power spectra of the streamwise velocity signals in the experiments and computations. Due to the unsteady quasi-periodic nature of the flow and the fact that the discrete points on the signal are not equidistant, a direct Fourier-transform of the signal or its segments is not possible. To remove spectral information associated with the quasi-periodic temporal variation of the flow, we fit a second-order polynomial in a least squares sense to the segment of the velocity signal under consideration and subtract it from the signal. This operation results in applying a high-pass filter to the data in order to minimize the effect of periodic mean component of the signal. Polynomials up to fourth order were also tested and the peak in the frequency spectra did not

change considerably (variation less than 5%). We then use a 'slotting' technique, in which the autocorrelation function together with their discrete separation distances is calculated from the signal [details on the implementation of the 'slotting' technique, which is based on the formulation developed by [30], can be found in [42] and [43]]. The separation distances are then discretized into equally spaced bins or 'slots' and the power spectra are obtained either by FFT or an autoregressive method of the autocorrelation function. The later gives better resolution when the signal is short and was particularly useful in estimating the Strouhal number for the shedding frequency of the shear layer oscillations.

3.2 Computational setup

In order to establish the degree to which DNS can accurately reproduce the flow physics a carefully coordinated simulation was carried out first and results from that simulation were directly compared to those from the experiments. The stenosis shown in 3.2a was used in the simulation. It is represented by a semicircular arc and is mathematically given by

$$\left(\frac{z \pm z_0}{h}\right)^2 + \left(\frac{x}{h}\right)^2 = R, \tag{3.4}$$

where h denotes the half channel height, x and z are the streamwise and wall normal coordinates respectively, z_0 is the center offset of the cylindrical obstruction, and R is the radius of the cylinder. In all the cases investigated in the current work, values of $z_0/h = 1.5$ and $R/h = 1$ have been used. The occlusion based on the cross

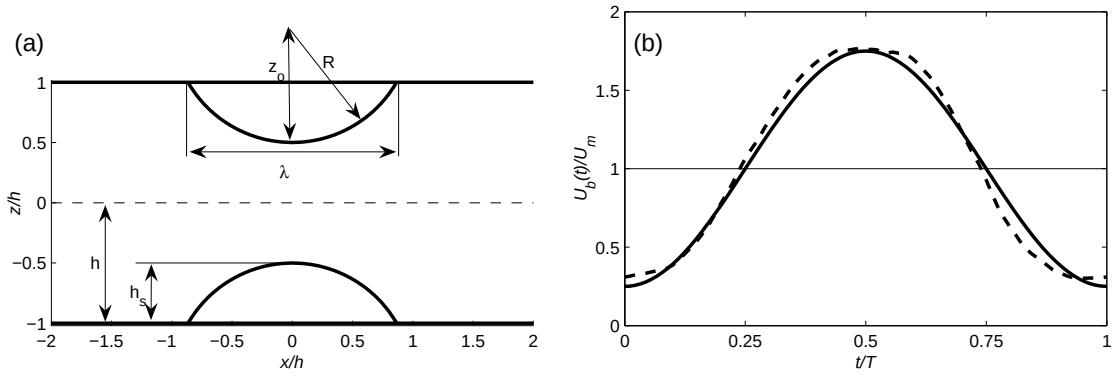

Figure 3.2: (a) Geometrical parameters that define the stenosis. (b) Waveform of $U_b(t)$: - - - cases 1 and 2; —— perfect sinusoid.

section area resulting from this stenosis is 50%. The stenosis has a length $\lambda = \sqrt{3}h$.

Table 3.1 summarizes the cases that were used for the purpose of comparison with the experiment. The mean Reynolds and Womersley numbers are 600 and 8.4 respectively. The flow rate was set to match that of the experiment, which deviates from a single-frequency sinusoid due to limitations in fine-tuning the spool valve in the experimental apparatus (see figure 3.2b). Case 1 differs from Case 2 in that synthetic noise was added to velocity profiles at the inlet. This difference in inflow conditions is meant to demonstrate the effect of the disturbance environment upstream of the stenosis on the flow characteristics downstream. The boundary conditions at the inflow plane will be discussed in detail in the next section. The grid has 598x64x106 points in the streamwise, spanwise and wall normal direction respectively and the domain extends $30h$ upstream and downstream of the stenosis and 2π in the spanwise direction. The distributions of grid points in the streamwise and wall-normal directions for cases 1 and 2 is shown in figure 3.3. In the streamwise direction the grid has its finest resolution of $dx/h = 0.03$ at $x/h = 0$ corresponding

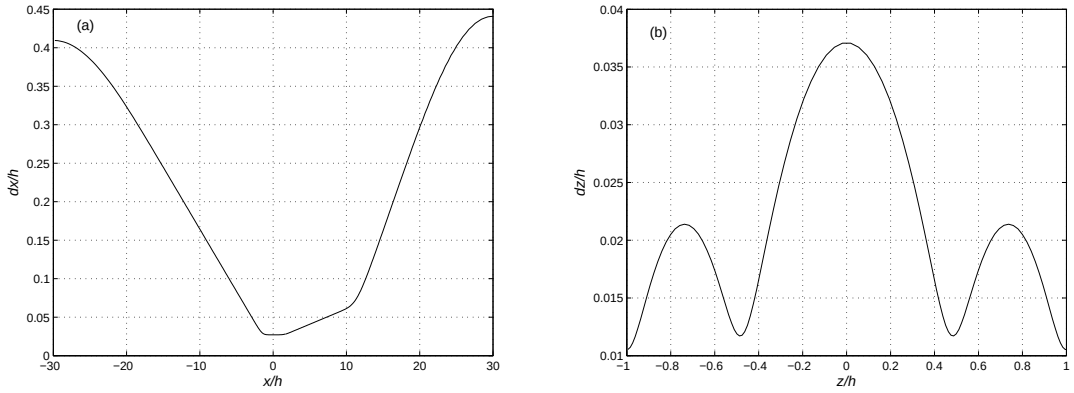

Figure 3.3: Grid spacing versus coordinate for (a) streamwise direction and (b) wall normal direction. The stenosis is located at $x/h = 0$.

to the location of the stenosis. From $x/h = 1$ to $x/h = 10$ corresponding to the region of the shear layers the grid spacing starts to increase although there is sufficient resolution to capture the shear layer instabilities and vortex shedding. After the mean reattachment ($x/h = 10$) the grid is made coarser, but it is always kept fine enough to resolve the quasi-streamwise vortices present in this area of the computational box. Finally the region between $x/h = 20$ and $x/h = 30$ serves as a buffer region for flow structures to leave the domain so no flow analysis was performed there. In the wall-normal direction the grid is stretched near the walls in order to capture the sharp velocity gradients expected in the reattached wall-region and also at the location of the shear layers. Non-slip conditions are enforced on all solid boundaries. A convective boundary condition that allows disturbances to propagate out of the domain without influencing the rest of the computational box is used at the outflow plane [38].

Case	Re	α	Domain Size	Grid Resolution	Inflow boundary condition
1	600	8.4	$60h \times 2\pi \times 2h$	$598 \times 64 \times 106$	$\widetilde{\vec{u}}_{exp} + \vec{u}''_{synthetic}$
2	600	8.4	$60h \times 2\pi \times 2h$	$598 \times 64 \times 106$	$\widetilde{\vec{u}}_{exp}$

Table 3.1: Set-up of simulations for purpose of comparing with experiment

3.3 Coordination between experiments and simulations

Central in matching experiments and simulations is the specification of the inflow boundary conditions in the simulations. For this reason, experimental data taken ten channel heights upstream of the stenosis ($x/H = -10$) were used to coordinate the setup of the numerical simulations. As for all other measuring stations in the experiment, the streamwise velocity statistics were measured at 25 equally spaced points in a profile normal to the wall with a temporal resolution of 90 intervals for each pulsatile cycle. Fig. 3.3a shows the variation of the measured unsteady Reynolds number, $\widetilde{Re}_b = \widetilde{U}_b H/2\nu$, (where $\widetilde{U}_b$ is the phase-averaged bulk velocity in the channel) during one pulsatile cycle. The corresponding value of $\widetilde{Re}_b$ based on the analytical solution produced from a perfectly sinusoidal pressure gradient is also shown. Although we tried to have a perfectly sinusoidal flow rate in order be able to compare with similar experiments in pipes and channels in the literature, limitations in fine-tuning the spool valve resulted in small deviations from the sinusoidal behavior, as can be seen in the figure.

Fig. 3.3b shows profiles of the phase-averaged streamwise velocity at the upstream measuring station, at four different instants in the cycle. The shape for all of

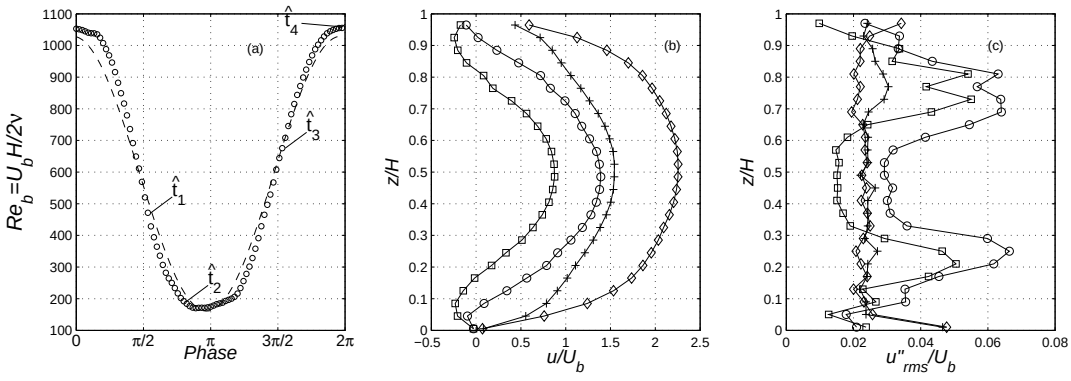

Figure 3.4: Present experimental results. (a) Reynolds number variation during the pulsatile cycle: ∘ experiment; **- - -** theoretical prediction based on a purely sinusoidal pressure gradient. (b) Profiles of the axial velocity, $\tilde{u}$, at $x/H = -10$. (c) Profiles of u''_{rms} at $x/H = -10$. ∘ , $\hat{t}_1 = 2\pi$; ▫ $\hat{t}_2 = 0.86\pi$; × , $\hat{t}_3 = 1.52\pi$; ⋄ , $\hat{t}_4 = 2\pi$.

the profiles is similar to that predicted by theory for a sinusoidal pressure gradient with reversed flow near the wall around the minimum flowrate (maximum deviation within 5%). To characterize the disturbance environment upstream of the stenosis, careful measurements of the streamwise velocity fluctuations were also conducted at the same upstream station. The corresponding phase-averaged fluctuations are shown in Fig. 3.3c. During the acceleration phase ($\pi < \hat{t} = 2\pi t/T < 2\pi$), the u''_{rms} levels are approximately uniform across the channel with a magnitude which is below 2% of the bulk velocity. This is what one would expect as typical background noise in such experiments, and is largely the result of a slight and gradual drift of the mean velocity combined with the resolution capabilities of the instrument. However, late in the deceleration phase close to the point of minimum flow rate, u''_{rms} increases in magnitude and gains a distinct shape with two peaks closer to the

wall. This suggests that the disturbances in the channel upstream of the stenosis during this part of the cycle are not strictly due to background noise, but rather are the result of an instability that never grows into a turbulent state.

Some support for this conjecture can be found in a study on transition in oscillatory pipe flows by Hino *et al.* [22]. They distinguish four different flow regimes in the Re_δ-α space (The Reynolds number, Re_δ, is based on the Stokes layer thickness $\delta = (2\nu/\omega)^{1/2}$ and amplitude of the bulk velocity): (I) laminar flow, (II) disturbed laminar flow, (III) intermittently turbulent flow and (IV) fully turbulent flow. Disturbed laminar flow was observed at a relatively low Reynolds number Re_δ of 128 for $\alpha = 3.9$ while intermittent or conditional turbulence occurred when $Re_\delta > 550$ and $\alpha > 2.3$. In the disturbed laminar flow regime, small-amplitude perturbations appear and are superimposed on the mean velocity during part of the cycle. These perturbations, however, are so small that they create an almost negligible deviation in the mean velocity profile, which still yields a good agreement with laminar theory. This behavior is very similar to the one we observed in the present experiments. Quantitative comparisons with the above study are not possible, however, because in our case the flow is in a planar channel with a much lower Stokes layer Reynolds number, $Re_\delta = 75$, and a driving frequency which is not purely sinusoidal. In a related study, Das and Arakeri [13] studied the transition of unsteady velocity profiles with reversed flow in both pipes and channels, and found that in the disturbed laminar flow regime a linear instability appears as a result of the inflection points in the velocity profiles. If the Reynolds number is above a critical value and there is sufficient time for the instability to grow, then the disturbance manifests itself as

a periodic array of vortices with a 180^o phase difference between the bottom and top walls of the channel. Similar vortices have also been observed by Merkli and Thomman [31] in oscillating pipe flow as long as the flow was not turbulent.

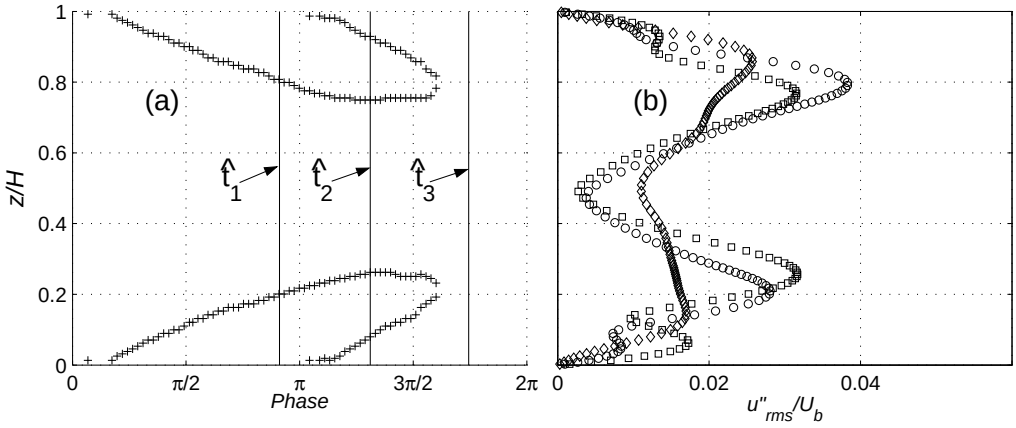

Figure 3.5: (a) z-locations of the inflection points of the streamwise velocity profiles at the inflow plane as a function of the phase angle; (b) profiles of u''_{rms} at $x/H = -13$ for instances in the cycle noted by the vertical lines in (a). $\circ$, $\hat{t}_1 = 0.9\pi$; $\square$, $\hat{t}_2 = 1.3\pi$; $\diamond$, $\hat{t}_3 = 1.75\pi$

In the present simulations, the accurate reproduction of the disturbed-laminar-flow upstream of the constriction is a challenging task, since it cannot be reproduced directly from the measured velocity statistics. This is a common problem in DNS of turbulent and disturbed flows, where at the inflow plane one needs to specify velocity fluctuations with prescribed moments and the correct phase information. To overcome this difficulty, we have located the inflow plane within the fully developed part of the channel at $x/H = -15$, and introduced synthetic noise to naturally trigger disturbances through the above mentioned inviscid instability mechanism. As

the disturbances are convected downstream, they will evolve and resemble the ones in the experiments. In particular, at the inflow plane the specified velocity vector consists of the sum of two parts: 1) a laminar component, which is obtained from the experimental results and is interpolated in space and time (using spline interpolation), and 2) a random component that is introduced to trigger instabilities when inflection points are present in the laminar profiles. To prevent the noise from decaying a few grid cells downstream from the inflow plane, fluctuations with prescribed moments and spectra were introduced. In particular, we used synthetic isotropic turbulence based on the formulation developed by Rogallo [44]. This procedure produces fluctuations that are isotropic, satisfy the continuity equation and have the von Karman energy spectrum. The fluctuations were scaled to have the magnitude of the background noise in the experiments, and were smoothly reduced to zero near the walls using a hyperbolic tangent function. Details on the implementation of this algorithm can be found in [39].

The advantage of this algorithm is that the input noise requires minimal adjustment length before realistic disturbances are realized. As it will be shown in the next section, the comparison of the disturbances at the experimental station upstream of the stenosis (at $x/H = -10$), with the ones from the above procedure is very satisfactory. In Fig. 3.5, the initial stage of the formation of these disturbances is demonstrated. Part (a) of the figure shows the temporal evolution of the mean velocity profile inflection points at the inflow plane. It can be seen that inflection points exist shortly after the maximum flow rate and for most of the acceleration phase. In Fig. 3.5b, profiles of the phase-averaged, root-mean-square streamwise

velocity fluctuations, u''_{rms}, are shown just downstream of the inflow plane for three different instances in the pulsatile cycle. It is evident that the locations of the peaks in these profiles at $\hat{t} \sim 0.9\pi$ and $\hat{t} \sim 1.3\pi$ correspond to the locations of the inflection points, while later in the cycle when the inflection point is absent, there is no such trend. Instantaneous flow visualizations reveal the appearance of pairs of staggered vortices at approximately $0.25H$ away from the walls. As the vortices propagate through the channel they perturb the flow, resulting in the distinct shape of the rms fluctuations.

3.4 Comparison and grid resolution

In this section, the effect of the disturbance environment upstream of the stenosis, the effect of grid resolution, and the effect of the domain size in the spanwise direction will be examined by detailed comparisons to the experimental results. To address the first issue we will compare results from Cases 1 and 2 in Table 3.1. In both cases, the grid resolution is the same (as we will demonstrate at the end of this section it is also sufficient to capture the dynamics of the flow), and they only differ on the specification of inflow boundary conditions. In Case 1 the procedure described in Section 3.3 is used, where synthetic turbulence is superimposed on the mean velocity profile. In Case 2, no disturbances are added, and as a result the flow upstream of the stenosis remains in an undisturbed laminar state throughout the cycle. Figs. 3.6-3.8 show comparisons of the phase-averaged statistics of the streamwise velocity component ($\tilde{u}$ and u''_{rms}) between Cases 1, 2 and the experiment.

In each figure, profiles at four streamwise locations are shown: $x/H = -10$, $x/H = 2$, $x/H = 4$, and $x/H = 6$. The first station is upstream of the stenosis and will be used to assess the quality of the inflow data, while all other stations are downstream of the stenosis. Each figure refers to one characteristic instance in the pulsatile cycle: midway through the acceleration ($\hat{t} \sim 3/2\pi$) in Fig. 3.6, near the maximum flow rate ($\hat{t} \sim 2\pi$) in Fig 3.7, and at the minimum flow rate ($\hat{t} \sim \pi$) in Fig. 3.8.

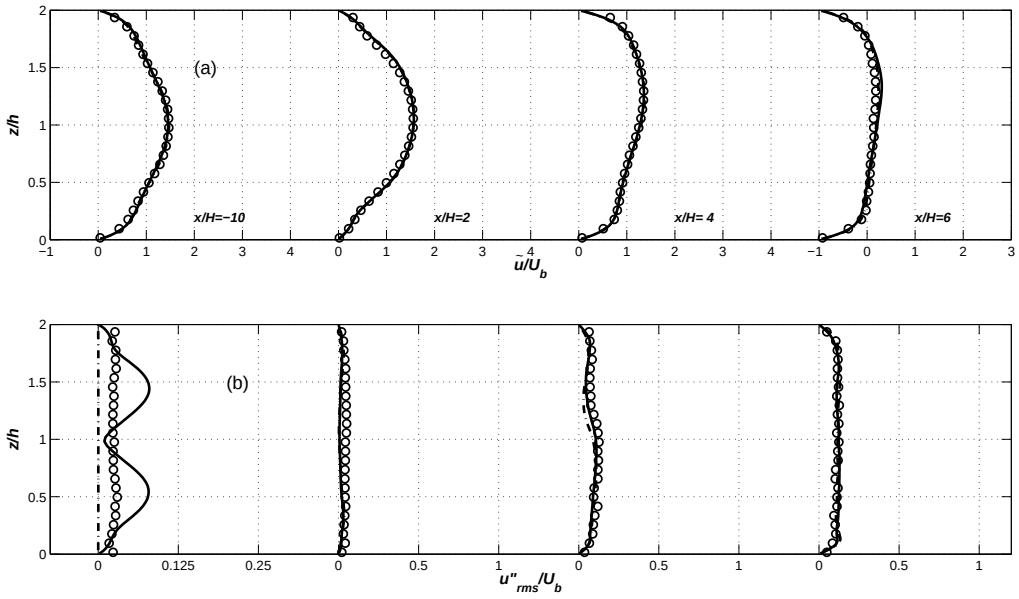

Figure 3.6: Phase-averaged statistics of the streamwise velocity at $\hat{t} \sim 3/2\pi$. $\circ$ experiment, —— Case 1, --- Case 2. (a) $\tilde{u}$; (b) u''_{rms}.

For each of the three phases shown in the corresponding figures, the phase-averaged mean streamwise velocity, $\tilde{u}$, at the upstream station, $x/H = -10$, is always in very good agreement with the experiment. This is expected, however, since this is the profile that is prescribed at the inflow plane should correspond to fully developed conditions. It also verifies, however, that the experimental and

interpolation errors are minimal, since the velocity does not change noticeably downstream of the inflow plane. On the other hand, the disturbances that are generated as a result of the inviscid instability in Case 1, develop both in space and time before reaching the stenosis. For this reason the distance of the inflow plane from the throat of the stenosis is also important. In the present computations we found that a distance of $10H$ to $15H$ was a good compromise between accuracy and efficiency. This is demonstrated by comparing profiles of incoherent streamwise fluctuations, u''_{rms}, for Case 1 to the experimental results at $x/H = -10$. Very good agreement can be observed. The only exception to this is found midway through the acceleration phase (Fig. 3.6b), where the simulations have more profound peaks compared to the experiment, evidently due to a slightly quicker decay of the disturbance in the experiment. As expected, in Case 2 where synthetic noise has not been added to the mean velocity profile, u''_{rms} remains zero upstream of the stenosis throughout the cycle.

Having demonstrated that the present approach reproduces the disturbance environment upstream of the stenosis with sufficient accuracy, we will now examine the influence of these disturbances to the flow downstream of the constriction. As shown in Fig. 3.6, midway through the acceleration, both Cases 1 and 2 agree well with the experimental results, indicating that during this part of the cycle the disturbance environment upstream of the stenosis has a minimal effect on the downstream flow. This is probably due to the negligible production of turbulence throughout the channel at this stage, as indicated by the nearly zero Reynolds shear stress (not shown in the figure). The relatively low levels of u''_{rms} at all downstream

stations (see Fig. 3.6b), are remains from earlier turbulent activity and are probably convected out of the channel. Also, from the corresponding mean profiles, a strong jet is visible that extends up to $x/H = 2$. Further downstream, the mean velocity profiles resemble that of a developing channel flow with a small asymmetry at $x/H = 4$.

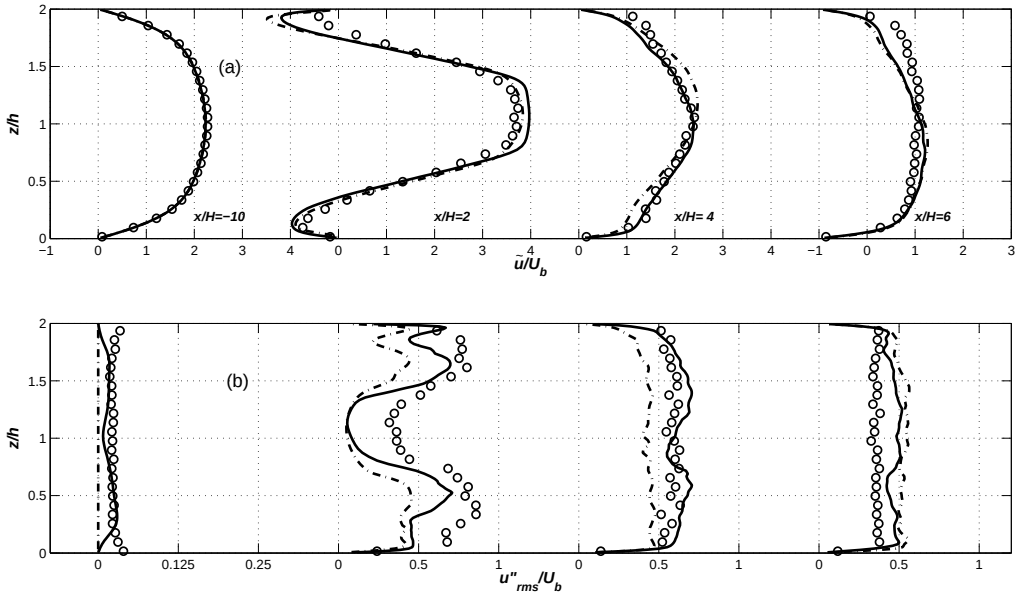

Figure 3.7: Phase-averaged statistics of the streamwise velocity at $\hat{t} \sim 2\pi$. ∘ experiment, —— Case 1, --- Case 2. (a) $\tilde{u}$; (b) u''_{rms}.

About the time of the maximum flow rate (see Fig. 3.7), the jet grows stronger and two recirculation bubbles are formed proximal to the stenosis. In addition, the thin shear layer that forms the edge of the jet becomes unstable and rolls up into, which subsequently interact with the recirculating areas and generates two distinct peaks in the u''_{rms} profile. Further downstream, the very high levels of u''_{rms} (approximately 50% of $\widetilde{U}_b$ at $x/H = 4$, and $x/H = 6$) are the result of the

break-up of the vortices into smaller vortical structures as they interact with the wall. During this part of the cycle, the upstream disturbance environment has a strong impact on the downstream statistics, and appears to have a substantial effect on the timing and localiztion of the shear layer breakdown. Case 1 (disturbed inflow conditions) agrees much better with the observed experimental results in comparison to those of Case 2 (undisturbed inflow). In the latter, the shear layer becomes unstable at a later time, affecting both $\tilde{u}$ and u''_{rms}. However, even for Case 1 some discrepancies with the experiment are visible, especially in the u''_{rms} level. This difference can be attributed to fact that the shear layer becomes unstable a little closer to the stenosis in the experiments, although this trend could not be confirmed with the current experimental data. As the flowrate decreases, the post-stenotic jet weakens and around $\hat{t} \sim \pi/4$ it becomes asymmetric. The u''_{rms} levels are also reduced as turbulent activity decays with decreasing Reynolds number. As it can be seen in Fig. 3.8, the agreement between the experiment and the DNS is excellent. Similarly to the mid-acceleration phase, the disturbance environment upstream during this phase of the cycle has a small influence on the downstream statistics, where turbulence is dissipated.

A more complete comparison between the experimental results and the simulation can be obtained by looking at iso-countours in the z/h versus t/T space of $< U >$ and $< u''_{rms} >$ across the channel at $x/h = 4$ and $x/h = 12$. The former location is within the recirculating area just downstream of the constriction, and the latter is downstream the mean reattachment point. Accompanying these figures are plots of the time evolution of $< u''_{rms} >$ at locations near the wall ($x/h = \pm 0.9$),

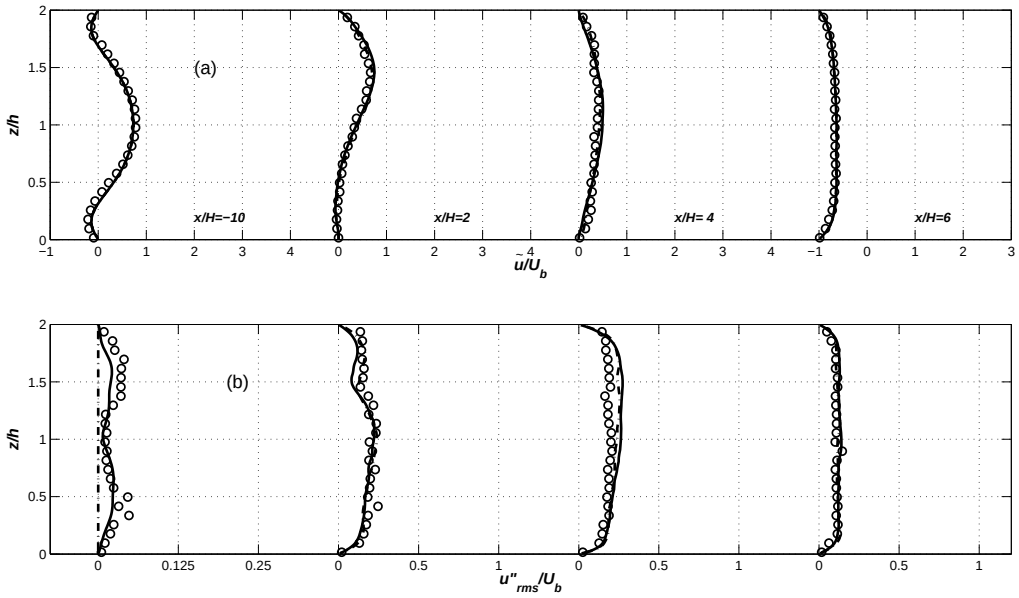

Figure 3.8: Phase-averaged statistics of the streamwise velocity at $\hat{t} \sim \pi$. $\circ$ experiment, —— Case 1, - - - Case 2.

at the height of the stenosis ($x/h = \pm 0.5$) and at the centerline ($x/h = 0$).

As it can be seen in figure 3.9a, a strong jet is formed near the stenosis as the flowrate increases. The jet is symmetric for most of the cycle, while towards the end of the deceleration (from now on, and unless otherwise stated, we will call 'deceleration phase' the part of the pulsatile cycle where the flowrate decreases from its maximum value at $t/T \sim 0.5$ to its minimum at $t/T \sim 1.0$, and 'acceleration phase' the remaining part from $t/T \sim 0.0$ to $t/T \sim 0.5$) it becomes asymmetric and gradually tilts towards the upper side of the channel. Near the wall, thick regions of reversed flow exist as indicated by the iso-contours of negative velocity. Qualitatively, the agreement with the experiment is excellent at this location, and the simulation captures accurately the formation and evolution of the confined jet

and the recirculation bubbles throughout the cycle. From a quantitative perspective, the simulations always compare within 8% of the experimental value, with a mean discrepancy of 5% (based on the mean bulk velocity).

The phase averaged, root-mean-square fluctuation of the streamwise velocity component, $< u''_{rms} >$, as plotted in figure 3.9b, highlights some important aspects of the dynamics of the shear layers at the edges of the jet. The rms levels during the early part of the acceleration are very small, indicating that any initial oscillations in the shear layer are coherent and repeatable from cycle-to-cycle. Later in the acceleration, however, the u''_{rms} levels increase sharply, pointing to a possible transition to a turbulent state. The $< u''_{rms} >$ levels remain high during most of the deceleration. The agreement between the simulation and the experiments is very good (within 5%), apart from a small interval, approximately $t/T = 0.80 - 0.95$, during which the latter are higher. This difference is most likely due to the fact that the confined jet becomes unstable a little closer to the stenosis in the experiments, although this trend could not be confirmed with the limited number of profiles sampled in the experiment. We can verify, however, that our simulations successfully capture the dynamics of the shear layers in the experiments, by comparing the power spectrum of streamwise velocity at this downstream location. Figure 3.11 shows a comparison of the frequency spectra at two positions selected to be within the top and bottom shear layers during the time interval $t/T = 0.30 - 0.40$. The dominant peak corresponding to the vortex shedding frequency of the shear layers can be clearly observed in both cases. The Strouhal Number ($N_s = 2\pi f h/\overline{U}_c$, where $\overline{U}_c$ is the time average centerline velocity at the throat of the stenosis) at both locations is

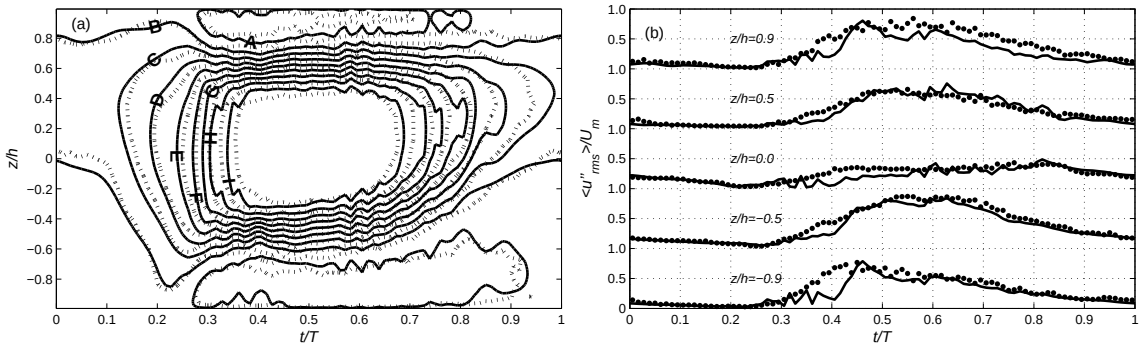

Figure 3.9: Spatiotemporal evolution of the phase-averaged statistics of (a) $< U > /U_m$ and (b) u''_{rms}/U_m at $x/h = 4$. ····· present experiment; —— case 1. Index values for the contour levels of $< U > /U_m$ are given by A=-0.18; B=0.38; C=0.76; D=1.13; E=1.15; F=1.89; G=2.26; H=2.63; I=3.01

approximately 7.7, and it is the same (within 1%) in the DNS and experiments.

The corresponding velocity statistics downstream of the mean reattachment point are also shown in figure 3.10. The absence of reversed flow patterns near the wall throughout the cycle indicate that the velocity profiles deviate considerably from the laminar solution. In particular, during the late acceleration and midway through the deceleration the velocity profiles exhibit a steep velocity gradient at the wall and a relatively flat shape towards the center of channel indicating that significant momentum transport takes places across the channel. The apparent turbulent nature of this region of the flow will be discussed in detail in section 4.2.2, with a focus on the turbulent kinetic energy budgets. As with the statistics at the location closer to the stenosis discussed above, the agreement with the experiment in this region is excellent.

Finally, a comparison of $< u''_{rms} >$ at $x/h = 12$ depicted in figure 3.10b shows the agreement with the experiment is very good at this location as well. This

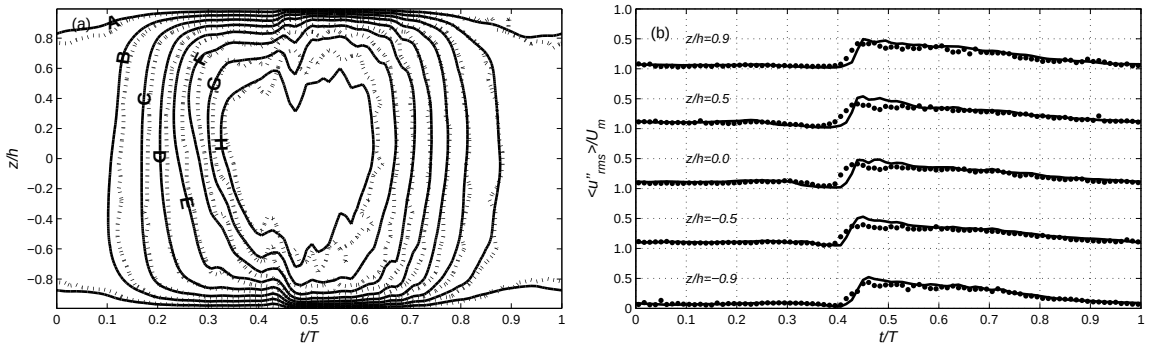

Figure 3.10: Spatiotemporal evolution of the phase-averaged statistics of (a) $< U > /U_m$ and (b) u''_{rms}/U_m at $x/h = 12$. ····· present experiment; —— case 1. Index values for the contour levels of $< U > /U_m$ are given by A=0.23; B=0.46; C=0.70; D=0.97; E=1.16; F=1.40; G=1.62; H=1.85

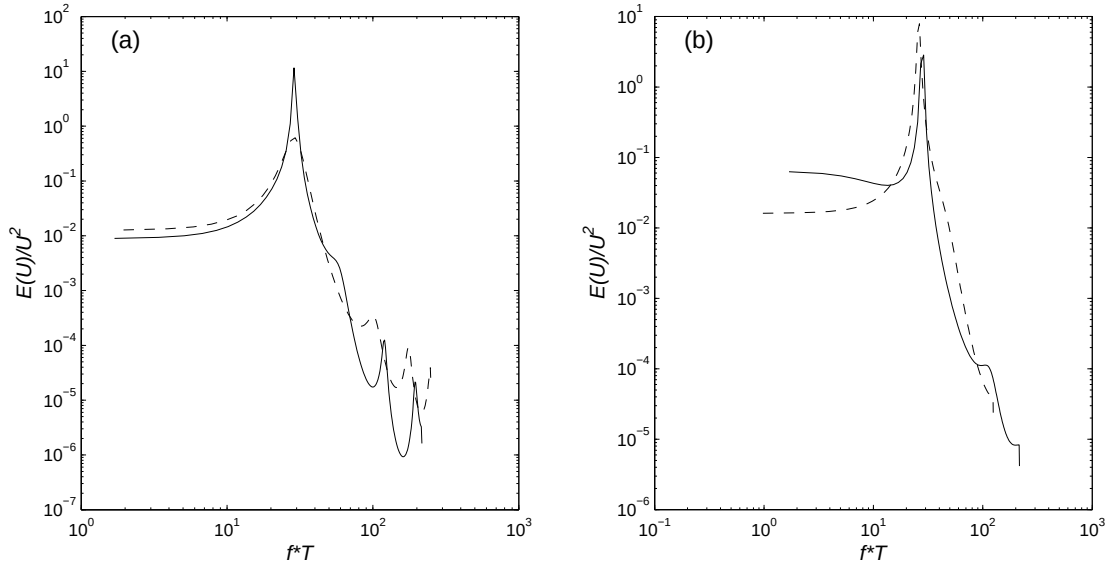

Figure 3.11: Autoregressive power spectra at $x/h = 4$ for segment of U between $t/T = 0.80-0.90$. —— case 1; - - - present experiment. (a) $z/h = -0.5$ and (b) $z/h = 0.5$. In both cases the kinetic energy in the segment has been used for normalization.

Case	Re	α	Domain Size	Grid Resolution	Inflow boundary condition
A	600	8.4	$60h \times 2\pi \times 2h$	$268 \times 32 \times 72$	$\widetilde{\vec{u}}_{exp} + \vec{u}''_{synthetic}$
B	600	8.4	$60h \times 2\pi \times 2h$	$402 \times 32 \times 106$	$\widetilde{\vec{u}}_{exp}$
C	600	8.4	$60h \times 2\pi \times 2h$	$598 \times 64 \times 106$	$\widetilde{\vec{u}}_{exp}$
D	600	8.4	$60h \times 4\pi \times 2h$	$402 \times 64 \times 106$	$\widetilde{\vec{u}}_{exp}$

Table 3.2: Set-up of simulations for establishing grid independency

reinforces the conviction that the simulation captures both qualitatively and quantitatively the essential features of the flow in the post-stenotic region. Interestingly, one may note that although during most of the acceleration the $< u''_{rms} >$ levels are low, there is a sudden spike in the streamwise turbulent intensity just before the peak flow rate. This burst in incoherent fluctuations in the wall layer lags the one observed at $x/h = 4$ by about $0.12t/T$. If one assumes that the observed jump in $< u''_{rms} >$ stems from an evolution of the incoherent fluctuations noted upstream, the resulting propagation velocity is calculated to be equal to the local mean velocity during that time interval ($1.2U_m$). Therefore, this 'turbulent' front can be plausibly linked with the break-down of the vortices originating in the mixing layer. This process will be discussed in greater detail in the following section.

The above comparisons with the experimental results suggest that the grid resolution is sufficient to capture the detailed dynamics of the flow. However, since comparisons were confined to the streamwise velocity (the only one available from

the LDV experiment), we also performed a grid refinement study to examine the sensitivity of all velocity components to the grid resolution. Table 3.2 shows a summary of the different cases and grids used in this study. In Fig. 3.12 the time-averaged velocity statistics are shown for Cases A, B, and C. The corresponding experimental results have been added for the streamwise velocity. Referring to Table 3.1, Case B is the baseline case; Case A has 50% fewer points in all three directions compared to baseline case; Case D has 50% more points in the streamwise and spanwise directions and corresponds to case 1 for which results were shown above.

From all the statistics shown in Fig. 3.12 it is evident that the coarse grid (Case A) is not sufficient to capture the dynamics of the flow. In particular, the mean streamwise and wall-normal velocity profiles near the stenosis ($x/H = 2$) are fairly symmetric, contrary to what is observed in the experiment. In addition, for the same station, all velocity fluctuations (u'_{rms}, v'_{rms}, w'_{rms}) are under-predicted and the Reynolds stress, $u'w'$, is practically zero. Further downstream ($x/H = 4$ and $x/H = 6$) the differences are smaller but not negligible. The two fine grids however, agree very well for all velocity components indicating that the resolution in Case 1B is sufficient to capture the dynamics of the flow.

Finally the sensitivity of the statistics to the spanwise domain size was examined. Case D has twice the domain size in the spanwise direction compared to the baseline case (Case B), while it uses the same grid resolution. As it can been seen in Fig. 3.12, the agreement with Case B is excellent indicating that the spanwise domain size for the baseline case is sufficient to accommodate the largest structures

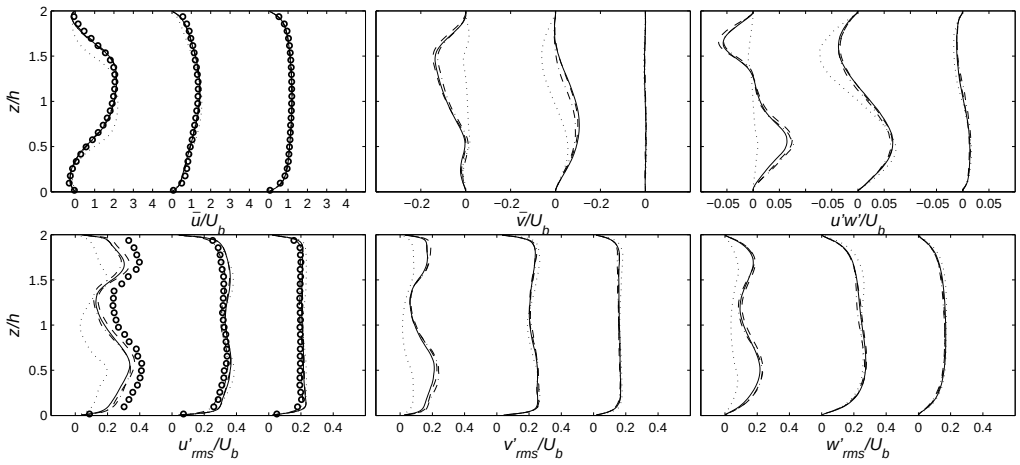

Figure 3.12: Time average velocity statistics at $x/H = 2$, $x/H = 4$, $x/H = 6$. ····· Case A; —— Case B; —·— Case C; - - - Case D.

present in the flow.

3.5 Inflow conditions for the axisymmetric configuration

In the present study we have also considered axisymmetric configurations. Given the profound effects of the disturbance environment at the inlet in the planar cases examined above, in this section we will examine the sensitivity of the axisymmetric cases to this environment. We performed a series of computations using the cylindrical coordinate solver with different disturbance levels at the inlet. The effect of the disturbance environment in axisymmetric configurations has also been examined recently by Sherwin *et al.* [53] at a mean Reynolds number of 300. They found that in the absence of any disturbance on the velocity profile at the inlet the shear layer remained stable throughout the pulsatile cycle. Only when they introduced a small-amplitude high frequency forcing to the inflow, they observed a convective

shear-layer instability, which reduced the axial distance downstream from the stenosis where turbulent breakdown occurs compared to the unperturbed case. Table 3.3 summarizes the three cases ivnestigated in the present work. In all cases the velocity profile from the analytical solution is prescribed. In case 6A random noise fluctuations are added to all velocity components at the inflow. The fluctuations are high enough (about 10% of the local mean velocity) so as not decay immediately within one grid cell and thus trigger any instabilities associated with the inflection points in the velocity profile. In case 6B, which is equivalent to case 6 from table 4.2, a small amplitude (0.1% of the mean flow) high-frequency ($50th$) harmonic is added to the inflow, similar to the high-frequency forcing applied by Sherwin [53] in their simulations. Finally case 6C is a simulation with no disturbances at the inflow, and as a result the flow upstream of the stenosis remains in an undisturbed laminar state throughout the cycle. Figures 3.13-3.15 show comparisons of the phase-averaged axial velocity profiles and rms levels across the pipe for all three cases. In each figure, four axial locations are shown: $x/R = -20$, $x/R = 8$, $x/R = 12$, $x/R = 20$. The first station is upstream of the stenosis, and is used to assess the state of the flow, while the other three stations are downstream of the stenosis. Each figure refers to one characteristic instance in the pulsatile cycle: midway through the acceleratiom in figure 3.13, later in the acceleration during the roll-up process in figure 3.14 , and midway through the deceleration in figure 3.15.

In all three instances the flow upstream of the stenosis for the case with random noise has considerable levels and distinct shapes of $u"_{rms}$ suggesting that a transition to a disturbed laminar state is probably triggered through an inviscid instability (the

Case	Re_m	U_{red}	K	Domain Size	Grid Resolution	Inlet Conditions
6A	600	26.5	1.75	$70R \times 2\pi \times 1R$	$834 \times 64 \times 54$	$\tilde{u}_{analytical}$+ random noise
6B	600	26.5	1.75	$70R \times 2\pi \times 1R$	$834 \times 64 \times 54$	$\tilde{u}_{analytical}$+ h.f. forcing
6C	600	26.5	1.75	$70R \times 2\pi \times 1R$	$834 \times 64 \times 54$	$\tilde{u}_{analytical}$

Table 3.3: Summary of cases with different disturbance environment at the inflow in cylindrical configuration.

velocity profiles during the later part of deceleration exhibit inflection points). The shape and magnitude of the $u"_{rms}$ also changes during the cycle as the instability triggered near the inflow creates disturbances that propagate downstream. For case 6B the $u"_{rms}$ levels are always below 0.5% of the mean bulk velocity and do not have any particular shape representative of a transition to a disturbed laminar state. As shown in figure 3.14 corresponding to the phase in cycle during the initial roll-up of the shear layer, the arrival of the disturbances in case 6C triggers the breakdown of the start-up structure a little closer to the stenosis. As a result the flow reattaches before $x/R = 20$ for case 6C while for the other two cases the flow has not yet reattached at $x/R = 20$. Instantaneous flow visualizations (not shown here) confirm this trend and also reveal that the transition occurs a little earlier in the cycle. Following the breakdown of the start-up structure and until midway in the deceleration, the shear layer becomes unstable in all cases. However for case 6C the breakdown of the vortex-rings occurs closer to the stenosis. This is clearly seen in figure 3.15 where at $x/R = 8$ corresponding to the location of the shear layer

roll-up the $u"_{rms}$ are higher for case 6C than in the other two cases. In addition the velocity profiles at $x/h = 12$ reveal that the flow in case 6C has already reattached while in the other two cases the flow is about to reattach. In general there are no differences between the case with no disturbances at the inflow and the high frequency forcing case for this set of Reynolds number and reduced velocity. This is expected as in both cases, the flow upstream of the stenosis remains in a laminar state throughout the cycle. Even when random noise is added at the inflow, the qualitative features of the flow in the post-stenotic region remain the same. For all the cases in cylindrical coordinates high frequency forcing was chosen over random noise since a change in the reduced velocity would result in a different arrival time of the disturbances at the stenosis.

From the above simulations it is clear that for the range of Reynolds number and reduced velocity investigated the noise added at the inlet (either synthetic or random) triggers inviscid instabilities in both planar and cylindrical configurations. These instabilities evolve into coherent disturbances that propagates downstream and can accelerate the breakdown of the shear layer. Knowledge of the disturbance environment upstream of the stenosis is therefore an important parameter in these types of biological flows.

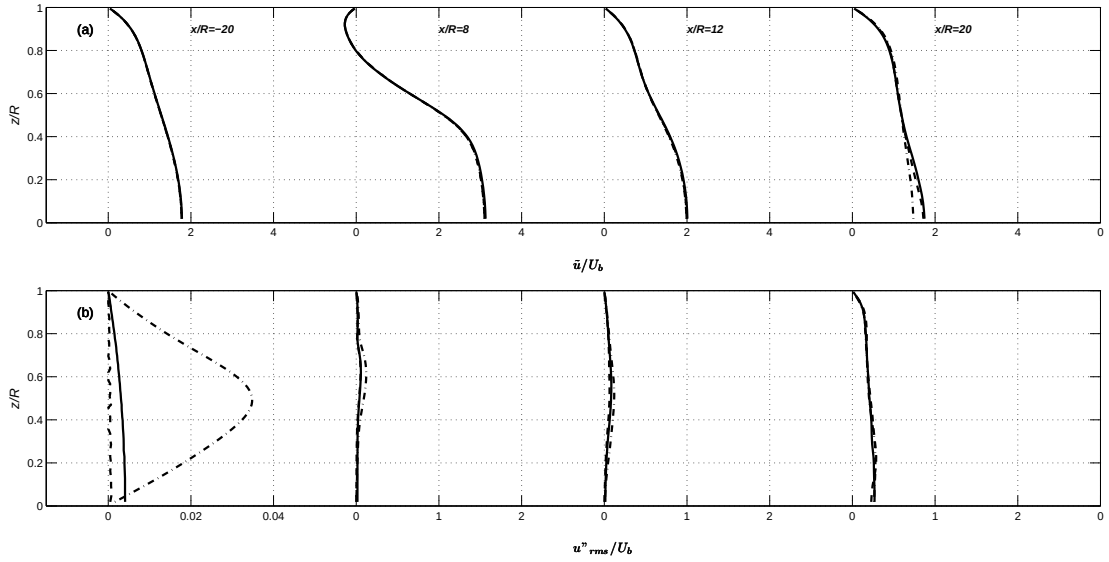

Figure 3.13: Phase-averaged statistics of the streamwise velocity at $t/T = 0.25$. —·— Case 6A, —— Case 6B, - - - Case 6C. (a) $\tilde{u}$; (b) u''_{rms}.

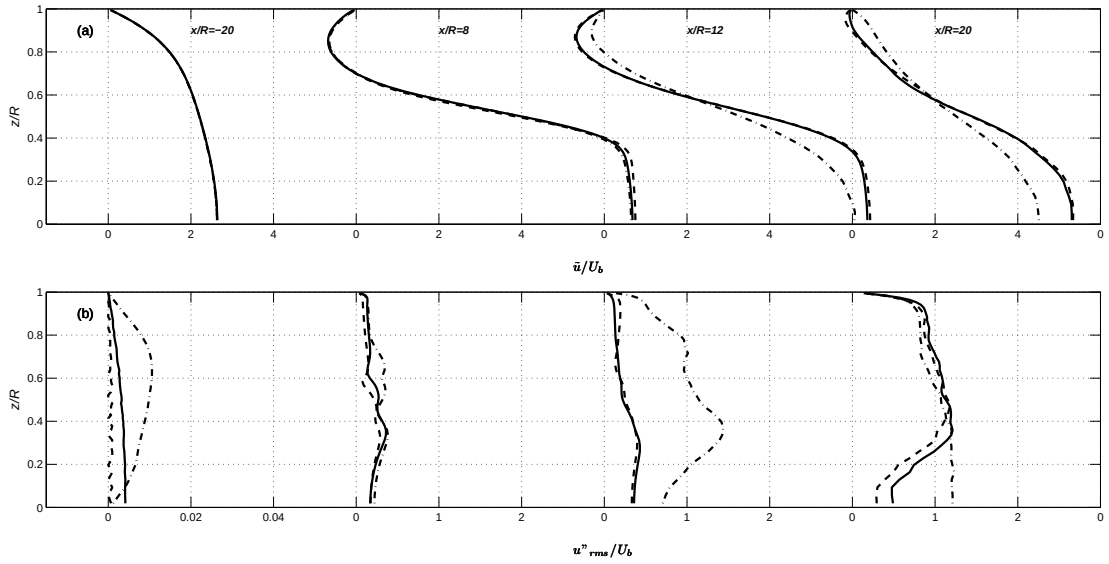

Figure 3.14: Phase-averaged statistics of the streamwise velocity at $t/T = 0.42$. —·— Case 6A, —— Case 6B, - - - Case 6C. (a) $\tilde{u}$; (b) u''_{rms}.

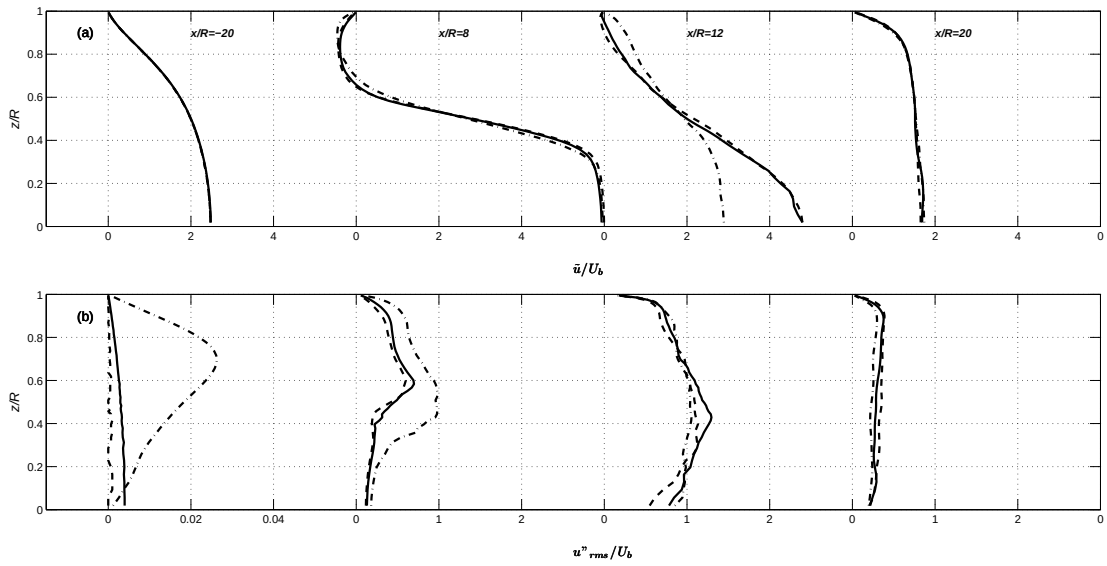

Figure 3.15: Phase-averaged statistics of the streamwise velocity at $t/T = 0.70$. —·— Case 6A, —— Case 6B, - - - Case 6C. (a) $\tilde{u}$; (b) u''_{rms}.

Chapter 4

Flow Physics

Having established the accuracy of the simulations in reproducing the complex transitional flow patterns in the experimental apparatus, the discussion in this section will utilize the wealth of information provided by the simulations to explore the instantaneous flow dynamics in more detail. First, the parametric space covered in both Cartesian and cylindrical coordinates is given. We will then discuss the dynamics of the flow in the planar configuration by identifying the coherent structures that dominate the dynamics of the flow and explore their spatio-temporal evolution. The effect of these structures on the phase-averaged statistics, and the way turbulent kinetic energy is produced, transported, and dissipated will be presented in the subsequent section. Results from the axisymmetric configuration are given last. Two distinct transition mechanisms are investigated: i) the initial roll-up structure and ii) the shear layer instability. The effect of the reduced velocity and Reynolds number on these mechanisms is explained. Finally phase-averaged velocity and wall shear stress statistics are discussed.

4.1 Parametric Space

The flow conditions upstream of the constriction are defined using the following parameters: the mean Reynolds number $Re_m = U_m h/\nu$, (U_m is the time average

bulk velocity and ν the kinematic viscosity, and h is either the half channel height in the case of the planar geometry or the radius of the pipe in the case of the axisymmetric geometry); the Womersley number, $\alpha = h(2\pi/T\nu)^{0.5}$, ($T$ is the period of the pulsation); and the non-dimensional amplitude of the oscillations, K, defined as the ratio of the maximum bulk velocity, U_{max} to U_m. The reduced velocity, $U_{red} = U_m T/2h$, is also a useful parameter and can be interpreted as the mean convective length to the channel height. Note that U_{red} is not an independent parameter and is related to the Reynolds number and α according to the relation: $U_{red} = \pi Re/\alpha^2$.

The reason we chose to investigate the planar channel first is that compared to an equivalent axisymmetric configuration, where usually the mean flow is three-dimensional and unsteady, the planar configuration allows for spatial averaging along the homogeneous (spanwise) direction. This increases substantially the statistical sample making feasible the convergence of higher order statistics. The parametric space was chosen to be within the physiologic regime considered in prior *in vitro* experiments available in the literature for the purpose of investigating the robustness and repeatability of the observed flow phenomena. The $Re - \alpha$ parametric space obviously does not account for all factors that can influence the dynamics of such flows (i.e., curvature, wall roughness, non-sinusoidal flow rate, wall compliance, rheological effects, etc.). As we will discuss in the result section, however, the flow physics reproduced in this simplified configuration are qualitatively similar to the ones reported in a variety of *in vivo* and *in vitro* experiments with a various degrees of complexity, thus allowing for a more detailed understanding of the relevant first-

order fluid dynamic effects associated with post-stenotic transition.

Table 4.1 summarizes the range of these parameters in our simulations for the planar configuration. We considered three different forcing frequencies ($4.2 < \alpha < 16.8$) and two Reynolds numbers ($Re_m = 600$ and 1200) while keeping the amplitude of the oscillations constant. This way the reduced velocity also varies from $U_{red} = 6.6$ to 106.2. In all cases except case 1, the temporal characteristics of the bulk velocity consist of a mean plus a single harmonic. For case 1, however, the flow rate was set to match that of the experiment, which deviates from a single-frequency sinusoid due to limitations in fine-tuning the spool valve in the experimental apparatus. To quantify the effect of this small deviation on the results, we compared first and second order velocity statistics between cases 1 and 3. The results between these two cases were very close and therefore we consider these two cases as equivalent.

For the cylindrical configurations the cases investigated are shown in table 4.2. The domain in this case extends 20 diameters downstream of the stenosis. Consequently additional points are used in the axial direction to maintain sufficient resolution within 10 diameters from the stenosis. In the first three cases the Reynolds number is 600 and the reduced velocity is varied similarly to the cases with the planar configuration. This way a direct comparison between the two different geometries is possible. A simulation at Reynolds of 1200 but the same reduced velocity of 26.5 was performed to estimate the effects of Reynolds number.

Case	Re_m	α	U_{red}	K	Domain Size	Grid Resolution	Inlet Conditions
1	600	8.4	26.5	1.75	$60h \times 2\pi \times 2h$	$598 \times 64 \times 106$	$\tilde{u}_{experiment}$+ noise
2	600	16.8	6.6	1.75	$60h \times 2\pi \times 2h$	$598 \times 64 \times 106$	$\tilde{u}_{analytical}$+ noise
3	600	8.4	26.5	1.75	$60h \times 2\pi \times 2h$	$598 \times 64 \times 106$	$\tilde{u}_{analytical}$+ noise
4	600	4.2	106.2	1.75	$70h \times 2\pi \times 2h$	$834 \times 64 \times 106$	$\tilde{u}_{analytical}$+ noise
5	1200	8.3	53.1	1.75	$70h \times 6 \times 2h$	$598 \times 128 \times 54$	$\tilde{u}_{analytical}$+ noise

Table 4.1: Summary of cases studied in planar configuration.

Case	Re_m	α	U_{red}	K	Domain Size	Grid Resolution	Inlet Conditions
6	600	8.4	26.5	1.75	$70R \times 2\pi \times 1R$	$834 \times 64 \times 54$	$\tilde{u}_{analytical}$+ noise
7	600	16.8	6.6	1.75	$70R \times 2\pi \times 1R$	$834 \times 64 \times 54$	$\tilde{u}_{analytical}$+ noise
8	600	4.2	53.1	1.75	$80R \times 2\pi \times 1R$	$1026 \times 64 \times 54$	$\tilde{u}_{analytical}$+ noise
9	1200	8.4	26.5	1.75	$70R \times 2\pi \times 1R$	$834 \times 64 \times 54$	$\tilde{u}_{analytical}$+ noise

Table 4.2: Summary of cases studied in axisymmetric configuration.

4.2 Planar Configuration

4.2.1 Instantaneous Flow Dynamics

As the flowrate starts to increase from its minimum value at $t/T \sim 0.0$, a confined jet starts to form through the constriction. To illuminate the basic flow patterns during the initial stages of the jet formation, figure 4.1 shows iso-contours of the instantaneous spanwise vorticity at an $x-z$ plane for case 1 from four instances during the interval $0.0 < t/T < 0.5$. In the proximal area downstream of the constriction, the flow remains quasi two-dimensional during this period, indicating that these contours are a good representation of the flow throughout the spanwise direction. Superimposed on the contours are velocity streamlines highlighting the shape and evolution of the recirculating zone. Initially, the attached thin shear layers that form on the walls of the stenosis separate due to the adverse pressure gradient induced by the expansion in the geometry, and create a closed separated area just downstream of the constriction (see figure 4.1a). During this early stage, the vorticity imparted into the shear layers is primarily convected downstream along the edge of the recirculation bubble. At $t/T = 0.23$ (see figure 4.1e), the shear layer begins to curl towards the wall, but does not immediately roll-up into a vortex, as is often found in starting transients of free jets. This is most likely due to the close proximity of the solid boundaries, but may also be delayed by strong diffusion effects at these relatively low Reynolds numbers. Later in time though ($t/T = 0.28$), the vorticity at the tip of the shear layer eventually does initiate a roll-up into a small vortical structure, as shown in figures 4.1b and f. This structure (labeled

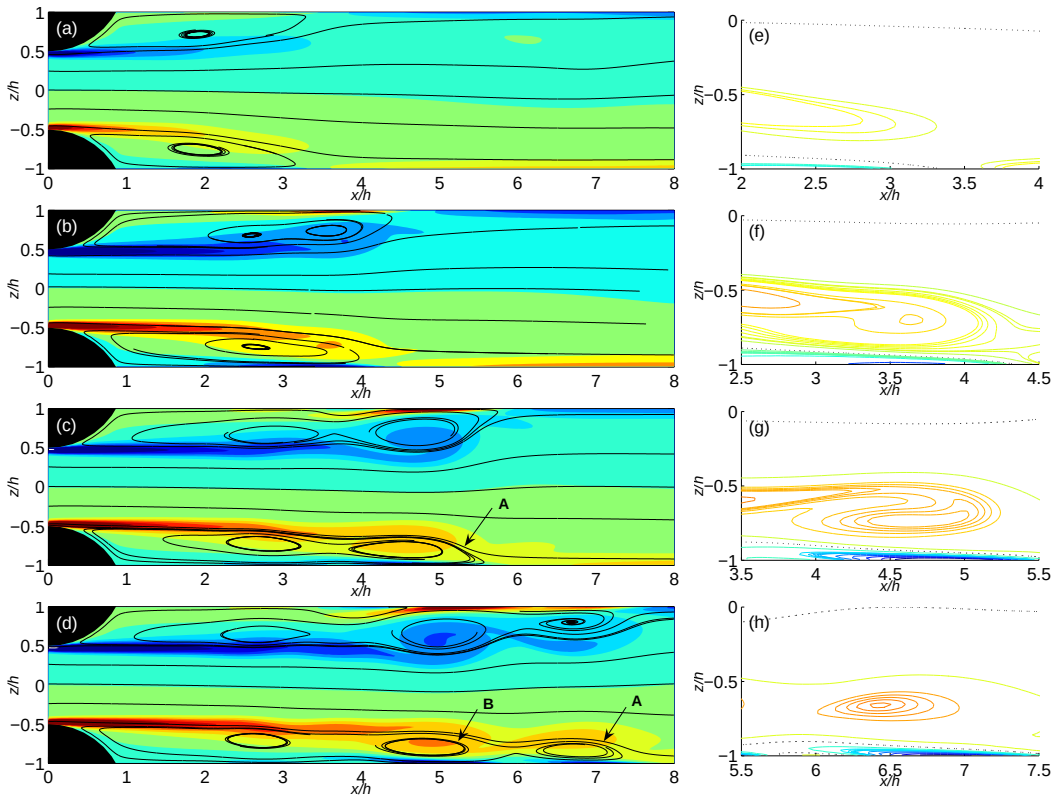

Figure 4.1: Filled iso-contours of spanwise vorticity and velocity streamlines for case 1 at four instances during the acceleration (a-d) and detailed iso-contour lines of spanwise vorticity following the downstream edge of the vortex sheet (e-h). The dotted line in (e-h) represents the iso-contour of zero spanwise vorticity. (from top to bottom (a,e); $t/T = 0.23$, (b,f); $t/T = 0.28$, (c,g); $t/T = 0.32$, (d,h); $t/T = 0.36$).

A) gradually gains strength, and at $t/T \sim 0.32$ detaches from the shear layer as indicated by the shape of the streamlines and the vorticity contours in figures 4.1c and g.

As a possible explanation for the observed behavior, one may speculate that the formation dynamics of the leading structure, A, share some of the features found in round jets accelerating in a quiescent unbounded environment [15, 45]. In such a case, the shear layer around the edge of the jet rolls-up, forming a vortex with a circulation that continues to grow until a critical threshold is reached: at this

point the vortex disconnects from the trailing jet and propagates on its own speed. This process has also been found to have a universal scaling characterized by a non-dimensional time-scale of the pinch-off, referred to as the 'formation number' [15]. To elucidate the dynamics of the initial shear layer roll-up and robustness of the 'pinch-off' process in our simulations we compared the results from all the different cases in Table 1. The temporal and spatial localization of the initial roll-up is a complicated process likely influenced by the Reynolds number, frequency and amplitude of the oscillations as well as the geometry of the constriction. For our limited range of parameters, however, it is observed to vary strongly with the reduced velocity. In Figure 4.2, selected iso-contours of the instantaneous spanwise vorticity are shown at an $x-z$ plane. As U_{red} increases (top to bottom in the figure) the jet becomes longer and the 'pinch-off' occurs farther downstream. In addition, the initial shear layer roll-up occurs earlier in time relative to the period of pulsation. Similar trends have also been observed in simulations [45] and experiments [15] of round jets accelerating in a quiescent unbounded environment. In our case, however, we did not find the same universal 'formation number' as in the above studies. This is likely due to the fact that in a confined jet the proximity of the walls dominates the overall dynamics.

Following the 'pinch-off' of structure A, a series of detached vortices form by the time the flowrate is close to its maximum value. A typical example of the flow at this time is shown in figure 4.1d where the structure B (indicated by the arrow) is clearly visible behind A. The generation of the above structures is likely the result of an instability of the shear layers. In particular, inspecting a series of animations

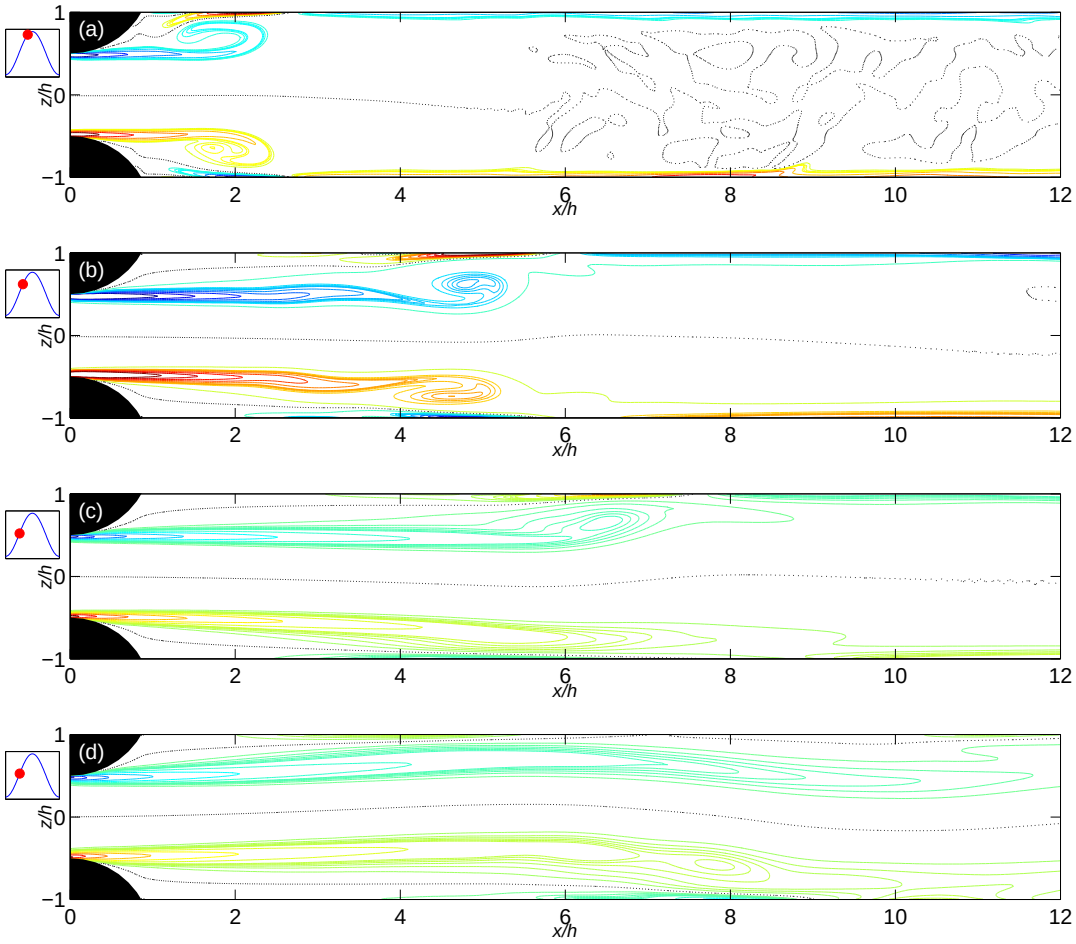

Figure 4.2: Selected iso-contours of spanwise vorticity and velocity streamlines at a characteristic instance during the initial shear layer roll-up. The dotted line represents the iso-contour of zero spanwise vorticity. (a) case2, $U_{red} = 6.6$, $t/T = 0.41$; (b) case3, $U_{red} = 26.5$, $t/T = 0.32$; (c) case5, $U_{red} = 53.1$, $t/T = 0.26$; (d) case4, $U_{red} = 106.2$, $t/T = 0.26$.

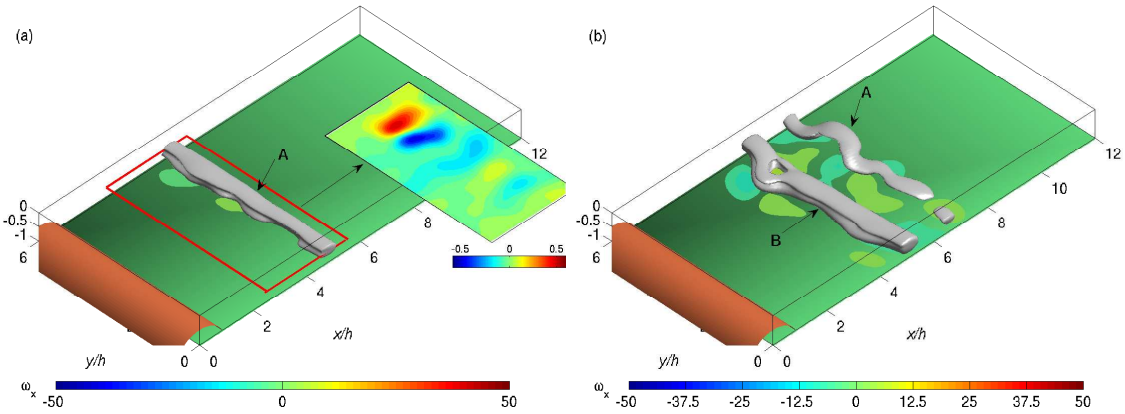

Figure 4.3: Early stages of the formation and evolution of coherent spanwise structures in case 1 visualized by iso-surfaces of Q. The time instants for the left and right parts correspond to the ones shown in figures 4.1c and d respectively. Selected contours of $(dU/dy)h/U_m$ are shown at a slice through the vortex in (a). Values of contours are ± 0.1, ± 0.2, ± 0.3 and ± 0.4, with negative values represented by dotted lines. Only the bottom half of the channel is shown and filled iso-contours of $\omega_x h/U_m$ are plotted on the wall.

and velocity time series generated from the DNS database, small oscillations were observed in the shear layers as early as $t/T \sim 0.2$. They gradually increased in amplitude and eventually lead to the local collapse of the recirculation bubble and the formation of the detached structures shown in figure 4.1. A similar Kelvin-Helmholtz like instability has been observed in impulsively accelerating jets [45, 15] and has been shown to affect the evolution of the detached leading vortex described earlier [63]. Sherwin *et al.* [53] also suggested that the jet shear layers are most likely subject to a convective instability, which was based on the high receptivity of their DNS to a well-defined frequency band, as well as the absence of vortex formation in their unforced simulations.

Following the initial formation of these quasi two-dimensional detached vortical structures, we looked into the details of their spatio-temporal evolution and

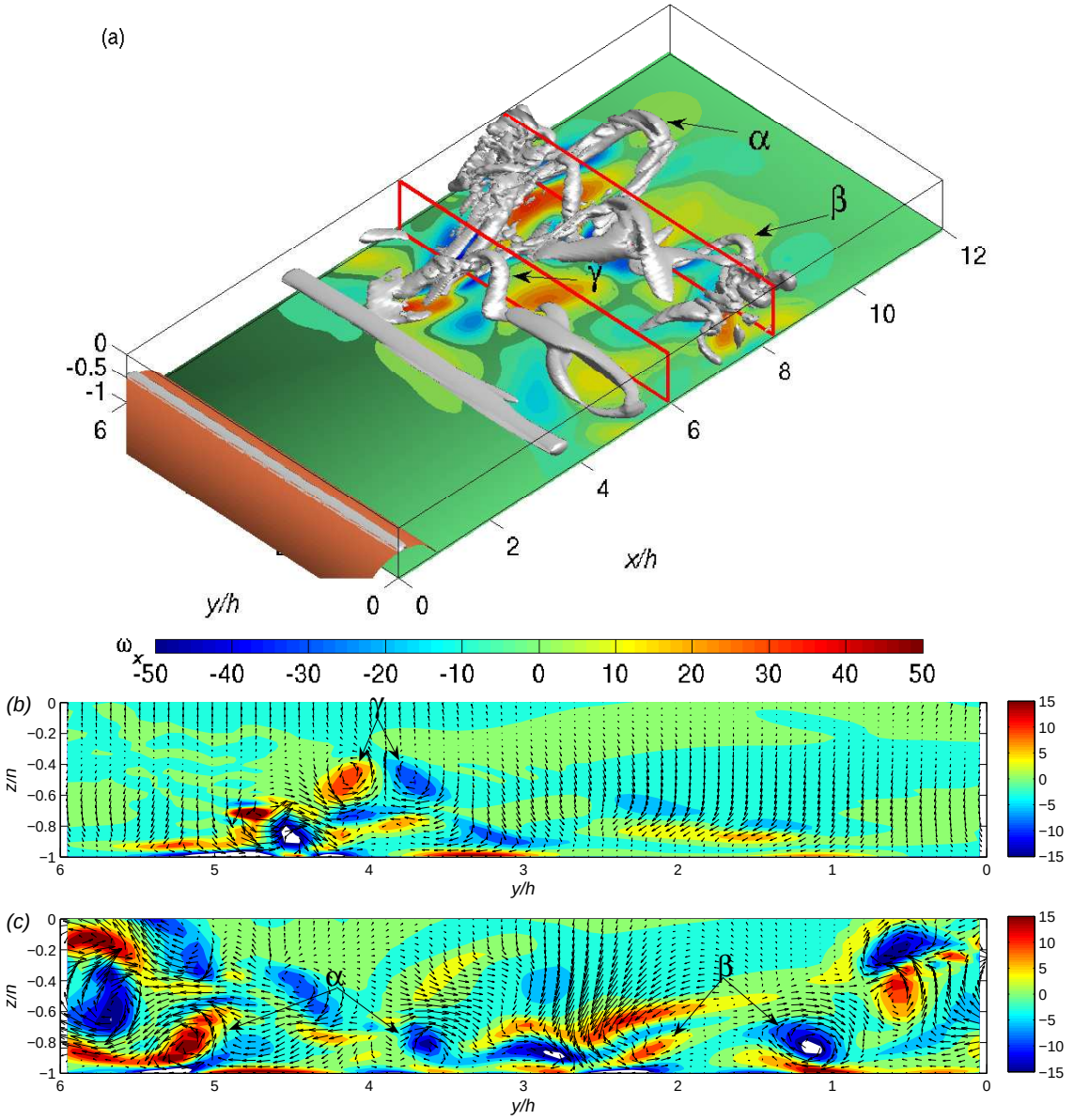

Figure 4.4: (a) A snapshot of the dominant coherent structures in case 1 visualized by iso-surfaces of Q, shortly before the maximum flowrate ($t/T = 0.4$). Only the bottom half of the channel is shown and iso-contours of streamwise vorticity, $\omega_x h/U_m$ are plotted on the wall. (b)-(c) Instantaneous distribution of $\omega_x h/U_m$ at the two y-z planes indicated on part (a) of the figure. In-plane, instantaneous velocity vectors are also shown. Arrows in all parts of the figure point to the hairpin-like structures.

their role in the initiation of turbulence. Figures 4.3a and 4.3b show snapshots of the instantaneous flow structures at two instances in time (same case as in figures 4.1c and 4.1d respectively). Iso-surfaces of the 2^{nd} invariant of the velocity gradient tensor, or Q-criterion (see [8]), on the lower half of the channel are shown to visualize the vortical structures, while contours of the streamwise vorticity are plotted on the bottom wall. Figure 4.3a shows that the first vortex to detach from the shear layer (indicated by A in the figures) is initially very coherent and uniform along the span of the channel, and as it is convected downstream, it undergoes a three-dimensional instability and evolves into what resembles a Λ-type structure (see figure 4.3b). The vortices that subsequently form behind structure A (see structure B in the same figure) undergo a similar evolution. For all cases listed in table 4.1, the above appears to be the primary mechanism that is responsible for the reorientation of spanwise vorticity into streamwise vorticity, which will eventually lead to the formation of streamwise vortex packets. This conjecture is consistent with the presence of strong spanwise gradients (see the insert in figure 4.3a near $y/h = 5$) during the early stages of this process, indicating that the dominant production term in the transport equation for streamwise vorticity is $\omega_y \partial U/\partial y$ (this was subsequently verified by direct computation of all stretching terms in the above transport equation). Such mechanisms for reorientation of spanwise vorticity are common in numerous free-shear and wall-bounded flows [see for example [26, 21]]. The observed asymmetry in the spanwise gradients and their resulting deformation is probably due to small scale disturbances that remain in the post-stenotic region from previous cycles.

As this instability evolves, the initially quasi two-dimensional rollers lose most

of their spanwise coherence, and their subsequent interaction with the wall generates packets of hairpin-like vortices. Figure 4.4a shows selected iso-surfaces of the Q criterion at $t/T = 0.4$ and velocity vectors on two $y - z$ planes across the wall. As can be seen, the downstream edge of the structures shown in the figure consists of pairs of horseshoe-like vortices, reminiscent of the near wall structures seen in turbulent boundary layers. These vortices are made up of two legs that are almost parallel and close to the wall, and a head region that extends away from the wall. Spanwise cuts through the flow reveal pairs of counter-rotating steamwise vorticity that correspond to the legs of the hairpin vortices (structures α, β and γ indicated by arrows in figure 4.4). It is evident that these hairpin vortices are the direct evolution of the detached structures shown in figure 4.3. Furthermore, these hairpin-like structures induce other streamwise vortical structures, creating a highly three-dimensional and random flow field, which starts to generate disturbances within the structures upstream.

As the flowrate starts to decrease ($t/T \sim 0.5$) the disturbances generated from the evolution and breakdown of the above mentioned vortical structures slowly propagate upstream. This can be clearly seen in figure 4.5, where the variation along x of the spanwise averaged turbulent kinetic energy, k, is shown at three instances in the pulsatile cycle. As time increases, a disturbance front travels upstream approaching $x/h = 2$. The dynamics of the shear layers, which now have a shedding frequency of approximately twice the one observed for $t/T < 0.5$, also change substantially. Figure 4.6 shows contours of the instantaneous spanwise vorticity at an $x - z$ plane, located approximately at channel center-span, at two characteristic instants during

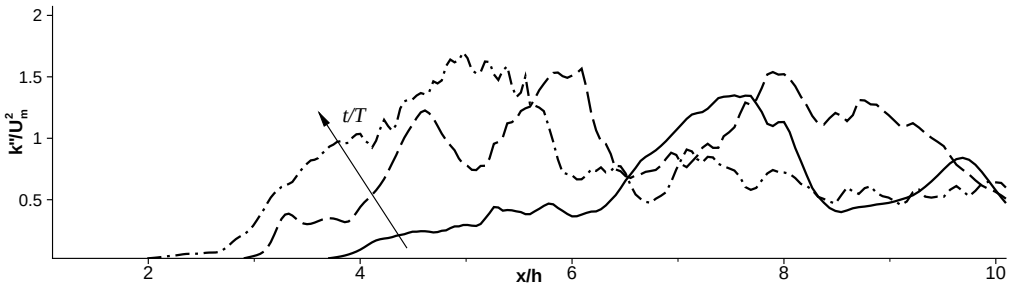

Figure 4.5: Spanwise averaged turbulent kinetic energy (case 1). Streamwise variation at $z/h = -0.5$ at three instances in the pulsatile cycle: —— $t/T = 0.4$; - - - $t/T = 0.45$; —·— $t/T = 0.5$

the period $0.5 < t/T < 1.0$. At $t/T \sim 0.58$ (see figure 4.6a) a distinct roll-up of the shear layer is observed at $x/h = 4$. In contrast to figure 4.1, a well defined shear layer extends only up to $x/h = 4$, beyond which only smaller elongated structures can be distinguished across the channel. This is also reflected on the instantaneous skin friction coefficient (see figure4.6c), which shows that the vortices shed by the shear layer quickly loose their spanwise coherence as they convect beyond $x/h > 5$. In addition, smaller structures originating from break-ups having occurred downstream can be clearly seen inside the recirculation bubble in figure 4.6b, where they get entrained by or merge with the shear layers. This points to the fact the shear layer instability is no longer convective but it attains a rather absolute nature.

A snapshot of the characteristic coherent structures during this part of the cycle is shown in figure 4.7. A quasi two-dimensional spanwise roller can be seen at $x/h \sim 3$, and just downstream another roller undergoes a three-dimensional instability. Between the two rollers, there is a 'braid' region where several counter-rotating rib vortices exist. The strength of these vortices is better illustrated in figure 4.7b,c where instantaneous iso lines of streamwise vorticity, ω_x, at $y - z$

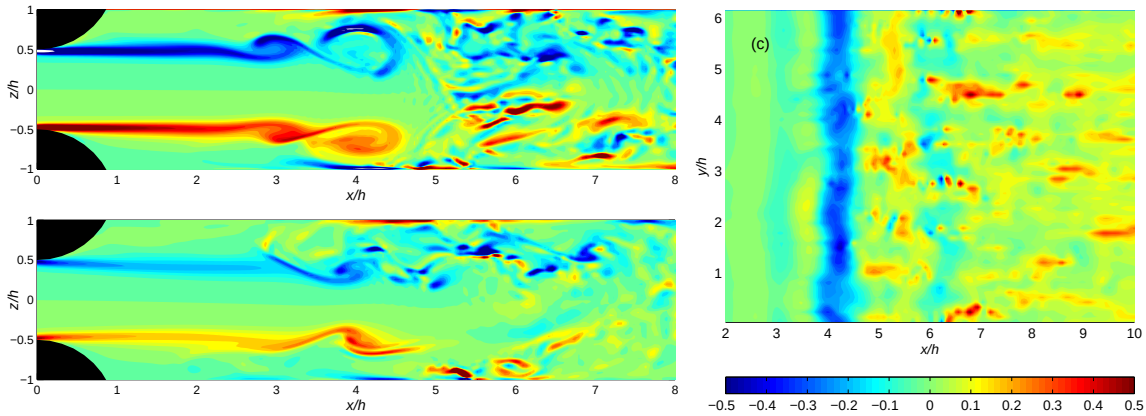

Figure 4.6: Iso-contours of instantaneous spanwise vorticity ($\omega_y h/U_m$) at two instances during the deceleration in case 1; $t/T = 0.58$ (a), $t/T = 0.77$ (b) and plot of $\omega_y h/U_m$ on the bottom wall at $t/T = 0.58$ (c).

planes located in the braid regions are shown. The overall picture resembles that of a mixing layer, indicating that the shear layers during this part of the cycle undergo both Kelvin-Helmholtz type, as well as three-dimensional braid instabilities.

The nature of this instability was also assessed by looking at how the dominant frequencies of vortex shedding change throughout the cycle. Figure 4.9 shows the Strouhal number calculated using the 'slotting' technique described in Chapter 3 applied on the wall-normal velocity signal at $x/h = 2$, $z/h = 0.5$, every $dt/T = 0.10$ segments. On the same plot are shown the frequencies predicted from the quasi-steady stability analysis are shown. They have been computed from the shear layer thickness and velocity difference across shear layer at $x/h = 0.5$, at the corresponding time instants. In the part of the cycle between $t/T = 0.3 - 0.7$, where the roller and rib vortices associated with the classical Kelvin-Helmoltz instability have been observed, the Strouhal numbers are in a fairly good agreement with the quasi-steady analysis (within 8%). During this part of the cycle there is also a lower range of

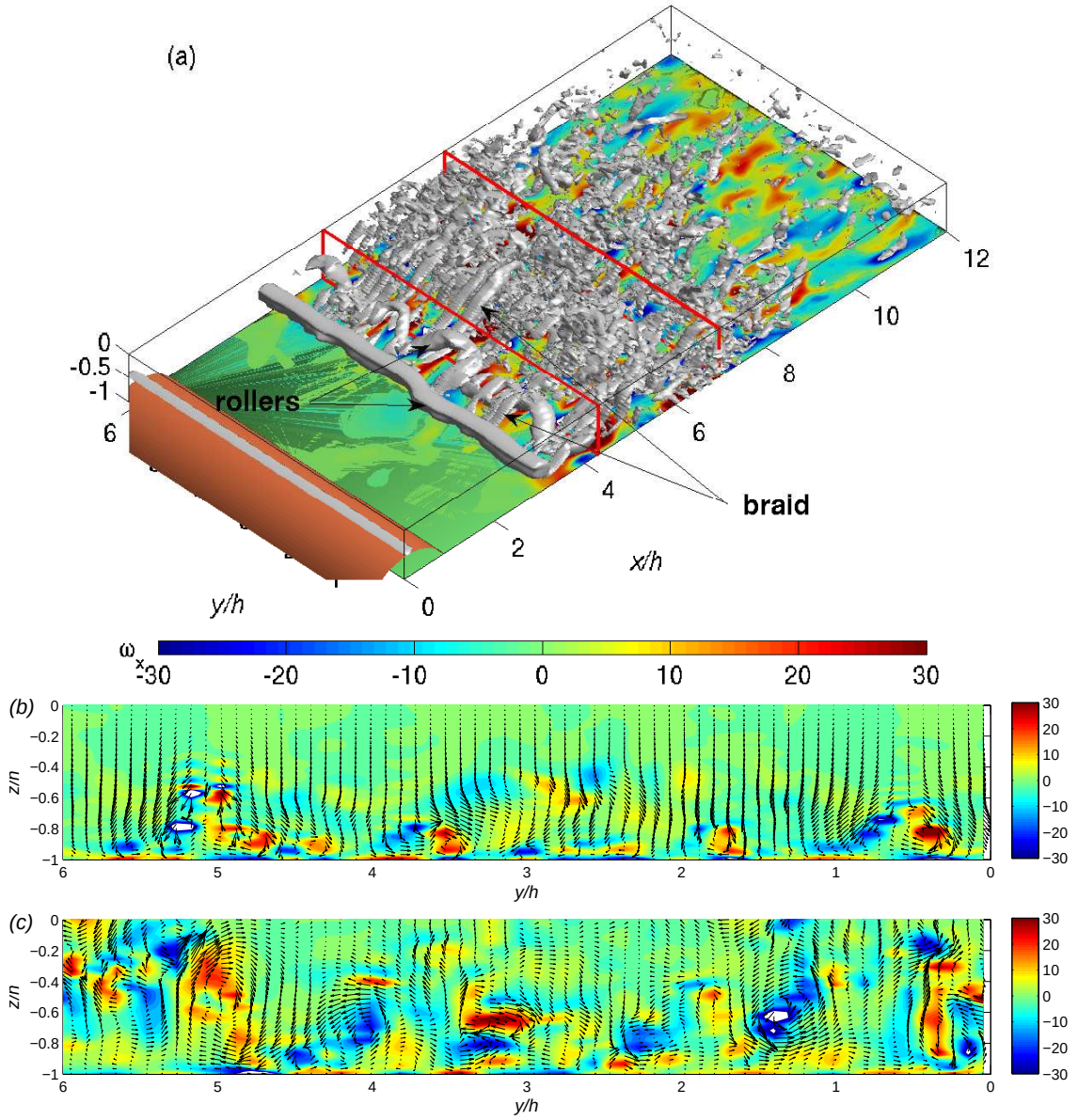

Figure 4.7: A snapshot of the dominant coherent structures in case 1 visualized by iso-surfaces of Q at $t/T = 0.58$. Only the bottom half of the channel is shown and iso-contours of streamwise vorticity, $\omega_x h/U_m$ are plotted on the wall. (b)-(c) Instantaneous distribution of $\omega_x h/U_m$ at the two y-z planes in the braid regions marked on part (a) of the figure.

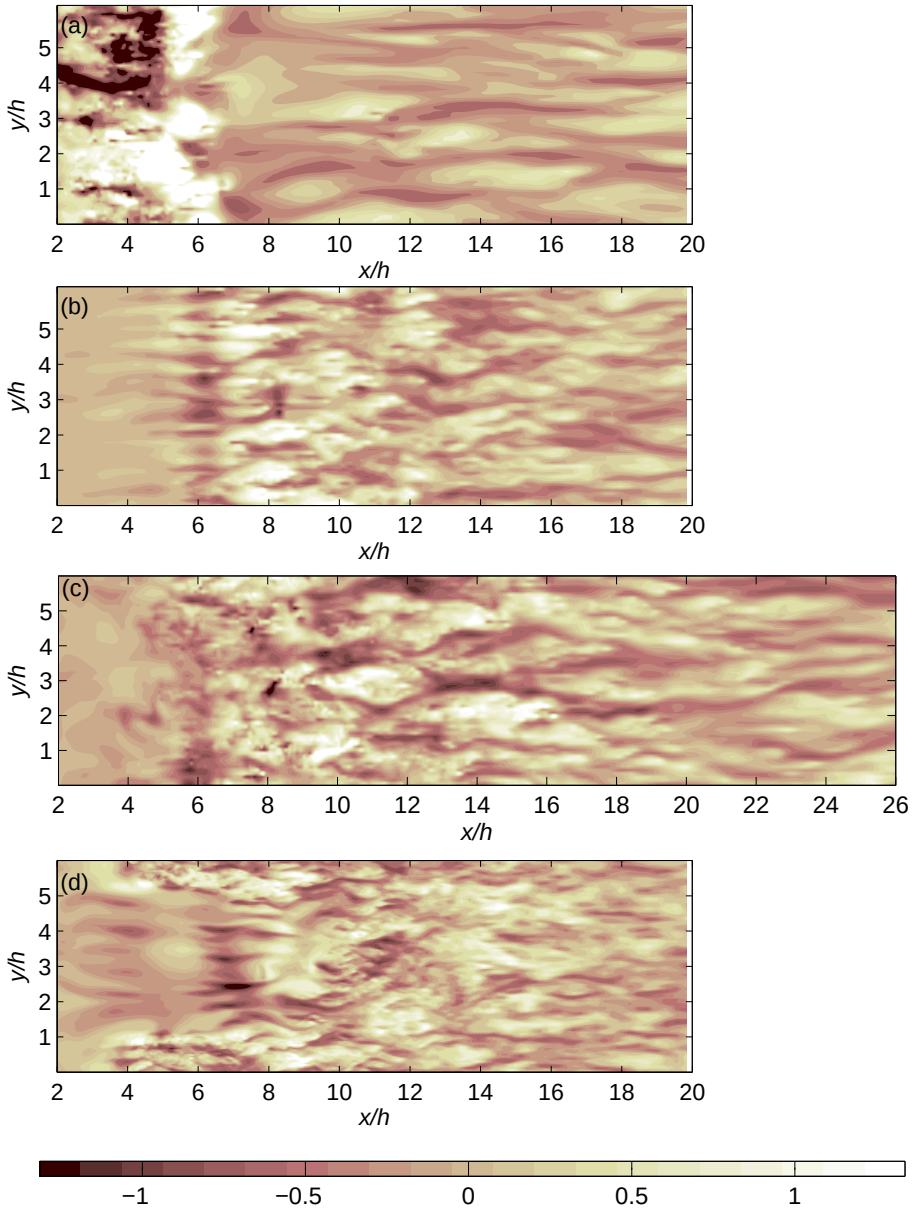

Figure 4.8: Iso-contours of the instantaneous velocity fluctuations, u''/U_m, at an x-y plane above the bottom wall ($z/h = 0.1$) at a characteristic instances after the maximum flow rate for each case(from top to bottom: case1; $t/T = 0.75$, case2; $t/T = 0.75$, case3; $t/T = 0.5$ and case4; $t/T = 0.75$).

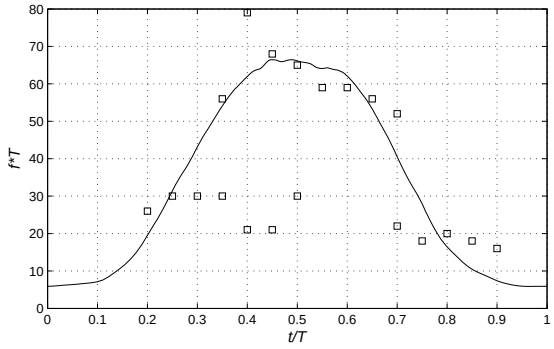

Figure 4.9: Vortex shedding frequencies vs phase in cycle for case 1: □ 'slotting' technique from the wall-normal velocity signal at $x/h = 2$ and $z/h = 0.5$; —— theoretical values based on thickness and velocity difference across the shear layer at $x/h = 0.5$.

frequencies due to vortex pairing. Observations of the instantaneous visualizations revealed that during this stage two or three vortices shed by the shear layer can merge by the time they reach $x/h = 2$. Outside this part of the cycle, the first band of lower frequencies from $t/T = 0.2$ to $t/T = 0.3$ corresponds to the vortex 'pinch-off' that takes places during the initial stage of the shear layer instability. Finally during the late part of the deceleration, after $t/T = 0.7$, the Strouhal number decreases rapidly to approximately 20 and deviates from the quasi-steady analysis. This is most probably due to the fact the oscillations in the velocity signal are due to leftover structures in the post-stenotic region as no vortex shedding however was observed in the instantaneous visualizations after $t/T = 0.75$.

The initiation of the shear layer roll-up and duration of the subsequent vortex shedding depends on the time-scale of the imposed oscillations. In particular, as the reduced velocity, U_{red}, increases, the vortex shedding begins earlier in the cycle and lasts for a greater part of the cycle (see figure 4.2). In all cases though, it is

evident that for approximately half or more of the pulsatile cycle, the confined jet constantly generates a series of quasi two-dimensional spanwise-coherent structures and streamwise rib vortices that through various instability mechanisms evolve into hairpin-like vortices propagating on the wall and are responsible for most of the momentum transport near the wall. The spatial evolution of these turbulent-like structures can be traced by examining the contours of the instantaneous velocity fluctuations, u'' at an $x-y$ plane near the wall. In figure 4.8, snapshots of u'' for all cases are shown at an $x-y$ plane located at $z/h = 0.1$ at a time just after the maximum flow rate. Intense velocity fluctuations appear near the reattachment line in each case, which can be correlated with the three-dimensional instabilities of the spanwise rollers. In all cases, short 'streaks' of negative and positive u'' fluctuations can be identified shortly after the reattachment point. These short 'streaks' of positive and negative u'' merge as they evolve downstream, forming structures that are reminiscent of the high and low-speed streaks seen in turbulent boundary layers. We have also looked at different instances during the cycle and qualitatively similar patterns are observed as long as vortex shedding takes place. However, the evolution of these structures in time is different as one changes U_{red} and is discussed later in the paper.

To better illuminate the effect of these structures on the momentum transport dynamics, the quadrant decomposition of $\widetilde{u''w''}$ (see [60]) across the channel is shown for case 1 in figure 4.10. Results are shown for a characteristic location at $x/h = 12$, although statistics at other downstream locations are qualitatively similar. Clearly near the wall the 2^{nd} $(u'' < 0, w'' > 0)$ and 4^{th} quadrant $(u'' > 0, w'' < 0)$ con-

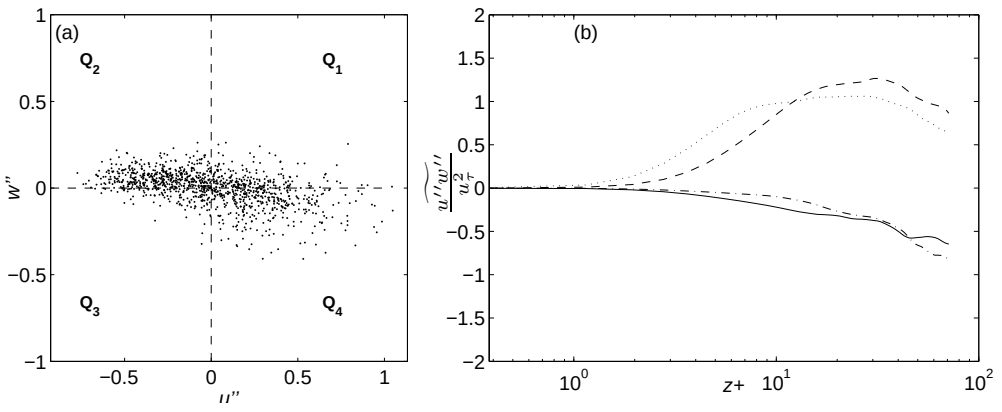

Figure 4.10: (a) Scatter plot of u''/U_m, w''/U_m events in case 1 at location $x/h = 17$ and $z/h = 0.1$; (b) The quadrant decomposition of the Reynolds shear stress, $\widetilde{u''w''}$, across the channel at the $x/h = 17$. —— Q_1: 1^{st} quadrant $(u'' > 0, w'' > 0)$; - - - Q_2: 2^{nd} quadrant $(u'' < 0, w'' > 0)$; —·— Q_3: 3^{rd} quadrant $(u'' < 0, w'' < 0)$; ····· Q_4: 4^{th} quadrant $(u'' > 0, w'' < 0)$. For both parts $t/T = 0.025$.

tributions are dominant, which is consistent with the presence of streaks. This is also reflected in the scatter plot of u'' and w'' events shown in figure 4.10a. As one moves away from the wall, more and more negative streamwise fluctuations are correlated with positive wall normal fluctuations. In a qualitative sense this behavior is very similar to the quadrant analysis of a turbulent channel flow, where sweep events dominate the viscous layer and ejections events gradually overwhelm them away from the wall. In the present case, however, the wall normal location where sweep events equal the ejections does not remain constant throughout the cycle, and appears to move closer to the wall as the flow decelerates. In addition, the exact contributions to the Reynolds shear stress vary with downstream distance as turbulent structures develop past the reattachment point.

4.2.2 Statistics and budgets

In the above section, we identified the vortical structures that dominate the dynamics of the flow in the shear layer and in the near wall region after the mean reattachment point. Next, we will examine the effect that these structures have on the phase averaged statistics and turbulence kinetic energy production, dissipation and transport in the channel. Figure 4.11 shows the phase-averaged turbulent kinetic energy, k, and the Reynolds shear stress, $\widetilde{u''w''}$, normalized by the 'local' bulk velocity, $\widetilde{U}_b$, in the pulsatile cycle and the half channel height. To illuminate the spatio-temporal behavior of these quantities, contours in the z/h versus t/T space are shown at three characteristic streamwise locations: one before ($x/h = 4$), and two after ($x/h = 12$ and $x/h = 20$) the mean reattachment point.

Very distinct patterns can be identified in the evolution of k and $\widetilde{u''w''}$ between the different streamwise stations. In particular, shortly before maximum flow rate there is a sudden burst in the levels of turbulent kinetic energy at $x/h = 4$. Most of it, however, is confined around the shear layers with relatively low levels near the walls, and negligible levels near the centerline. The levels of turbulent kinetic energy remain elevated for the first half of the deceleration, after which they gradually drop to very low levels and move towards the centerline as the jet becomes asymmetric. Finally, as the flow rate increases, turbulence activity in the channel remains negligible. At $x/h = 12$ (downstream of the mean reattachment location), the turbulent kinetic energy appears in a sudden burst prior to the peak flow rate, and is distributed uniformly across the channel, with high levels both near the wall

and the core. The levels gradually decay prior to the minimum flow rate, and no pronounced asymmetries can be identified at this location. Further downstream of the reattachment point at $x/h = 20$, peaks of the turbulent kinetic energy are only observed close to the walls, with a significant decay as one moves towards the centerline. The maximum levels of turbulent kinetic energy are sustained between $t/T = 0.0$ and $t/T = 0.1$, although the relative peaks near the wall still remain throughout most of the deceleration. As the flow rate increases, turbulent kinetic energy remains low, indicating that the flow during this part of the cycle tries to relaminarize throughout the channel.

Qualitatively similar patterns can be traced in the evolution of the turbulent Reynolds shear stress at the same downstream locations. Although $\widetilde{u''w''}$ is not the only component contributing to the production of turbulent kinetic energy, it is dominant in the regions of interest and gives a good indication of the regions where turbulence is 'active'. In particular, most of the turbulence production takes place around the shear layers at $x/h = 4$ from $t/T = 0.90$ to $t/T = 0.20$. As the flow reattaches, the levels of $\widetilde{u''w''}$ are more uniform across the channel, while further downstream at $x/h = 20$ peaks of $\widetilde{u''w''}$ are observed near the wall. This suggests that after the mean reattachment point the near wall region dynamics resemble those of turbulent boundary layers, while in the core turbulence is simply convected from upstream and is dissipated.

It is also important to point out the difference in the levels of turbulent kinetic energy and Reynolds shear stress as one moves from the shear layer dominated region ($x/h \sim 4$), to a station downstream of the mean reattachment point ($x/h \sim 12$),

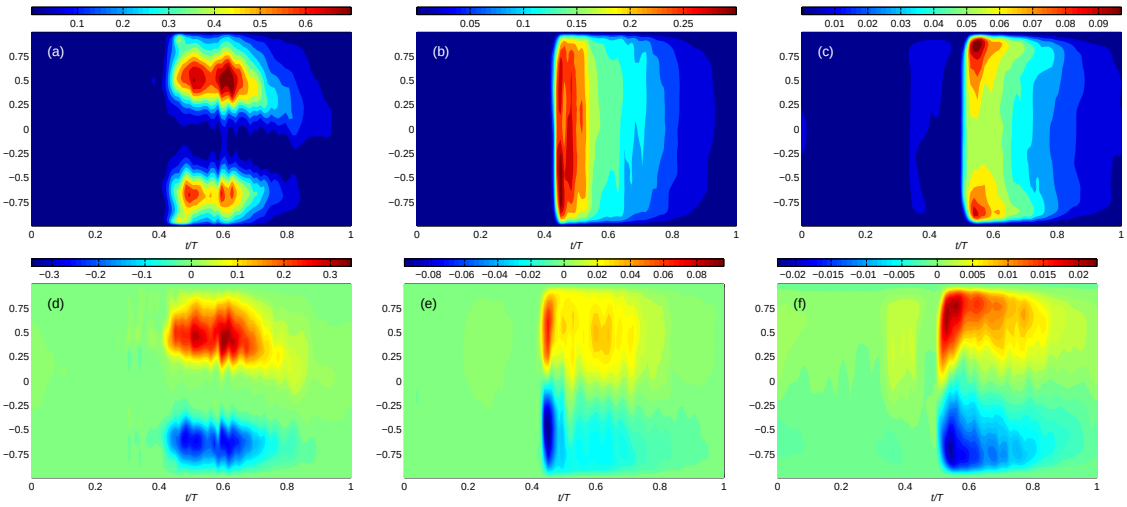

Figure 4.11: Contours of $\tilde{k}/U_m^2$ for a) $x/h = 4$, b) $x/h = 12h$, and c) $x/h = 20$, and $\widetilde{u''w''}/U_m^2$ for d) $x/h = 4$, e) $x/h = 12h$, and f) $x/h = 20$ for case 1 plotted in t/T versus z/h space.

where boundary layer like behavior is observed. Using a simple scaling arguments, the intensity of the turbulent activity present at the shear layers at the former station cannot be naturally sustained in magnitude in an equilibrium turbulent wall layer. Therefore in addition to the temporal decay of the turbulent kinetic energy and Reynolds shear stresses observed at each location due to the decreasing Reynolds number, there is a spatial decay of the above quantities as the nature of turbulence transitions from that of a shear layer to that of a wall layer.

To better understand how turbulent kinetic energy is produced, dissipated, and transported in the post-stenotic area, we looked into the budgets of the phase averaged turbulent kinetic energy governed by the following equation:

$$\frac{\partial \tilde{k}}{\partial t} = \underbrace{-\widetilde{u_i'' u_j''}\frac{\partial \widetilde{U_i}}{\partial x_j}}_{P_k} \underbrace{-\frac{1}{Re}\widetilde{\frac{\partial u_i''}{\partial x_j}\frac{\partial u_j''}{\partial x_i}}}_{\epsilon_k} + \underbrace{\widetilde{U_j}\frac{\partial \tilde{k}}{\partial x_j}}_{C_k} \underbrace{-\widetilde{\frac{p''u_j''}{\partial x_j}}}_{\Pi_k} + \underbrace{\frac{1}{Re}\nabla^2\tilde{k}}_{D_k} \underbrace{-\frac{\partial \widetilde{u''k}}{\partial x_j}}_{T_k} \tag{4.1}$$

where $k = 1/2 u_i'' u_i''$. The term on the left hand side is the phase-averaged rate of change ($\partial k/\partial t$) of the turbulent kinetic energy. On the right hand side, the first and

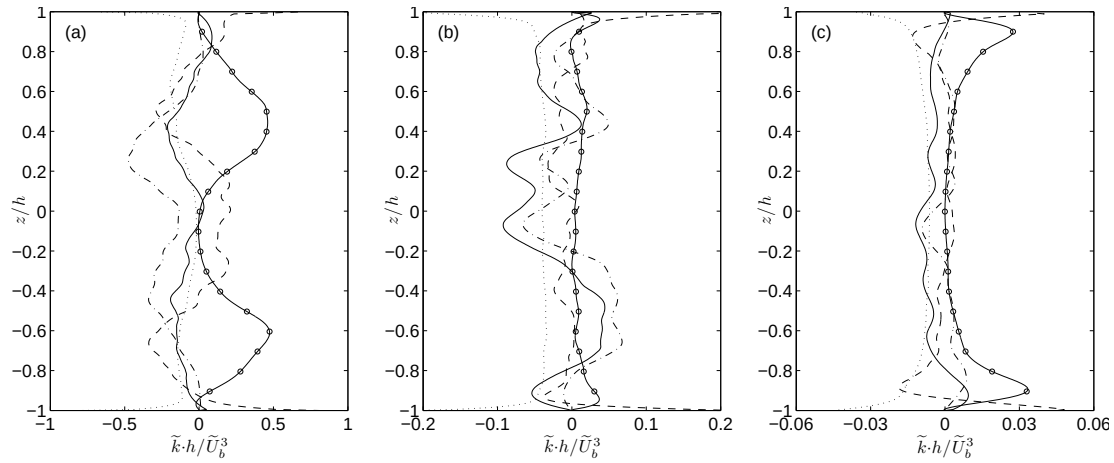

Figure 4.12: Budgets of the phase-averaged turbulent kinetic energy for case 1 at $t/T = 0.5$ for three downstream locations (a) $x/h = 4.8$, b) $x/h = 9.2$, and c) $x/h = 17.0$. The terms are shown as follows: $\circ$ P_k; ····· ϵ_k; – – – T_k; ——— C_k; —·— $\partial k/\partial t$

second terms are usually defined as the production (P_k) and dissipation (ϵ_k) of k, and are the only terms that add or remove energy. The last four terms on the right hand side represent transport of turbulent kinetic energy by the phase-averaged flow field (C_k), pressure velocity correlations (Π_k), diffusion (D_k), and turbulent transport (T_k) respectively. These terms can be written in conservative form and are responsible for redistributing k. Figure 4.12 shows the variation of these terms across the channel at two instances during the cycle and at three locations representative of the distinct flow features that exist downstream of the stenosis; one within the shear layer ($x/h = 4.8$), one shortly after the mean reattachment point ($x/h = 9.2$), and one in reattached wall layer ($x/h = 17.0$). For clarity Π_k, D_k and T_k have been lumped together as the total transport of turbulent kinetic energy.

Near the maximum flow rate at the station closest to the stenosis (see figure 4.12a), the turbulent kinetic energy is predominantly produced within the shear

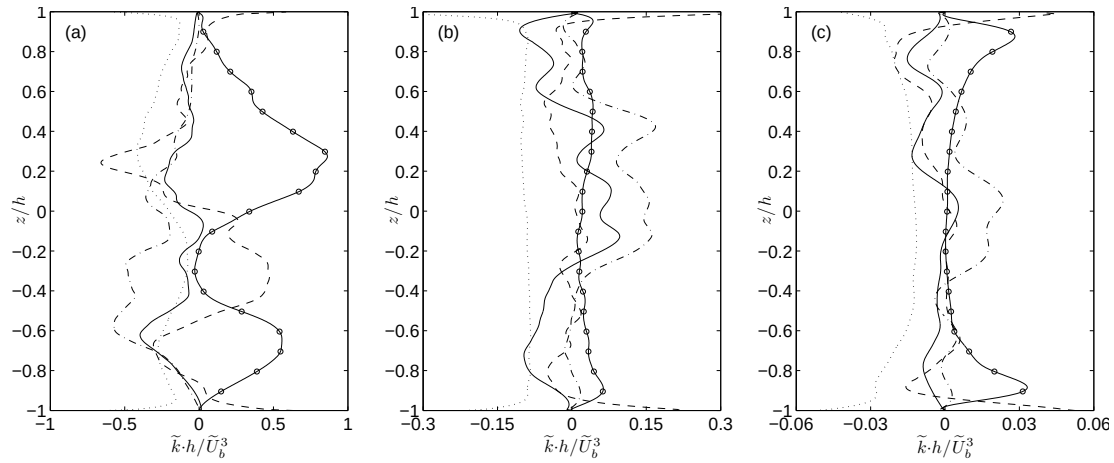

Figure 4.13: Budgets of the phase-averaged turbulent kinetic energy for case 1 at $t/T = 0.75$ for three downstream locations (a) $x/h = 4.8$, b) $x/h = 9.2$, and c) $x/h = 17.0$. The terms are shown as follows: $\circ$ P_k; ····· ϵ_k; – – – T_k; —— C_k; —·— $\partial k/\partial t$

layers as indicated by the shape P_k, which peaks at $z/h \pm 0.5$, and then goes to zero towards the center and the walls of the channel. Only a small part of the turbulent kinetic energy produced at the shear layers, however, is being dissipated: ϵ_k is just a fraction of the production term except for a small area very close to the wall. Instead, most of the produced energy is being transported away from the shear layers and towards the center of the channel (mainly by T_k) and the walls (mainly by D_k and Π_k) where it is balanced by ϵ_k. The remaining energy in the core of the channel is then convected by C_k.

After the flow reattaches, the energy balance changes dramatically. On one hand there is no production of turbulence away from the wall, as indicated by P_k in figure 4.12b, and the rate at which turbulent kinetic energy is transported across the channel is relatively small (as shown by T_k). The dominant terms for the most part of the channel are now the dissipation, e_k, and the convection, C_k, which at this location is predominantly in the streamwise direction. One the other hand, the

relative peaks in P_k and T_k near the walls, suggest that a 'turbulent-like' layer starts to develop. This is consistent with the presence the of streamwise oriented vortices discussed in the previous section, that transport momentum across the channel and sustain turbulent activity near the wall. As indicated by the balance of the different terms, this near wall flow is almost independent of the turbulent activity in the core, which consists of decaying, 'inactive', fluctuations.

Further downstream of the reattachment point, the turbulent kinetic energy budget shown in figure 4.12c resembles more that of a turbulent wall bounded flow. There is a clear peak in P_k near the wall while it decays quickly to negligible levels away from it. Transport and dissipation are also dominant near the wall, as found in a classical turbulent channel flow – although important differences exist between the two. First of all, the convection C_k and rate of change of turbulent kinetic energy $\partial k/\partial t$ are not zero in our case, due to the fact that the flow is still developing. Second, away from the wall the dissipation, ϵ_k, is orders of magnitude larger than production, P_k. Lastly, the similarity to classical equilibrium wall bounded flow was investigated by renormalizing the different terms in the budget equations using local the u_τ and ν (not shown here). Although the overall magnitude of the different terms, especially production and dissipation near the wall, is close to the ones found in low Reynolds number channel flow, the differences discussed above still remain. Given the superficial similarity of these regions to classical wall bounded turbulent layers, from now on we will refer to them as 'synthetic' turbulent boundary layers.

Throughout the deceleration phase, it was found that as long as energy is fed to the flow through the shear layer instability, the budgets of turbulent kinetic en-

ergy remain qualitatively similar (see figure 4.13). The main difference during the late deceleration stage is associated with the asymmetry of the jet, which causes the peaks of the P_k at the shear layers to shift accordingly as shown in figure 4.12a. This asymmetry, however, does not seem to significantly affect the energy balance downstream of the reattachment point as the turbulent kinetic energy contained in the wake of the jet is passive. In addition, the dimensional values of of the turbulent kinetic energy production, dissipation and transport throughout the channel decrease by an order of magnitude.

From the above analysis it is clear that the turbulent activity is driven by the dynamics of the shear layer, which is also consistent with the observations of the instantaneous dynamics of the flow. In particular, within the wall layer downstream of the reattachement point, the turbulent kinetic energy production is mostly sustained by the evolution/interaction of large vortical structures that originate from the shear layers. Even for the highest values of the Reynolds number we considered (case 5), as the shear layers weaken near the minimum flowrate ($t/T \sim 1.0$), vortex shedding stops and the near wall turbulence cannot be sustained. This is evident in figure 4.14, where the time evolution of the near wall maxima of the phase-averaged turbulent kinetic energy and its production at a location within the region of the 'synthetic' turbulent boundary layers (approximately $14h$ past the mean reattachment point), is shown. For the cases with the higher values of reduced velocity ($U_{red} \geq 26.5$), the transition to a turbulent-like regime downstream of the reattachment point appears in a burst, as indicated by a drastic spike in the levels of the turbulent kinetic energy and the finite values of the production term. Specifically,

the duration of the production events corresponds to the duration of active structure formation observed within the free shear layers. For example, in case 3, dominant production begins at $t/T = 0.5$ and decays to zero approximately at $t/T = 0.95$. This corresponds closely to the active structure formation duty cycle of the shear layer of approximately 0.45. For cases 4 and 5 the duty cycles are 0.68 and 0.60 respectively, which also compare favorably with the production durations shown in figure 4.14. The case with $U_{red} = 6.6$ (case 2), however, is the exception and does not fit the above pattern. Finite values of production of kinetic energy are found throughout the duration of the cycle, whereas the active duration of the shear layer duty cycle is only 0.35. This is most likely due to the fact that comparatively small mean convection velocity enables the relatively few active structures to remain in the near wall region for the majority of the cycle.

4.3 Axisymmetric configuration

Having discussed in detail the flow physics in the case of a symmetric stenosis in a planar geometry we look next in the flow characteristics downstream of an axisymmetric stenosis. We start by describing the instantaneous flow dynamics and transition mechanism for case 6. In this baseline case, the mean Reynolds number is 600 while the reduced velocity is 26.5, corresponding to the same parameters as those in case 1 in the planar geometry. The geometry of the stenosis was kept the same as the one in the Cartesian coordinates resulting in a percent occlusion of 75%.

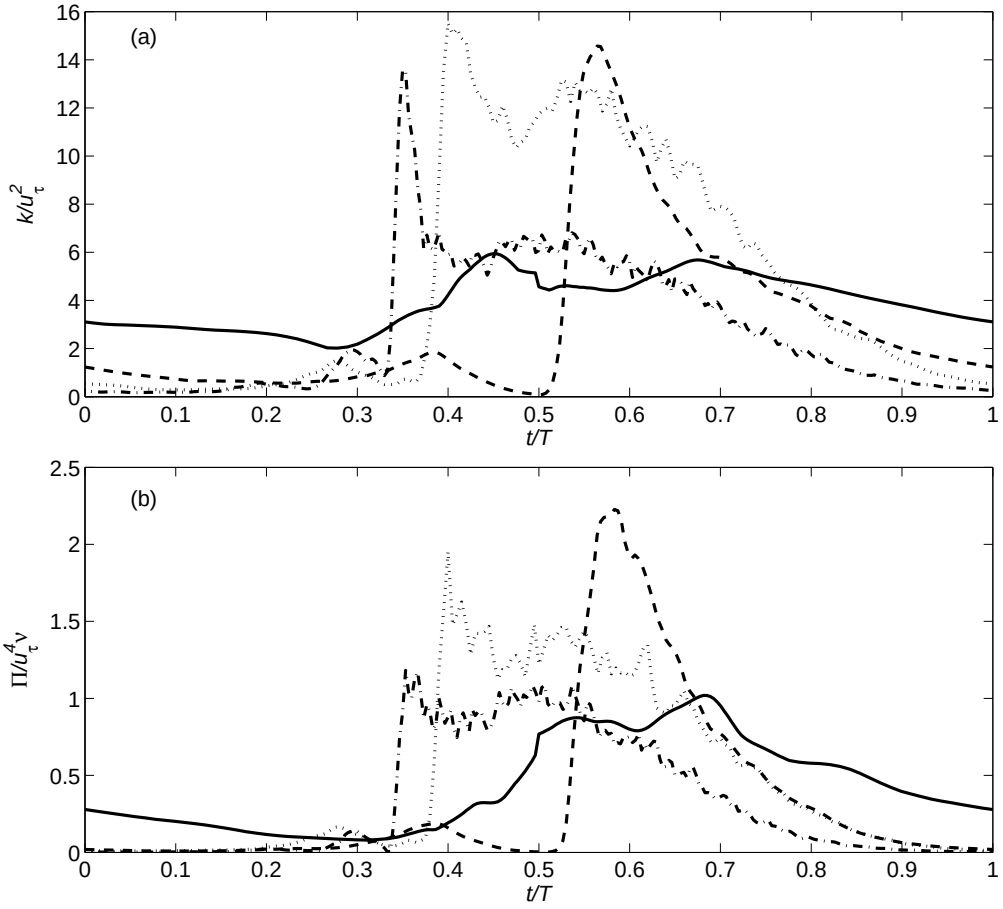

Figure 4.14: (a) near wall maxima of the phase-averaged turbulent kinetic energy and (b) turbulent kinetic energy production as a function of time at $x/h = 14$ downstream of the mean reattachment point, ——— ; case 2 ($Re = 600$, $U_{red} = 6.6$), – – – ; case 3 ($Re = 600$, $U_{red} = 26.5$), —·— ; case 4 ($Re = 600$, $U_{red} = 106.2$), ····· ; case 5 ($Re = 1200$, $U_{red} = 53.1$).

4.3.1 Instability of the start-up structure

Figure 4.15 shows as series of contours of the azimuthal vorticity on two selected azimuthal planes. On the same plot instantaneous streamlines are plotted to highlight the behavior of the recirculation bubble. During the early stages of the acceleration the flow remains axisymmetric downstream of the stenosis and thus these contours are representative of the flow patterns throughout the azimuthal direction. As the flow accelerates the shear layer that forms at the stenosis separates creating a small recirculation bubble. The vorticity that is imparted in the shear layer is mainly convected downstream along the edge of the recirculation, similar to the planar configuration. As the flow rate continues to increase the recirculation bubble becomes elongated at $t/T = 0.24$ and the reattachment points reaches at approximately $x/R = 10$. During this stage the shear layer fails to curl up as shown in figure 4.15e and continues to propagate along the edge of the recirculation bubble. Later in time though, the vorticity at the tip of the shear layer rolls-up into a vortex structure (labelled A) and detaches from the recirculation bubble. This vortex structure is considerably elongated as shown 4.15f due to the interaction with the walls. The recirculation bubble at $t/T = 0.31$ remains coherent and does not appear to collapse suggesting that shear layer remains stable. It is important to note that the shear layer extends all the way to $x/R = 15$ which is much farther downstream than the corresponding planar case. This is expected due to the fact that for the same stenosis the constriction is higher in cylindrical coordinates resulting in a larger jet velocities.

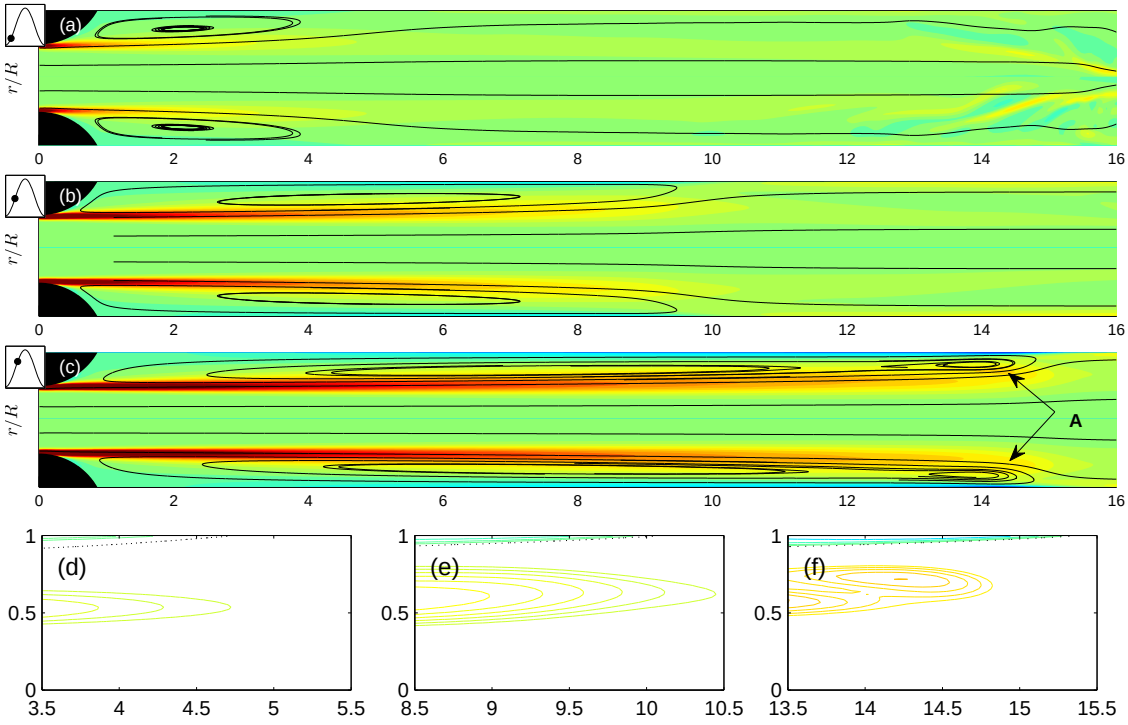

Figure 4.15: Filled iso-contours of spanwise vorticity and velocity streamlines for case 6 at three instances during the acceleration (a-c) and detailed iso-contour lines of spanwise vorticity following the downstream edge of the vortex ring (d-f). The dotted line in (d-f) represents the iso-contour of zero azimuthal vorticity. (from top to bottom (a,d); $t/T = 0.14$, (b,e); $t/T = 0.24$, (c,f); $t/T = 0.31$.

Crucial to the transition process is the instability and evolution of the leading vortex structure. Sherwin et al. [6] studied the instability modes and transition of pulsatile flow through a sinusoidally varying stenosis with the 75% occlusion. They performed a Floquet analysis to predict the most unstable mode of the leading vortex ring and performed a series of DNS to confirm the theoretical predictions. They considered Reynolds numbers between 200-300, and reduced velocities from 0.875 to 10. They found that for $U_{red} < 2$, modes greater than 1 (corresponding to a wavy-mode instability) dominate, while for $U_{red} > 2$ mode 1 (corresponding to a period-doubling instability) becomes dominant. To identify the instability mode in our case a plot of the auto-covariance of the radial velocity fluctuation (defined as $w"(\theta) \cdot w"(\theta + \delta\theta)/w"^2$ at $x/R = 14.0$ and at $r/R = 0.75$ corresponding to the center of the vortex ring is shown in figure 4.16c. It is obvious that mode 1 is the most unstable mode of the leading vortical structure in this case. This agrees well with the results of Sherwin despite the differences in the shape of the stenosis and the Reynolds number. Figure 4.16a shows contours of the azimuthal vorticity fluctuations in a $r-\theta$ plane at $r/R = 14$ and $t/T = 0.31$. The radial structure of the instability mode contains two nodes and extends from $r/R = 0$ to $r/R = 0.8$. The vortex structure at this stage lacks symmetry as evidenced both by the contours of the vorticity fluctuations and by a minimum value of the auto-variance function of about -0.8. To better understand the spatial features of the vortical structure A, figure 4.17 shows a selected iso-contour of the azimuthal vorticity at $t/T = 0.31$. The structure resulting from the shear layer roll-up appears to be considerably distorted as a result of the mode 1 instability and the interaction with the wall. The mode 1

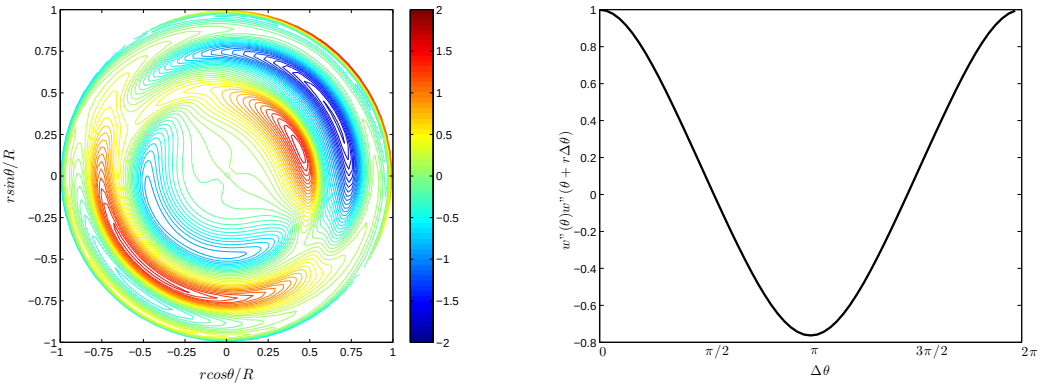

Figure 4.16: (a) Iso-contours of axial vorticity fluctuations for case 1 at $x/R = 14$, (b) Auto-variance of the radial velocity fluctuations at$x/R = 14$, $r/R = 0.75$. Both plots correspond to phase $t/T = 0.31$

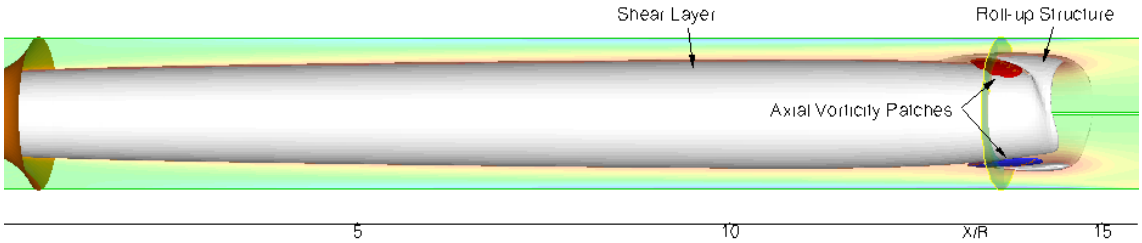

Figure 4.17: 3D representation of the shear layer and the roll-up at $t/T = 0.31$. Iso-contours of the azimuthal vorticity at ($\omega_\theta = 9.2$) are shown in white color, while isocontours of axial vorticity at $\omega_x = 3.5$ are shown in red and blue color.

instability is a single sinusoidal vortex line radially displaced from the toroidal axis of the shear layer. As a result the part of the shear layer that gets displaced radially outwards, as it rolls-up undergoes extensive stretching as it interacts with the wall, compared to the part of the shear layer that gets displaced inwards.

It is also interesting to note the presence of small patches of axial vorticity in the area between the roll-up structure and the shear layer itself. To understand how this streamwise vortical structures originate we take a look at the instantaneous vorticity dynamics at an $r - \theta$ plane at $x/R = 14$ that cuts through the shear layer,

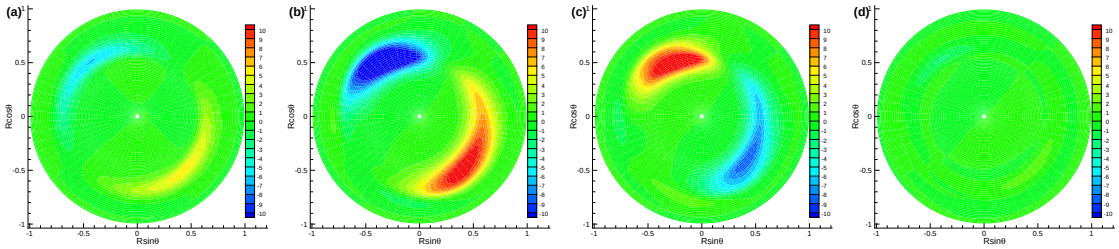

Figure 4.18: Iso-contours of (a) total rate of change of ω_x, stretching and reorientation of ω_z in (b) radial (c) azimuthal and (d) axial direction r/θ plane slicing at $x/R = 13.85$ at $t/T = 0.31$.

the roll-up structure and the axial vorticity patches. The axial component of the vorticity equation in cylindrical coordinates can be written as:

$$\frac{D\omega_x}{Dt} = \underbrace{\omega_r \frac{\partial U}{\partial r}}_{S_r} + \underbrace{\omega_\theta \frac{1}{r}\frac{\partial U}{\partial \theta}}_{S_\theta} + \underbrace{\omega_x \frac{\partial U}{\partial x}}_{S_x} + \underbrace{\frac{1}{Re}\nabla^2 \omega_x}_{D} \tag{4.2}$$

The rate of change of axial vorticity of a fluid particle $D\omega_x/Dt$, on the left hand-side of the equation, is determined by the stretching and reorientation of the radial, azimuthal and axial vorticity given by the first three terms on the right hand side (S_r, S_θ, S_x) and on viscous diffusion by the last term. Figure 4.18 shows iso-contours of $D\omega_x/Dt$ and the stretching terms S_r, S_θ and S_x. Viscous diffusion of the axial vorticity is negligible at this particular slice and thus is not plotted.

Since initially there is no axial component of vorticity, in areas where $D\omega_x/Dt > 0$ a patch of positive ω_x is being created, and in areas where $D\omega_x/Dt < 0$ and a patch of negative ω_x is being created. It is seen from figure 4.18a that a pair of counter rotating patches of axial vorticity 180° apart is concentrated in a thin arc-shaped region around $r/R = 0.6$. Everywhere else $D\omega_x/Dt$ is negligible. This means that axially oriented vortical structures are being formed in a region corresponding between the shear layer ($r/R = 0.5$) and the roll-up structure ($r/R = 0.75$). The

other terms shown in figure 4.18b-d reveal that these structures are being mainly created through the reorientation and stretching of ω_r and ω_θ, by shearing motions caused by azimuthal and axial gradients of streamwise velocity U, with the first mechanism being more dominant than the second. The above analysis points to the fact the the generation of the streamwise vortices does not originate directly from the reorientation of the azimuthal vorticity in the leading roll-up vortex structure. The latter is a highly distorted structure that has been stretched by the velocity gradients in the near wall regions and does not undergo the classical three dimensional instabilities experienced by isolated slender vortex rings. Instead it is the interaction of the roll-up structure with the shear layer that gives birth to axially oriented streamwise structures confined in the region between the two.

As these axially oriented structures evolve in time they form into a structure that resembles the instantaneous horseshoe vortices observed in experiments and computations [20, 17]. Figure 4.19a-d shows a time-series of iso-surfaces of the Q-criterion colored by axial vorticity. Contours of the azimuthal vorticity on two $r-z$ planes 180° apart are shown in the background for clarity. To better visualize the vortical structure a side and top view is shown below each figure, accompanied by velocity vectors plotted on a $r-\theta$ plane slicing through the vortex. At $t/T = 0.35$ the positive and negative patches of axially vorticity shown in figure 4.17 subjected to the local shear become the streamwise oriented legs of the hairpin like vortical structure. The legs are located in the region between the shear layer and the roll-up structure. The latter is still visible in the contours of azimuthal vorticity but it appears to be considerably elongated. The legs have a Λ shape and are tilted

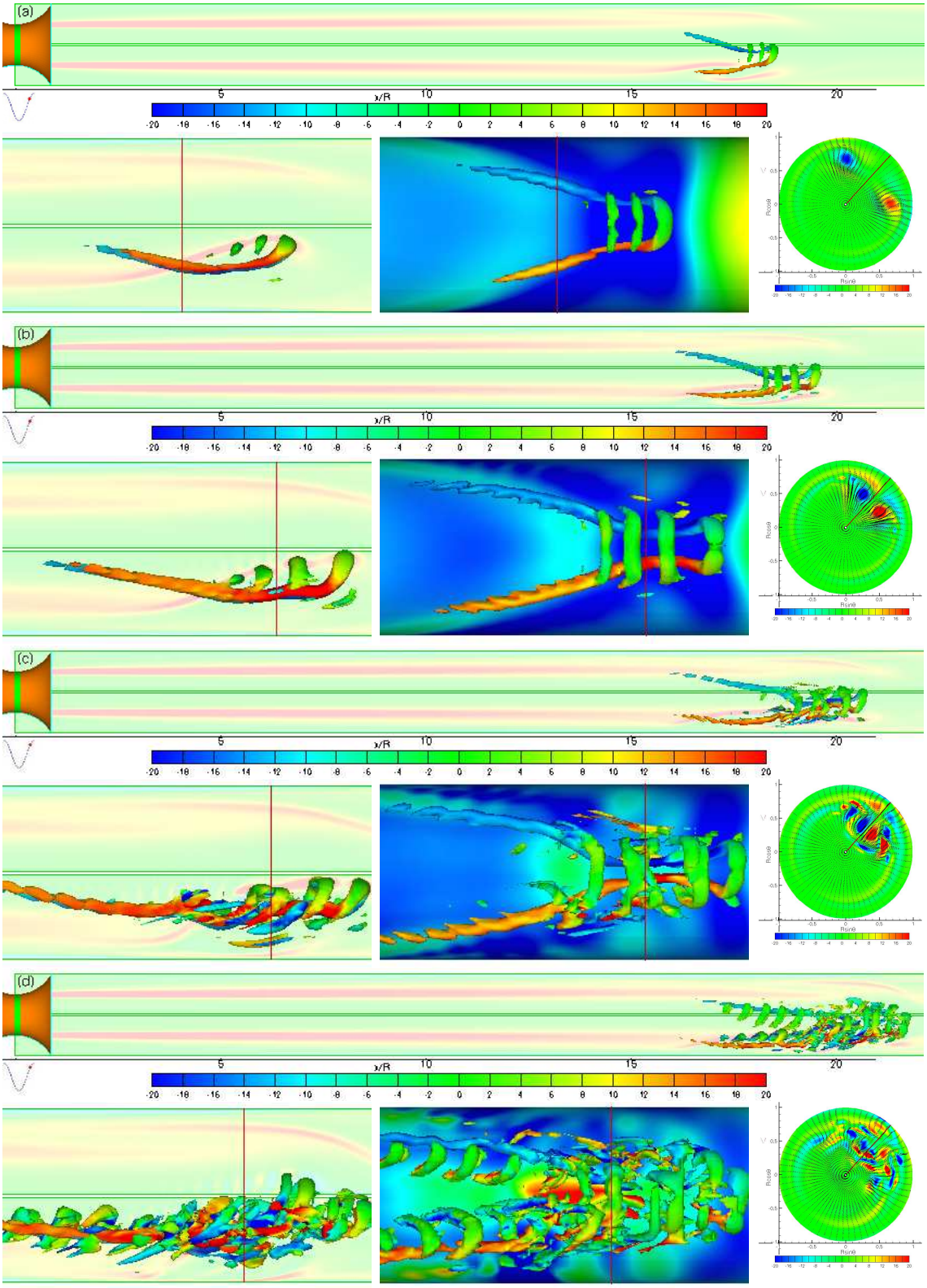

Figure 4.19: Iso-contours of the Q criterion colored by axial vorticity. On the background are plotted contours of azimuthal vorticity at selected r-z planes. From top to bottom the phase in the cycles are (a) $t/T = 0.35$, (b) $t/T = 0.36$, (c) $t/T = 0.37$ and (d) $t/T = 0.38$

slightly upwards and are connected to the tip of the shear layer at the downstream end forming the head of the hairpin like structure.

The evolution of this horseshoe like vortex shares a lot of common features with the evolution of a hairpin vortex introduced in a turbulent channel studied by Adrian et al. [64]. At $t/T = 0.36$ the hairpin like structure consists of three sections: the legs of the vortex, which extend the longest in the axial direction; a shorter section in the middle consisting of a kink and narrowing of the legs; and the Ω shaped head at the front. The bridges around the middle section are break-ups of the shear layer and only the upstream one reconnects the two legs at the kink. The main difference of this naturally formed horseshoe vortex with the one studied by Adrian is its orientation, with the latter having the upstream part of legs positive inclined upwards from the wall. In addition, as it can been see by the contours of azimuthal vorticity plotted on the wall the hairpin vortex has not yet entered the reattached wall region.

As the vortex further evolves in time, it gets stretched by the local shear and extends even more in the axial direction. At $t/T = 0.37$ a secondary hairpin vortex is formed by viscous reconnection of the legs of the primary hairpin near the kink. In addition other streamwise oriented vortices begin to form below and on the side of the legs of the primary hairpin as clearly shown by the contours of axial vorticity plotted on the cross sectional view. At $t/T = 0.38$ the initial hairpin vortex has evolved into a complex packet of vortices. A series of cane-like vortical structures of opposite axial vorticity are seen on each leg. The front of the packet consists of many smaller streamwise oriented vortices occupying about half of the cross-section

of the pipe. It is obvious from the above discussion that the evolution of the initial hairpin resulted in a patch of vortical structures with turbulent like characteristics and self-sustained dynamics.

Next we examined the effects of the reduced velocity on the dynamics of the leading roll-up structure. Figure 4.20 shows contours of azimuthal vorticity for case 7 and 8 at selected phases in the cycle during the initial stages of the roll-up process. The effect of the stroke length on the localization of the shear layer tip is obvious. For the case with the smallest stroke length the shear layer extends to about $x/R = 1$ at $t/T = 0.35$ while for the case with the largest stroke length the shear layer extends up to $x/R = 19$ at $t/T = 0.25$. This is in qualitative agreement with the corresponding cases in the planar configuration. In addition, for the case of the smallest reduced velocity there is considerable noise ahead of the shear layer as a result of vortical structures from the previous cycles that have not been completely dissipated. At $t/T = 0.35$ the strongest structures are located in a region between $x/R = 6$ and $x/R = 12$ although weaker disturbances are present all the way upstream to the shear layer. The auto-covariance of the radial velocity fluctuation at the tip of the shear layer is shown for both cases in figure 4.21. The axial location corresponds to the vertical line in figure 4.20 while the radial location is at $r/R = 0.55$ and $r/R = 0.50$ for the cases 7 and 8 respectively. For the case of the smallest reduced velocity the auto-variances shows that the most dominant mode of instability is mode 2, although a third peak at $\Delta\theta = \pi$ suggests that a third mode is also emerging. It is possible that the disturbances that are present near the stenosis gives rise to other modes besides mode 2. For the case of the

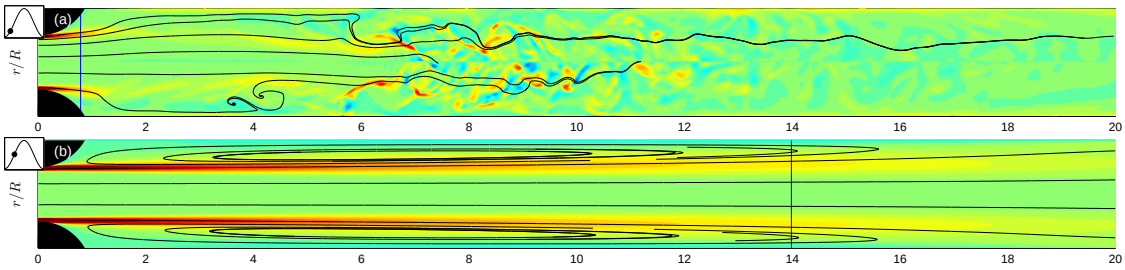

Figure 4.20: Filled iso-contours of spanwise vorticity and velocity streamlines for (a) cases 1 at $t/T = 0.15$ and (b) case 3 at $t/T = 0.25$.

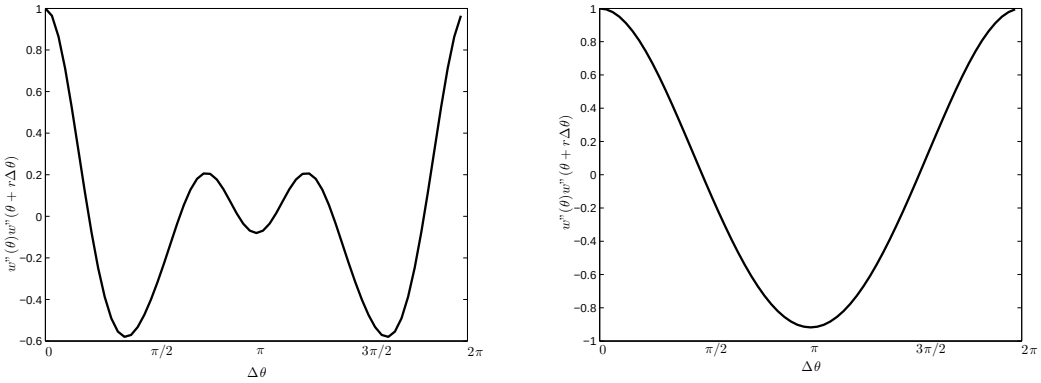

Figure 4.21: Auto-variance of the radial velocity fluctuations at early stages of the shear layer roll-up (a) case 1: $t/T = 0.35$ and $x/R = 0.80$, $r/R = 0.55$; (b) case 3: $t/T = 0.35$ and $x/R = 0.25$, $r/R = 0.50$.

highest reduced velocity the most unstable mode is mode 1 confirming the trend observed by Sherwin et al. [6] that mode 1 dominates as the reduced velocity gets larger. Of course the Floquet analysis performed by Sherwin et al. [6] where mode 1 dominates for reduced velocity greater than 2 was for cases with Reynolds of 300 and lower. In their cases all vortical structures had been completely dissipated within one cycle and during the acceleration phase the flow downstream of the shear layer had negligible levels of disturbances.

The structures resulting from the roll-up of the shear layer are visualized in 4.22 through iso-surfaces of the Q criterion. For the case of the smallest reduced

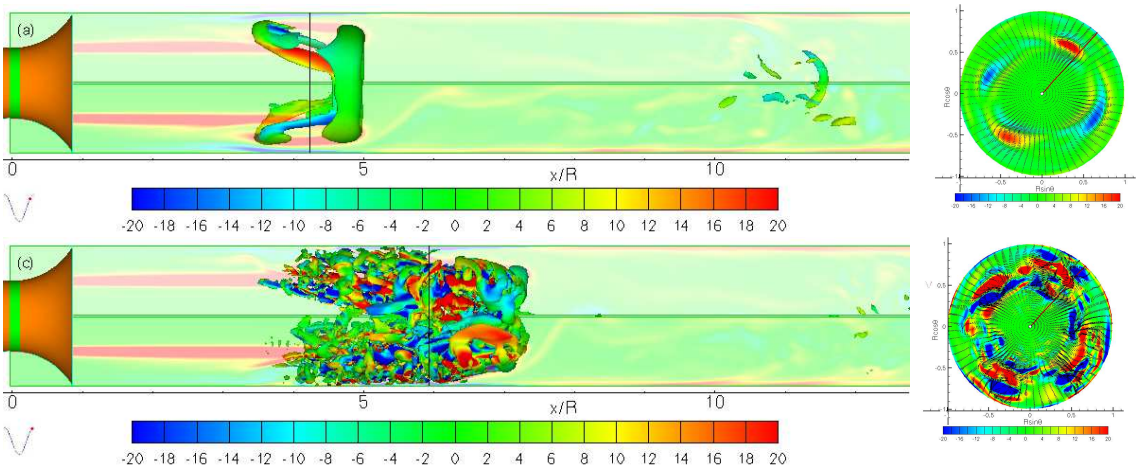

Figure 4.22: Iso-contours of the Q criterion colored by axial vorticity. On the background are plotted contours of azimuthal vorticity at selected r-z planes. On the right of each figure are plotted the velocity vectors superimposed on contours of axial vorticity on a selected $r-\theta$ plane at a x/R location indicated by the black line. From top to bottom the phase in the cycles are $t/T = 0.37$ and $t/T = 0.95$ respectively.

velocity with mode 2 instability, the interaction between the roll-up structure and the shear layer results in the generation of two pairs of streamwise oriented vortical structures. The core of these vortices is located between the shear layer and the roll-up and consists of legs with alternating positive and negative axial vorticity as shown in the cross-sectional view in figure 4.22b. Near the wall the legs are connected to the roll-up structure and away from the wall they are connected to the the shear layer. These structures generate other vortices and quickly evolve into a complex packet of axial vortices as shown in figure 4.22c. A cut through the patch shown in figure 4.22d reveal the presence of many streamwise vortices that occupy the entire cross-section of the pipe.

For the case with the highest reduced velocity where the most unstable mode during the roll-up process is mode 1 a horseshoe-like vortex emerges from the inter-

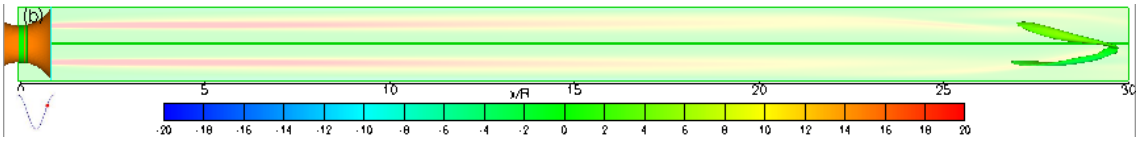

Figure 4.23: Iso-contours of the Q criterion colored by axial vorticity at $t/T = 0.25$. On the background are plotted contours of azimuthal vorticity at selected r-z planes.

action of the shear layer and the roll-up structure as shown in figure 4.23. The shear layer extends considerably further downstream to $x/R = 25$ owing to the increased stroke length at this reduced velocity. The formation dynamics of the roll-up process are very similar to the ones observed in case 4. This suggests that the formation of a hairpin vortex as a result of mode 1 instability of the shear layer during the roll-up process is a robust phenomenon.

4.3.2 Initial stages of the non-linear instability

Following the formation of turbulent-like vortices from the interaction between the shear layer and the roll-up structure, the shear layer becomes unstable and starts shedding a series of vortex rings. The instability is observed even in the absence of noise at the inlet suggesting that perhaps the leading patch of turbulent structures must play a role in the initiation of the shear layer instability. A representative picture of the vortical structures during the early part the shear layer instability is shown in figure 4.24. The front of streamwise vortices resulting from the instability of the roll-up structure is seen around $x/R = 20$. Following that patch 6 vortex rings can be clearly identified within the shear layer extending from approximately $x/R = 7.0$ to $x/R = 13$. The contours of azimuthal vorticity plotted on the background resemble those of Kelvin-Helmholtz type instability. The vortex rings appear to

undergo three dimensional instabilities as the propagate downstream but remain very coherent at this stage. A plot of the radial vorticity at a $r-\theta$ plane cutting through the second vortex ring at $x/R = 8.0$ shown in figure 4.24b reveals the presence of multiple instability modes confined within the region $r/R = 0.4$ and $r/R = 0.6$. The auto-covariance and power spectra of the radial vorticity fluctuation shown in figures 4.24c and 4.24d respectively at $r/R = 0.5$ reveal that most of the energy is located in mode 3 while modes 1 and 2 have some energy contents as well.

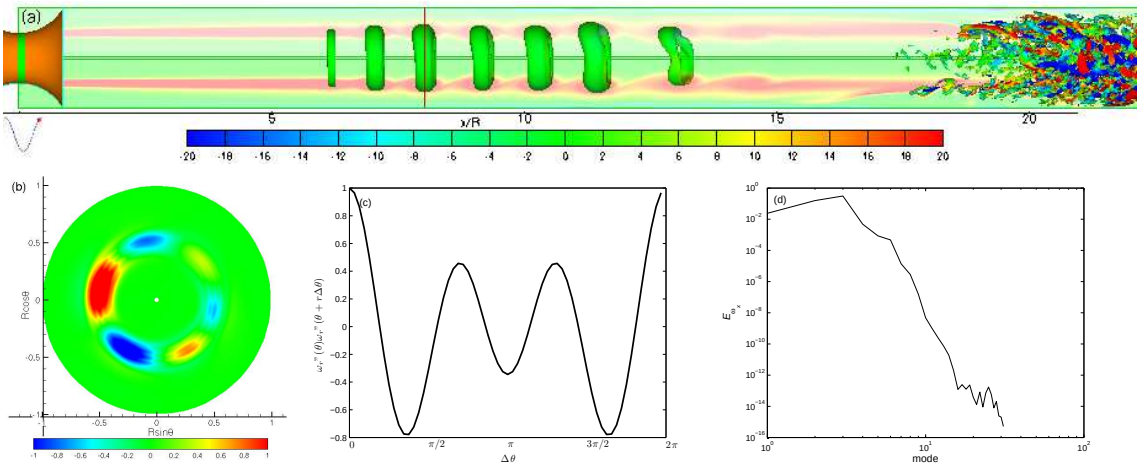

Figure 4.24: A representative picture of the shear layer instability at $t/T = 0.92$. (a) Iso-contours of the Q criterion colored by axial vorticity and contours of azimuthal vorticity at selected r-z planes on the background. (b) Contours of radial vorticity at $r-\theta$ plane at $x/R = 8$ cutting through the second vortex ring. (c) Auto-covariance of the radial vorticity fluctuations at $x/R = 8.0$ and $r/R = 0.5$. (d) Power spectra of the axial vorticity fluctuations at $x/R = 8.0$ and $r/R = 0.5$.

The way that these vortex rings transform into turbulent-like vortices is qualitative different from the mechanism observed earlier during the shear layer roll-up process. Figure 4.25 shows a series of iso-surfaces of the Q criterion contoured by the axial vorticity a little later in the cycle. First of all the vortex rings appear to be more slender and less elongated than the initial roll-up structure. As $t/T = 0.93$

they remain coherent by appear to undergo extensive deformation corresponding to their instability mode. During this transformation the parts of the vortex ring that are displaced radially outwards as a result of the instability are closer to the wall and travel at a slower speed than parts of the vortex ring that are displaced inwards and propagate faster. Consequently, in the region between them the vortex rings get reoriented in the streamwise direction and stretched producing axial vorticity. During the transformation process the vortex rings quickly generate other streamwise oriented vortices. This can be clearly seen in figure 4.25b where at $t/T = 0.94$ the leading vortex ring has evolved into two vortex legs with positive and negative axially vorticity extending from about $x/R = 16$ to $x/R = 18$. Other streamwise oriented vortices can be seen around and upstream of the legs. The trailing vortex rings from $x/R = 10$ to $x/R = 15$ undergo similar transition process too.

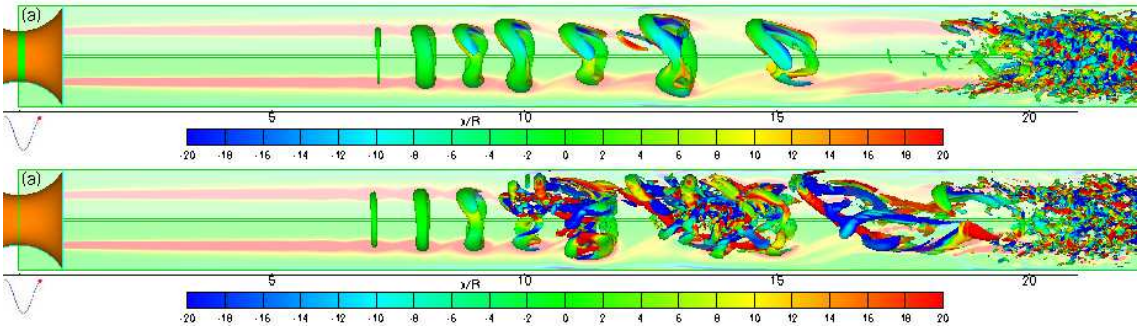

Figure 4.25: Selected iso-contour of the Q criterion colored by axial vorticity and contours of azimuthal vorticity at selected r-z planes on the background at (a) $t/T = 0.93$ and (b) $t/T = 0.94$

Another feature of this shear layer instability is that the most dominant mode observed at the leading vortex rings can change from cycle to cycle. Figure 4.26 shows a series of iso-surfaces of the Q criterion contoured by the axial vorticity corresponding to approximately the same phases as those in figure 4.25 but taken

from one cycle earlier. The vortex rings undergo a transformation consistent with a mode 2 instability. At $t/T = 0.94$ the leading vortex ring located around $x/R = 12.5$ begins to fold into two creating two pairs of vortex legs with positive and negative axial vorticity. The trailing vortex rings located around $x/R = 10$ undergo the same deformation. As expected at $t/T = 0.95$ the legs of the leading vortex ring become more elongated in the direction of the flow as shown in figure 4.26b and generate other vortical structures. While this process takes places there seems to be interaction and merging between successive vortex rings. It is interesting to note that even though the instability mode of the vortex rings shed by the shear layer may change from cycle to cycle, the mechanism by which these rings transform their azimuthal vorticity into streamwise vortical structures remains unchanged.

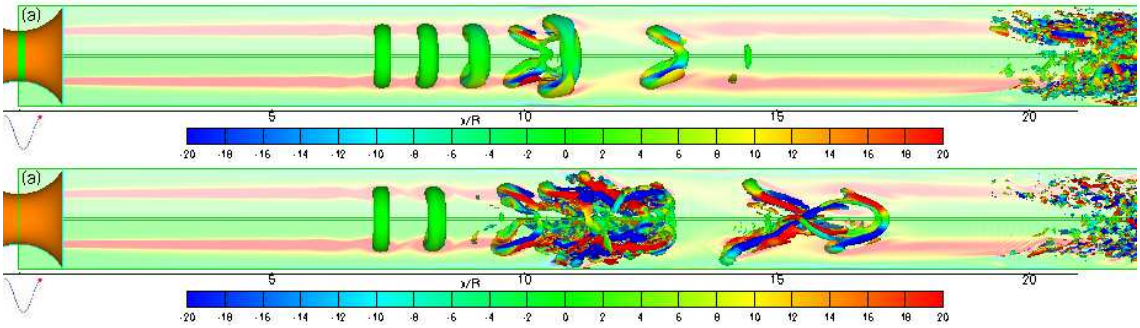

Figure 4.26: Selected iso-contour of the Q criterion colored by axial vorticity and contours of azimuthal vorticity at selected r-z planes on the background at (a) $t/T = 0.94$ and (b) $t/T = 0.95$

The shear layer continues to shed vortices throughout the deceleration phase. During this period the noise environment created by the breakdown of the vortex rings has propagated upstream and reaches closer to the stenosis. Figure 4.27 shows the trace of the turbulent kinetic energy as function of time. Initially there high levels of turbulent kinetic energy located between $x/R = 17$ and $x/R = 24$ cor-

responding to the turbulent patch of vortical structures generated by the roll-up process. Upstream and downstream of that patch the levels are very low indicating the flow must have relaminarized. Within a short duration of $\Delta t/T = 0.1$ the turbulent kinetic quickly propagates upstream and peaks around $x/R = 10$ where it remains for most of the deceleration.

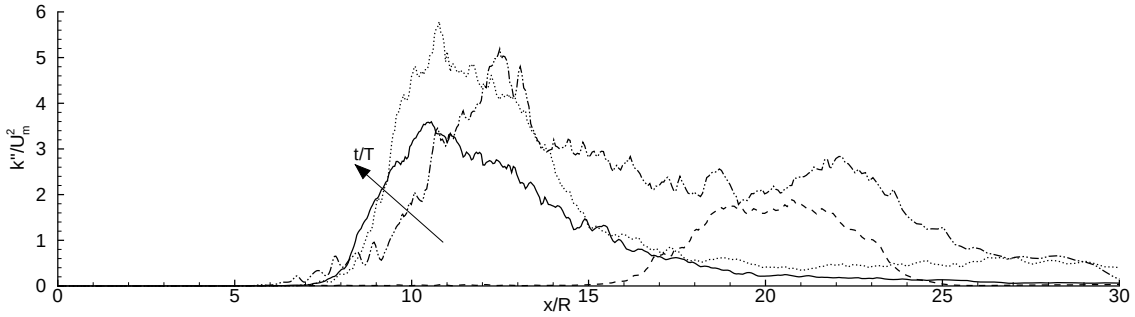

Figure 4.27: Phase-averaged turbulent kinetic energy (case 6). Streamwise variation at r/R=0.5 at four phases in the pulsatile cycle: - - - $t/T = 0.40$; —·— $t/T = 0.45$; ····· $t/T = 0.50$; ——— $t/T = 0.70$

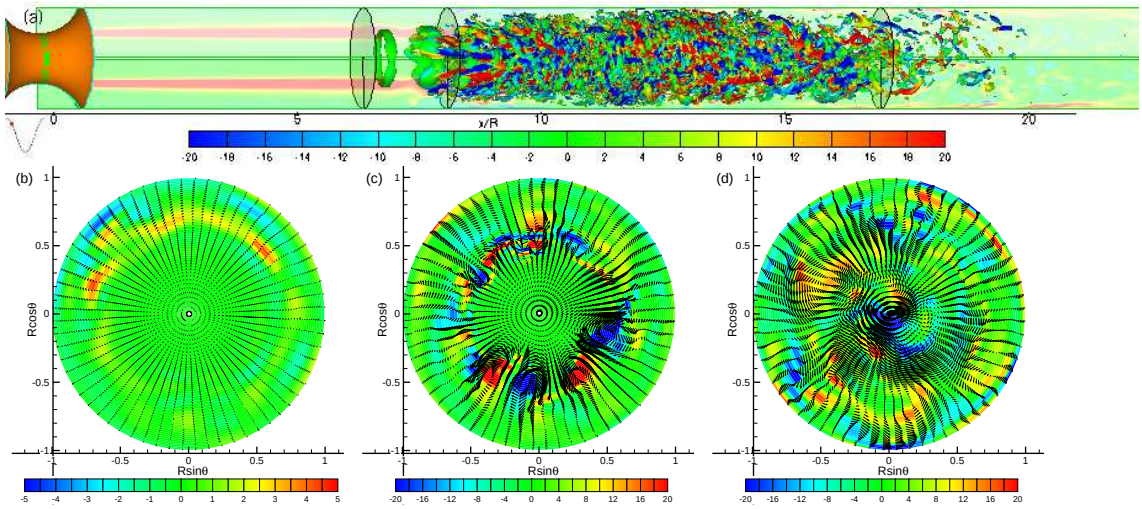

Figure 4.28: Selected iso-contour of the Q criterion colored by axial vorticity and contours of azimuthal vorticity at selected r-z planes on the background at $t/T = 0.13$

A representative picture of the flow dynamics during the deceleration is shown in figure 4.28a. A coherent vortex ring can be clearly seen around $x/R = 7$ and

just downstream another vortex ring undergoes a three-dimensionally instability. Just ahead of the latter there is a "braid" region where several counter rotating rib vortices exist. The strength of these vortices is better illustrated in figure 4.28c where iso-contours of the axial vorticity are plotted at a $r - \theta$ plane in the "braid" region. It is important to note that vortical structures resulting from earlier break-up of the vortex rings have propagated all the way upstream near $x/R = 6$ making the instability of the vortex rings at this stage non-linear. The is shown in figure4.28b where patches of axial vorticity are observed in the region between the shear layer and the wall. Further downstream the evolution of the vortex rings and the rib vortices results in the formation of patch of streamwise structures that fill the entire cross-section of the pipe as shown in figure 4.28c.

The effect of the reduced velocity on the initial roll-up and shear layer instability is qualitatively similar to that in the Cartesian cases. On one hand as the reduced velocity is increased, the amount of circulation imparted in the shear layers increases too. On the other hand the largest the reduced velocity the more time the diffusion has to act. The first phenomena tends to accelerate the roll-up process while the second one inhibits it. As a result, for case 8, which has the largest reduced velocity, the roll-up structure and subsequent shear layer instability does happens earlier in the cycle, but only by $\Delta t/T = 0.04$ compared to case 6. On the other hand, for case 7, which has the smallest reduced velocity, instantaneous visualizations reveal that the roll-up process occurs later during the acceleration and that shear layer does not roll-up into a series of vortex rings during the deceleration. Finally for case 9, where the Reynolds number is doubled compared to case 6, the

initial roll-up structure stage is bypassed and the shear layer becomes unstable more quickly.

4.3.3 Phase averaged statistics

Having identified the coherent vortical structures in the post-stenotic region and the mechanisms by which these structures transform the azimuthal vorticity in the shear layer into streamwise structures with turbulent-like features we next try to quantify the effect of these structures on the phase-averaged turbulent statistics. Figure 4.29 shows the phase-averaged turbulent-kinetic energy k, and the Reynolds shear stress $\widetilde{u''w''}$ normalized by the mean bulk velocity. To illuminate the spatio-temporal behaviour of these quantities, contours in r/h versus t/T space are shown in three locations: one in the shear layer ($x/h = 10$), one shortly after the mean reattachment point ($x/h = 20$) and one further downstream in the reattached wall region ($x/h = 32$).

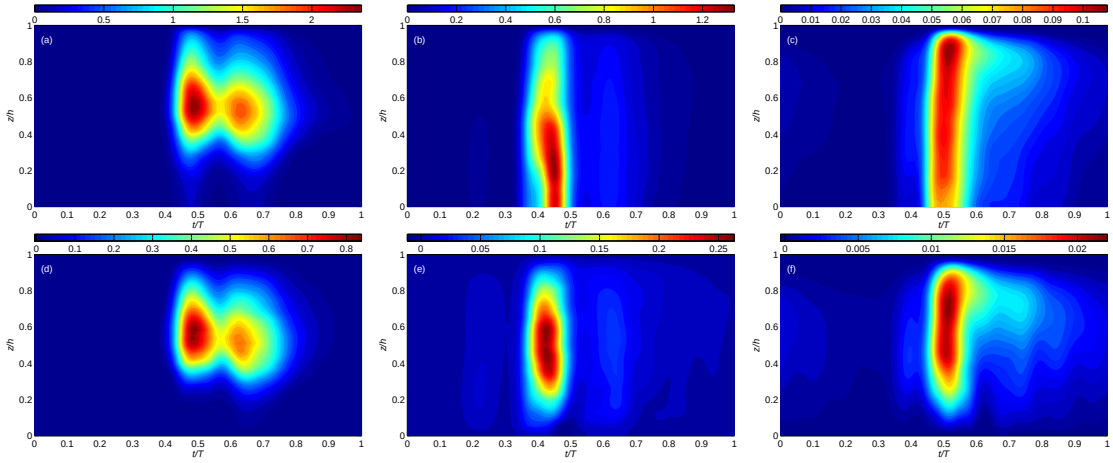

Figure 4.29: Contours of $\tilde{k}/U_m^2$ for a) $x/h = 10$, b) $x/h = 20h$, and c) $x/h = 32$, and $\widetilde{u''w''}/U_m^2$ for d) $x/h = 10$, e) $x/h = 20h$, and f) $x/h = 32$ for case 6 plotted in t/T versus z/h space.

At $x/h = 10$ the turbulent kinetic energy appears in a burst around $t/T = 0.4$. The peak of the turbulence is centered around $r/R = 0.55$ corresponding to the location of the shear layer. Near the wall there are considerable levels of turbulent kinetic energy while towards the centerline the levels decay very quickly. The turbulent activity is sustained in the shear layer midway through the deceleration and then very quickly decays suggesting that the shear layer stops shedding vortices after $t/T = 0.8$. The last patch of vortical structures that remain at this stage decay as they are convected downstream. The spatio-temporal evolution patterns of turbulent Reynolds shear stress resemble very closely those of the turbulent kinetic energy at $x/h = 10$ suggesting that the latter is directly related to the generation of turbulence resulting from the three-dimensional instabilities of the vortex rings.

Distinct patterns of turbulent activity can be observed downstream of the mean reattachment point. The turbulent kinetic energy fills the entire cross section of the pipe at $x/h = 20$. At this downstream location turbulence appears in a burst a little earlier at $t/T = 0.35$. This is due to the passage of patch of turbulent structures originating from the roll-up process. The turbulent kinetic energy maintains the highest levels until $t/T = 0.5$, after which the disturbance environment moves upstream and the subsequent vortex rings instability occurs a little closer to the stenosis. As a result the levels of turbulent kinetic energy shown after $t/t = 0.5$ are considerably lower when they reach $x/h = 20$. Similar behavior can be observed for the turbulent Reynolds shear stresses in figure 4.29e . Overall turbulent activity appears to have decayed to negligible levels after $t/T = 0.8$.

Further downstream in the reattached flow region the turbulent activity changes

considerably as shown in figures 4.29c and f. First of all the arrival of the leading front of turbulence is not as sharp as in the previous two locations. There is a more gradual increase in the levels of turbulent kinetic energy from $t/T = 0.35$ to $t/T = 0.45$ corresponding to the arrival of the leading patch of turbulence resulting from the roll-up process. The turbulent kinetic energy peaks at $t/T = 0.5$ and the radial location is now clearly closer to the wall. Both turbulent kinetic energy and turbulent Reynolds shear stresses start decaying after the maximum flow rate but do not dissipate completely until the end of the deceleration.

Qualitatively the turbulent flow characteristics in the axisymmetric configuration resemble a lot those of the planar configuration for the corresponding Reynolds number and reduced velocity. It is clear that the turbulent activity is driven by the dynamics of the shear layer, which is also consistent with the observations of the instantaneous dynamics of the flow. In particular, within the wall layer downstream of the reattachment point, the turbulent kinetic energy production is mostly sustained by the evolution/interaction of large vortical structures. This trend can be more clearly observed in figure 4.30 where the time evolution of the near wall maxima of the phase-averaged turbulent kinetic energy and its production at a location within the region of the 'synthetic' turbulent boundary layers (approximately 16R downstream part the mean reattachement point, is shown. The cases with the largest reduced velocity is not shown because the corresponding downstream location was very close to the domain outlet. It is clear that in all cases except case 4, the turbulent kinetic energy appears in a burst. As the Reynolds number is increased the turbulent front arrives a little earlier due to the fact that the shear layer becomes

unstable earlier in the cycle. In addition turbulent kinetic energy and production decay more gradually. However in both cases the duration of the turbulent production corresponds closely with the duration of the active structure formation duty cycle of the shear layer (including the roll-up process). For the case with $U_{red} = 13.275$ finite values of turbulent kinetic energy and production are found throughout the cycle. Inspection of the instantaneous flow visualizations reveal that the patch of turbulent-like structures formed near the stenosis does not completely dissipate in one cycle and remain in the near-wall region for the majority of the cycle. This is most likely because the reduced velocity becomes smaller the duration of the pulsatile cycle becomes comparable to the turnover time of the vortices and the small stroke length enables the relatively few active structures to remain in the near-wall region for the majority of the cycle.

The flow patterns above are reflected in the behavior of the wall shear stress. Figure 4.31 shows the phase-averaged skin friction coefficient, $\tilde{c}_f = 2\tilde{\tau}_w/\rho U_b^2$, and the corresponding root-mean-square fluctuations, c_f''. To illuminate the spatio-temporal behavior of the above quantities, iso-contours in the x/R vs $\hat{t} = 2\pi t/T$ space are shown. For clarity, only the part of the walls downstream of the stenosis ($x/R > 1.0$) is included in the figure.

Very distinct patterns can be identified in the spatio-temporal evolution of the wall stress. Near the minimum flowrate at $\hat{t} \sim -0$, the phase-averaged wall stress is predominantly positive throughout the channel. As the flowrate increases, a recirculating area is formed just downstream of the throat of the stenosis. The size of the recirculating bubble increases with time and reaches a maximum of downstream

distance of $x/R \sim 20$ at $\hat{t} \sim 0.35\pi$, as indicated by the location of the reattachment line in figure 4.31a. Around this instant in the pulsatile cycle, the shear layer becomes unstable and the roll-up process is initiated, resulting in an alternating pattern of negative and positive shear stress being imposed on the wall's surface. In figure 4.31a this is manifested by the long streaks of negative $\tilde{c}_f$ moving diagonally up and to the right in the $x/R - \hat{t}$ space. The slope of these streaks equals the inverse of the velocity of propagation of the vortex rings indicating that the c_f patterns move along with the structures. We should also note that near the stenosis ($x/R < 8.0$), the above alternating pattern is also fairly regular and repeatable from cycle-to-cycle, as indicated by negligible levels of incoherent fluctuations ($c_f'' \sim 0$ as shown in figure 4.31b. This pattern persists during part of the deceleration phase, up to $\hat{t} \sim 0.7$. The maximum levels of c_f'' occur around the reattachment point.

Downstream of the reattachment line, a very different behavior can be observed. The wall stress in this case is always positive and two very distinct patterns can be identified: on one hand, for most of the acceleration and part of the deceleration phase, the magnitude of $\tilde{c}_f$ is consistent with developing, laminar, pulsatile flow and c_f'' is practically zero; on the other hand, near the peak flowrate and for a considerable part of the deceleration ($-0.35 < \hat{t} < 0.8$) the magnitude of $\tilde{c}_f$ is increasing by a factor of two, accompanied by a dramatic increase in the levels of c_f''. This is a result of the interaction of the vortex rings with the wall layer that is perturbed and tends to transition to turbulence. In this range of Reynolds numbers, however, the disturbances decay fairly fast and a clear logarithmic layer cannot be established in the region downstream of the mean reattachment point.

Although we cannot directly correlate these results with previous *in-vivo* and *in-vitro* experiments designed to illuminate the mechanisms involved in endothelial mechanotransduction, it is clear that in the proximal post-stenotic area very distinct spatio-temporal patterns of the wall shear stress with very different temporal scales can be identified. Just downstream of the stenosis exposed cells would be subjected to a smooth and repeatable temporal shear stress gradient imposed by the shear layer roll-up. This pattern would be probably closer to conditions that promote endothelial proliferation [18]. Further downstream the high values of C_f'' suggest that instantaneously the shear stress undergoes big changes both in magnitude and direction over a small localized area. This could be an indication that in this part of the channel the wall stress could initiate higher endotelial cell turnover than in others parts of the channel.

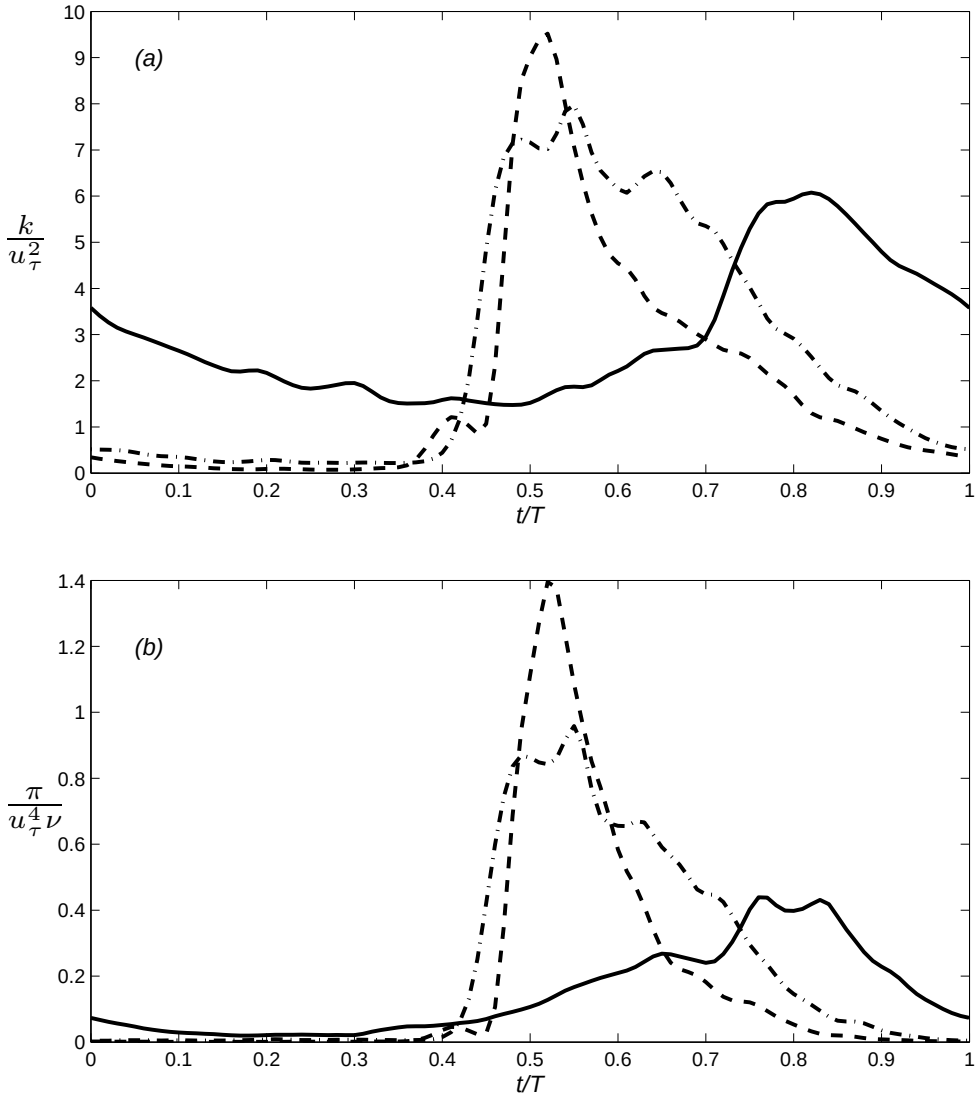

Figure 4.30: (a) near wall maxima of the phase-averaged turbulent kinetic energy and (b) turbulent kinetic energy production as a function of time at $x/R = 16$ downstream of the mean reattachment point, ——— ; case 7 ($Re = 600$, $U_{red} = 6.6$), - - - ; case 6 ($Re = 600$, $U_{red} = 26.5$), —·— ; case 8 ($Re = 1200$, $U_{red} = 26.5$).

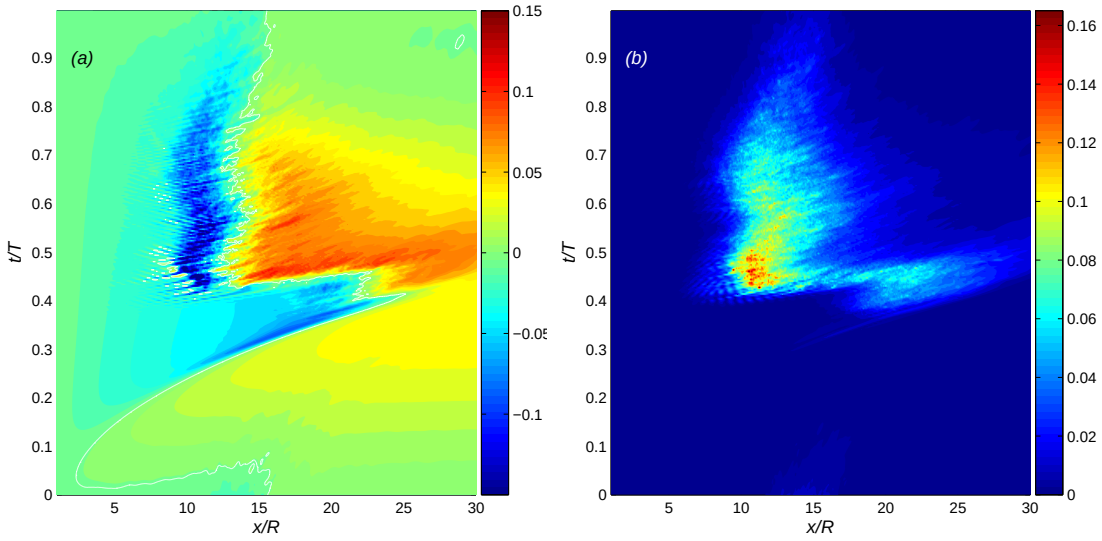

Figure 4.31: Spatio-temporal evolution of the phase-averaged statistics of the skin friction coefficient. (a) $\tilde{c}_f$; (b) c_f''. The dashed line corresponds to $\tilde{c}_f = 0$.

Chapter 5

Blood Rheology

Having identified the mechanisms by which transition takes place, in this section the non-Newtonian effects of blood on the turbulent characteristics downstream of a stenosis are investigated. Although shear thinning fluids like blood would be expected to behave like a Newtonian fluid in the range of Reynolds number investigated, an experimental study by Stein *et al.* [55], that showed that the presence of red blood cells in blood can alter significantly the turbulence characteristics in the post-stenotic region. First, blood rheology and different viscosity models that account for its shear-thinning behaviour are discussed. A low-Reynolds number simulation for purposes of validating the non-Newtonian model is presented. Finally, results from a simulation at the same configuration as the above experiment are shown and the effects of a commonly employed non-Newtonian viscosity model on post-stenotic turbulence are assessed.

One of the most important considerations in simulating blood flow in atherosclerotic vessels is employing a viscosity model that accurately represents the rheology of blood. Blood itself is a non-Newtonian fluid. It consists of plasma and a suspension of red cells, white cells and platelets. Plasma itself is about 90% water plus some proteins and behaves as a Newtonian fluid. It is the presence of the blood cells, and in particular the red cells or erythrocytes that make blood non-Newtonian. Human

red blood cells are deformable disk shaped objects, with a diameter of $7.6\mu m$ and thickness $2.8\mu m$ and occupy about 50% of the blood volume. As show in fig. 5.1, for blood with no hematocrit, defined as percentage of total volume of blood occupied by cells, the viscosity is independent of the shear rate, while blood with higher hematocrit have a non-linear dependence on shear rate. The higher the hematocrit levels, the higher the viscosity of blood is. When the blood flow is stagnant, the red blood cells tend to join together and form aggregates known as *rouleau*. The blood at this state most probably behaves like an elastic solid and has a finite yield stress. When the shear rate increases the aggregates begin to break apart and the viscosity of the blood is reduced. If the shear rate exceeds $10s^{-1}$, particle aggregation ceases to become important and individual red blood cells start to deform and line up with the streamlines of the flow. This further reduces the viscosity of the blood as shown in figure 5.2. Finally, for shear rates higher than $700s^{-1}$ blood appears to be Newtonian. In large and small arteries the shear rate ranges from $100s^{-1}$ to $2000s^{-1}$ and except near the centerline blood is expected to behave like a Newtonian fluid. Based on these facts, a lot of empirical models have been developed to account for the non-Newtonian nature of blood at low shear rates. The Herschel-Bulkley model for example can be written as:

$$\eta(\dot{\gamma}) = \tau_y/\dot{\gamma} + K\dot{\gamma}^{n-1} \quad , \dot{\gamma} > \dot{\gamma_c}$$

$$\eta(\dot{\gamma}) = \eta_{max} \quad , \dot{\gamma} < \dot{\gamma_c}$$

where τ_y is the yield stress, n the power index, γ_c the critical shear rate and K

is the consistency factor [12]. When $n = 1$ and $\tau_y \neq 0$ the above equation produces the biviscosity model, when $n \neq 1$ and $\tau_y \neq 0$ it produces a Bingham fluid and when $n \neq 1$ and $\tau_y = 0$ it produces a power law fluid. The above models are empirically obtained for unidirectional flows and approximate well the viscosity of blood in laminar regimes [19]. In turbulent regimes though the development of mathematical and computational models for the viscosity of blood is not well advanced. Experimental results on shear thinning fluids in turbulent pipe flows, although not blood in particular, show that the fluids tested preserve their rheological properties predicted by the Herschel-Bulkley model [40]. It is generally observed that with shear thinning fluids the transition to turbulence is delayed (i.e. transition occurs at higher Reynolds number). Usually only the radial and transverse velocity fluctuations are lower by $20\% - 40\%$ compared to a Newtonian fluid while the axial turbulent intensities are not affected [47, 41]. In these comparisons, the Reynolds number in the case of the non-Newtonian fluid is based on the mean wall viscosity, since it is the near wall region that plays a fundamental role in transition and development to turbulence in wall bounded flows. In addition, direct numerical simulations of weakly turbulent flow using the Hurschel-Bulkley model have been performed and are in good agreement with experiments [46]. However none of the above studies of the rheology and effects of non-Newtonian fluids in turbulence involved actual blood.

To date, the only experiments to study the effect of blood on the intensity of turbulence were carried out by Stein *et al.* in the 70s [55, 48]. They measured the turbulent intensities downstream of a sharped stenosis in a pipe using a hot

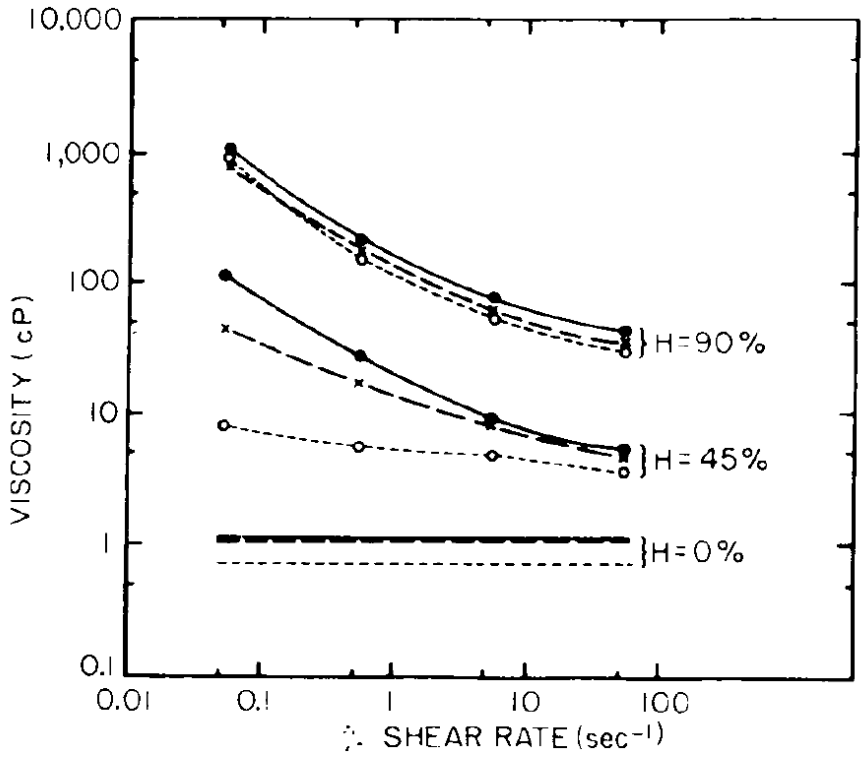

Figure 5.1: Viscosity dependence on shear rate for various levels of hematocrit (H). In blood with no red cells the shear rate is constant. As the percent of hematocrit increases blood behaves as non-Newtonian fluid. From [10].

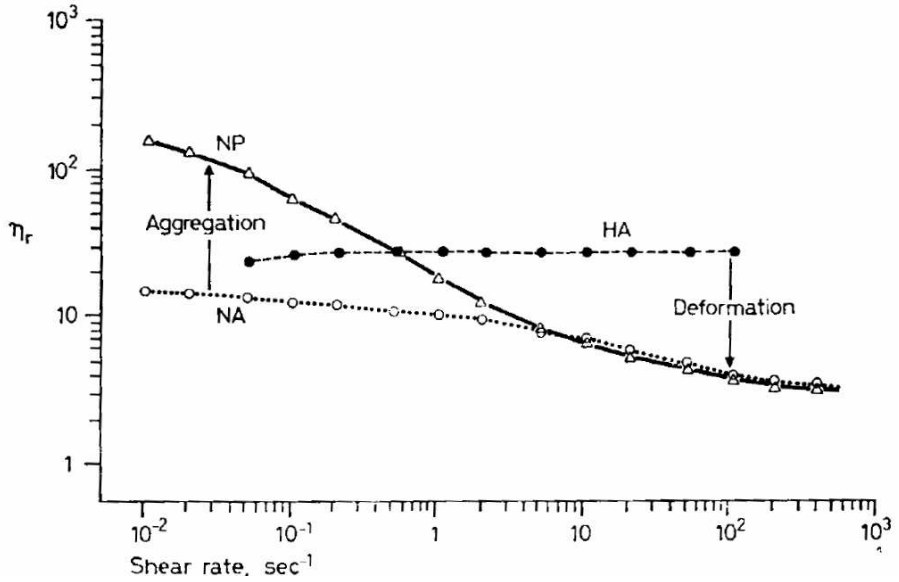

Figure 5.2: Blood viscosity dependence on red cell deformability. NP=normal red blood cells in plasma; NA=normal red blood cells in 11% albumin to prevent formation of *rouleaux*; HA = hardened red blood cells in 11% albunim to prevent deformation of cells. From [9].

film anemometer. The working fluid was either plasma or blood with different levels of hematocrit. The density of plasma was made equal to the density of blood by addition of dextrose, which kept the plasma mixture Newtonian. The apparent viscosity of blood was calculated by the Poiseuille equation and was adjusted so that for the same pressure gradient in the pipe identical flow rates of plasma and blood were achieved. The Reynolds number, based on the apparent viscosity, the pipe radius and the mean velocity of the fluid varied from 100 to 300. They found that the relative intensity of turbulence (defined as the turbulent intensity normalized by the mean velocity) increased dramatically in blood as the percent of hematocrit increased. At hematocrit between 20 and 30 percent, the intensity of turbulence of the blood was two to three times greater than that of plasma (see figure 5.3). With

further increment of the hematocrit levels the turbulent intensity decreased and at a level of 40 percent it approached that of plasma. In all the tests the apparent viscosity of blood did not differ more than 10% irrespective of the mean velocity. The average shear rate on the wall pipes varied between 147 and 613 sec^{-1}, at which blood of 40% hematocrit is virtually Newtonian. This demonstrated that the observed changes in turbulence intensities between plasma and blood was due to the presence of erythrocytes and not due to changes in apparent viscosity that may arise from the local differences in shear rate. They speculated that the observed augmentation of turbulence could be due to the slip postulate or due to the red blood cells acting as spot generators of small disturbances. To date no numerical simulations were able to reproduce the trends demonstrated by Stein *et al.*. Thus we have numerically tried to reproduce the above results by performing a DNS at a Reynolds number of 320 with the same geometrical configuration as in the experiments and employing a simple non-Newtonian model.

5.1 Validation of non-Newtonian model in Laminar Flows

As a first step, the implementation of non-Newtonian model in equation 5.1 was validated in a laminar flow. The validation case consisted of a low Reynolds number steady flow in a pipe with an axisymmetric stenosis whose shape is given by:

$$r = R \cdot (1 - 0.5e^{-4x^2/R^2}) \tag{5.1}$$

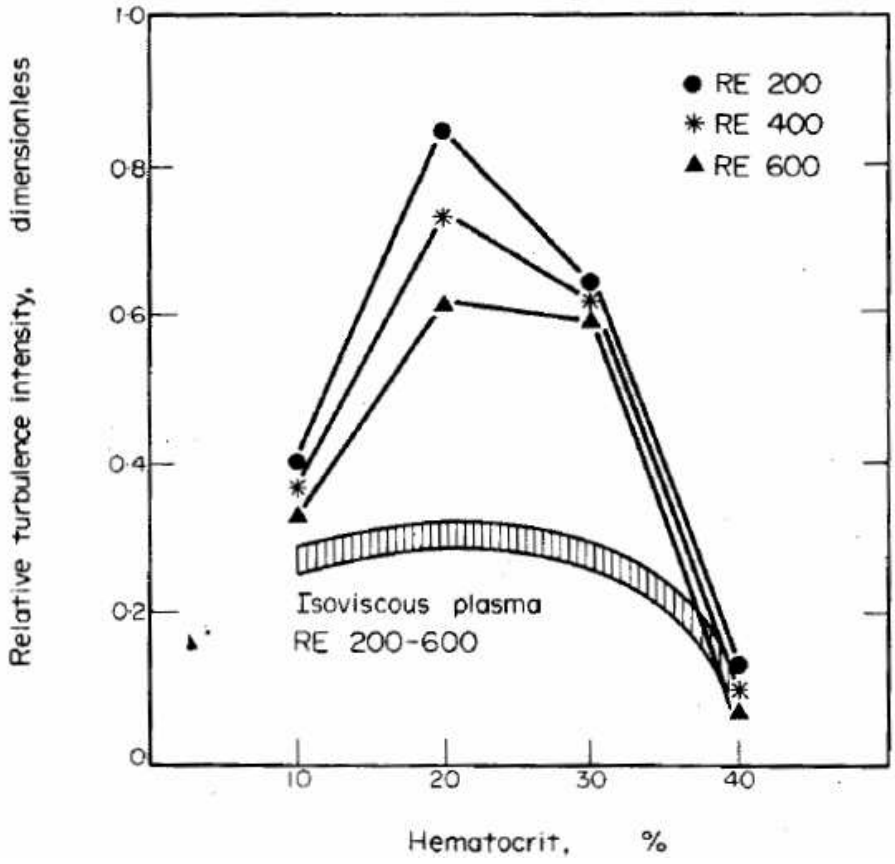

Figure 5.3: Relative turbulent intensities 20 diameters downstream of a sharp stenosis as a function of hematocrit at various Reynolds numbers. From [55].

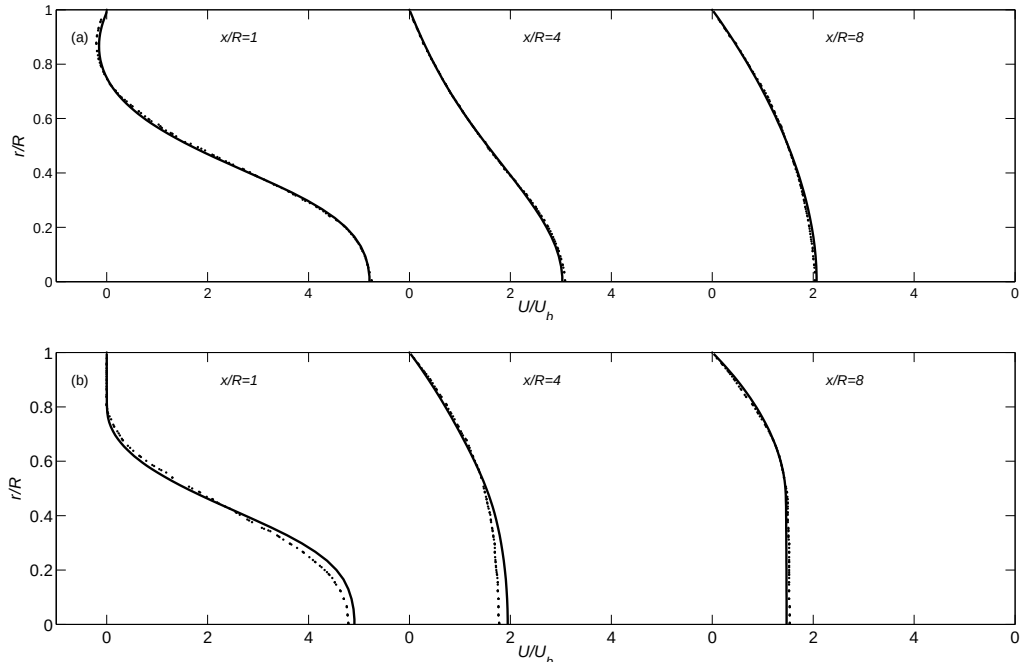

Figure 5.4: Comparison of of the axial velocity profiles (Beratlis; -, Nakamura; .) at three locations; $x/R = 1$, $x/R = 4$, and $x/R = 8$. a) Re=20, He=0 (Newtonian) b) Re=20, He=376 (biviscosity model).

The results from our simulation were compared against those carried out by Nakamura [34]. In their simulations they employed a simple biviscosity model to represent blood and used a dimensional parameter, called the Hedstrom number to denote the non-Newtonian effects. This parameter is defined as:

$$He = 4\rho\tau_y R^2/\mu_\beta^2, \tag{5.2}$$

where ρ is the density of the blood, τ_y is the yield stress of the blood and μ_β is the plastic viscosity. These values were chosen to be $\rho = 1050kg/m^3$, $\mu_\beta = 3.5e^{-3}Pa$ and $\tau_y = 0.27Pa$. An upper limit of $He_{max} = 580$ was set to avoid a singularity in equation 5.1 wherever the local shear rate becomes zero.

The velocity profiles for Re=20, He=0 (Newtonian) and Re=20, He=376 at three downstream locations (near the edge of the stenosis and downstream of it) are shown in figure 5.4. In both cases the velocity profiles agree well with those of Nakamura [34]. In the Newtonian case the flow separates downstream of the stenosis as shown by a region of negative velocity at $x/R = 1$. However in the non-Newtonian case a recirculation bubble is not present. In addition the velocity profiles at $x/R = 4$ and 8 exhibit a flatness region. This is a characteristic of biviscosity model since small velocity gradients near the core of the pipe result in high values of viscosity.

5.2 DNS of Non-Newtonian fluid downstream of an Axisymmetric Stenosis

The same biviscosity model used in the validation case above was used to represent blood. Two simulations with the Newtonian and non-Newtonian model was carried out first at a target Reynolds number of 320. The apparent viscosity of the flowing blood in the non-Newtonian case was calculated by Poiseuille equation:

$$\mu = dP/dx \cdot R^2/8U_b \tag{5.3}$$

where dP/dx is the pressure gradient upstream of the stenosis. The Reynolds number based on the apparent viscosity is 326.

The domain of the simulation extended 15R and 60R upstream and downstream of the stenosis. The grid used contained 54x32x794 points in the radial,

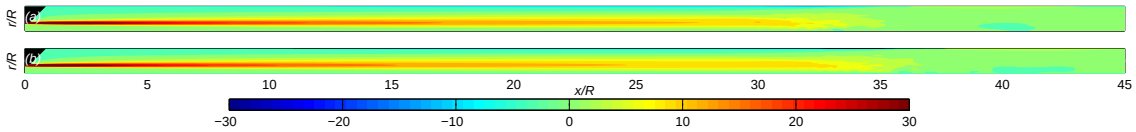

Figure 5.5: Contours of azimuthal vorticity normalized by the bulk velocity and radius of the pipe averaged over time and azimuthal direction in $r - x$ space. The Reynolds number in both cases is 320. a) non-Newtonian b) Newtonian case.

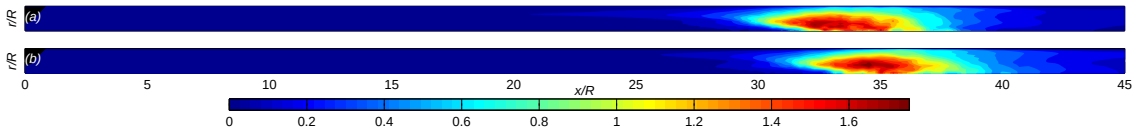

Figure 5.6: Contours of axial turbulent intensity normalized by the bulk velocity averaged over time and azimuthal direction in $r - x$ space. The Reynolds number in both cases is 320. a) non-Newtonian b) Newtonian case.

azimuthal and axial direction respectively. A fully developed parabolic velocity profile was prescribed at the inlet. A sharp stenosis with 89% occlusion is used. More details about the shape of the stenosis can be found in [55]. Statistics were sampled for about 20 time units, after the flow had reached a steady state.

Figures 5.5 and 5.5 shows contours of the azimuthal vorticity and axial turbulent intensities plotted in $r - x$ space for both Newtonian and non-Newtonian cases. In the Newtonian case the shear layer extends about one pipe radius further downstream than in the non-Newtonian. This is expected as the flat velocity profile in the core of the jet would increase the viscosity of the fluid and effectively slow down the fluid, similar to the extend of the recirculation bubble in the laminar case. In both cases the shear layers which extend to about 17 pipe diameters downstream of the stenosis shed vortices which undergo three dimensional instabilities giving rise

to turbulent activity near the reattachment point. As a result there exists a region between 15 and 20 diameters downstream of the stenosis where the axial turbulent intensities have the highest levels. In the non-Newtonian case this region precedes the one in the Newtonian case by approximately one pipe radius. However the levels in both cases are comparable to each other. The highest turbulent intensities anywhere in the flow normalized by the bulk velocity in the non-Newtonian case is 1.77 while in the Newtonian case it is 1.84. This is a difference of only 4% and contrary to the experiments the axial turbulent intensity is highest in the Newtonian case. At the centerline the maximum of the axial turbulent intensities normalized by the local mean velocity are 0.41 and 0.46 for the non-Newtonian and Newtonian cases and they occur at $x/R = 37.7$ and $x/R = 40.0$ respectively. The sensor of the hot film probe in the experiments by Stein *et al.* was placed at $x/R = 40.0$. The turbulent intensity at that location for the non-Newtonian case is 0.12. Although this value is dramatically lower than the corresponding value in the Newtonian case it would be misleading to compare turbulent statistics at fixed locations. At this point one could wonder if the large differences in turbulent intensities observed in the experiment can be explained purely on the basis of the different localization of the turbulent front breakdown. For example, if the probe is located just upstream of the transition in the Newtonian case and inside the core of turbulence patch in the non-Newtonian case that would give rise in the turbulent intensities. However, the differences in the experiment for the axial turbulent intensity were consistently observed for a range of Reynolds number, in which the location of transition can change. There are many uncertainties in the above mentioned experiment, mainly

the lack of the spatial state of turbulence and measurements techniques. The present simulations show that there are no major qualitative or quantitative differences between the two cases when employing a simple biviscosity model to account for the non-Newtonian nature of blood. If the trends observed by Stein *et al.* are true then a more sophisticated model that would take into account the red blood cells interactions with the turbulence structures is needed.

Chapter 6

Summary and conclusions

In the present study we investigated the physics of pulsatile transitional flows through a constriction by means of DNS. Such computations are very demanding in terms of CPU time. We therefore, first, optimized the staggered Cartesian/Cylindrical coordinates solver developed by Balaras et co-workers [5, 61] to scale on large computational clusters. The code was tested for various grids and linear scaling was achieved with as many as 500 processors and grids of 1.1 billion points. The key point in achieving linear scaling is performing efficiently the communication for the domain redistribution associated with the Poisson solver. This is done by sending data to and receiving data from one processor to each in order of processors with rank closer to each other.

In terms of flow physics, DNS of transitional pulsatile flow in an idealized planar and cylindrical channel with a constriction have been presented. One simulation in the planar geometry was closely coordinated with an experiment to validate the computations and guide the development of proper inflow boundary conditions was conducted. The results show that during part of the pulsatile cycle the flow upstream of the stenosis undergoes a transition from a laminar to a 'disturbed-laminar' state as a result of an instability associated with the inflection points in the velocity profiles. This is also true in cylindrical coordinates when random noise was added

to the inflow. We found that reproducing this state is important to properly capture transition downstream of the constriction. In general, the DNS results were in very good agreement with the experiment, and the formation and instability of the confined jet through the stenosis was captured accurately. In addition, the phase-averaged velocity statistics of the streamwise velocity follow very closely those from the experiment.

Having established the validity of the simulations, the instantaneous flow dynamics were investigated. It was found that there are two principal mechanisms responsible for the transition to turbulence; the initial stages of the shear layer roll-up and a shear layer instability. In the first one quasi two-dimensional vortical structures originating from the initial stages of a shear layer instability undergo three-dimensional instabilities as they interact with the wall and form Λ-type structures. During the second one the shear layer sheds vortices reminiscent of those found in a typical mixing layer with the existence of spanwise rollers undergoing three-dimensional instabilities and rib-vortices in the braid areas. Despite the differences, both mechanisms essentially reorient the spanwise vorticity into the streamwise direction, constantly feeding the reattached wall layer with turbulent-like structures. It was found that as the reduced velocity or Reynolds number is increased the shear layer begins to roll-up earlier in the cycle and the vortex shedding lasts longer in the pulsatile cycle. On the other hand as the reduced velocity is decreased the amount of circulation imparted in the shear layers is smaller and the second mechanism becomes less dominant.

We also presented phase-averaged statistics of the velocity field and turbulent

kinetic energy budgets. These results indicate that the overall turbulent activity is driven by the dynamics of the shear layer, which is also consistent with the observations of the instantaneous dynamics of the flow. Turbulent kinetic energy is produced at the shear layers and is transported towards the core of the channel, where it remains 'passive' and decays as it is convected downstream. Production of turbulent kinetic energy in the wall-layer further downstream, although a dynamically different process, is practically sustained by the evolution/interaction of large vortical structures that originate from the shear layers.

Finally the effect of the Reynolds and the reduced velocity on the near wall turbulence was discussed. It was observed that by increasing the Reynolds the shear layers instability (and consequently turbulence production) is initiated earlier in the cycle. However for the cases with higher U_{red} the turbulence activity could not be sustained during the entire cycle. It is observed that as the time-scale of the imposed oscillations increases dissipation has more time to act and completely kills the turbulent structures present in the reattached wall-region. Only for the case with $U_{red} = 6.6$ is turbulent kinetic energy sustained during the entire cycle.

A series of simulations in cylindrical coordinates varying the Reynolds number and reduced velocity have also been carried. The flow physics are qualitatively very similar to those in cartesian coordinates; namely a roll-up structure followed by shedding of vortex rings from the shear layer. It has been observed that as the shear layer begins to roll-up the first streamwise vortical structures are formed as a result of the interaction between the roll-up structure and the shear layer through vortex strecthing and reorientation of the azimuthal and radial vorticity. For the

largest reduced velocity a mode 1 instability is dominant during this roll-up process resulting in the generation of horse-shoe like vortex, while for the smallest reduced velocity mode 2 instability dominates resulting in the generation of two pairs of streamwise-oriented vortical structures. For the highest Reynolds number it appears that this roll-up stage is bypassed. Following the formation of these turbulent-like vortical structures the shear layer becomes unstable and starts shedding a series of vortex rings. These vortex rings undergo three-dimensional instabilities that directly transform their azimuthal into axial vorticity. Both mechanisms have the same effect; the generation of a turbulent-like wall region further downstream of the mean reattachment point. For the parametric space investigated, as the reduced velocity is decreased turbulent activity is sustained throughout the cycle. As the Reynolds number is increased the duration of turbulent activity is increased as the shear layer becomes unstable earlier in the cycle.

Finally, the effects of blood rheology on post-stenotic turbulent activity have been investigated. Blood was treated as non-Newtonian fluid employing a simple biviscosity model and a simulation was setup based on the experiments by Stein *et al.* [55]. It was found that the shear layer extends about 1 pipe radius futher downstream in the Newtonian case than in the non-Newtonian case. This can be explained in terms of the increased viscosity in the core jet region for the non-Newtonian case. Turbulent intensities however did not differ by more than 4% globally, showing that shear shinning viscosity models do not alter significantly the turbulent statistics in the post-stenotic region.

Bibliography

[1] *Turbulent Fluid Shear Stress Induces Vascular Endothelial Cell Turnover in vitro* (1986), vol. 83 of *Proceedings of the National Academy of Sciences of the United States of America*.

[2] Ahmed, S. A., and Giddens, D. P. Pulsatile poststenotic flow studies with laser doppler anemometry. *Journal of Biomechanics 17* (1984), 695–705.

[3] Asakura, T., and Karino, T. Flow Patterns and Spatial Distribution of Atherosclerotic Lessons in Human Carotid Arteries. *Circ. Res 11* (1972), 63–73.

[4] Balaras, E. *Large eddy simulation of high Reynolds number wall bounded shear layers*. PhD thesis, Swiss Federal Institute of Technology, 1995.

[5] Balaras, E. Modeling Complex Boundaries Using an External Force Field on Fixed Cartesian Grids in Large-Eddy Simulations. *Journal of Fluid Mechanics 33* (2004), 375–404.

[6] Blackburn, H. M., and Sherwin, S. J. Instability modes and transition of pulsatile stenotic flow: pulse-period dependence. *Journal of Fluid Mechanics 573* (2007), 57–88.

[7] Cassanova, R. A., and Giddens, D. P. Disorder Distal To Modeled Stenoses In Steady and Pulsatile Flow. *Journal of Biomechanics 11* (1978), 441–453.

[8] Center for Turbulence Research. *Eddies, Streams and Convergence Zones in Turbulent Flows* (1988), no. 193, Proceedings of the Summer Program 1988.

[9] Chien, S. Shear dependence of effective cell volume as a determinant of blood viscosity. *Science 168* (1970), 977–979.

[10] Chien, S., Usami, S., Taylor, M., Lundberg, J. L., and Gregersen, M. I. Effects of hematocrit and plasma proteins of human blood rheology at low shear rates. *Journal of Appl. Physiol. 21* (1966), 81–87.

[11] Chiu, J. J., Wang, D. L., Chien, S., Skalak, R., and Usami, S. Effects of Disturbed Flow on Endothelial Cells. *Journal of Biomechanical Engineering 120* (2001), 2–8.

[12] Crochet, M. J., Debbaut, B., Keunings, R., and Marchal, J. M. Ploflow: a multi-purpose finite-element program for continuous polymer flows,. In *Computer Modelling of Extrusion and Other Continuous Processes* (Hanser, Munich, 1992), K. O. Brien, Ed., pp. 25–50.

[13] Das, D., and Arakeri, J. H. Transition of unsteady velocity profiles with reverse flow. *Journal of Fluid Mechanics 374* (1998), 251–283.

[14] Friedman, M. H., Peters, O. J., Bargeron, C. B., Hutchins, G. M., and Mark, F. F. Shear-Dependent Thickening of the Human Arterial intima. *Atherosclerosis 60* (1986), 161–171.

[15] Gharib, M., Rambod, E., and Sharrif, K. A universal time scale for vortex ring formation. *Journal of Fluid Mechanics 360* (1998), 121–140.

[16] Grottum, P., Svindland, A., and L., W. Localization of Atherosclerotic Lessions in the Bifurcation of the Left Main Coronary Artery. *Atherosclerosis 47* (1983), 55–62.

[17] Haidari, A. H., and Smith, C. R. The generation and regeneration of single hairpin vortices. *Journal of Fluid Mechanics 277* (1994), 135–162.

[18] Haidekker, M. A., White, C. R., and Frangos, J. A. Analysis of Temporal Shear Stress Gradients During the Onset Phase of Flow over a Backward-Facing Step. *Journal of Biomechanical Engineering 123* (2001), 455–463.

[19] Han, S., Marseille, O., Gehlen, C., and Blumich, B. Rheology of Blood by NMR. *Journal of Magnetic Resonance 152* (2001), 87–94.

[20] Head, M. R., and Bandyopadhyay, P. New aspects of turbulent boundary-layer structure. *Journal of Fluid Mechanics 107* (apr 1981), 297–338.

[21] Heist, D. K., Henratty, T. J., and Na, Y. Observations of the formation of streamwise vortices by rotation of arch vortices. *Physics of Fluids 12* (2000), 2965–2975.

[22] Hino, M., Sawamoto, M., and Takasu, S. Experiments on transition to turbulence in an oscillating pipe flow. *Journal of Fluid Mechanics 75* (1976), 193–207.

[23] J., R., Straatman, A. G., and Steinman, D. A. Two-equation Turbulence Modeling of Pulsatile Flow in a Stenosed Tube. *Journal of Biomechanical Engineering 126* (2004), 625–635.

[24] Khalifa, A. M. A., and Giddens, D. P. Analysis of Disorder In Pulsatile Flows with Application To Poststenotic Blood Velocity Measurement in Dogs. *Journal of Biomechanics 11* (1978), 129–141.

[25] Khalifa, A. M. A., and Giddens, D. P. Characterization and evolution of poststenotic flow disturbances. *Journal of Biomechanics 14* (1981), 279–296.

[26] Lasheras, J. C., Cho, J. S., and Maxworthy, T. On the origin and evolution of streamwise vortical structures in a plane, free shear layer. *Journal of Fluid Mechanics 172* (1986), 231–258.

[27] Lee, A. A., Graham, D. A., Cruz, S. D., Ratcliffe, A., and Karlon, W. J. Fluid Shear Stress-Induced Alignment of Cultured Vascular Smooth Muscle Cells. *Journal of Biomechanical Engineerin 124* (2002), 37–43.

[28] Lieber, B. B., and Giddens, D. P. Post-stenotic core flow behavior in pulsatile flow and its effects on wall shear stress. *Journal of Biomechanics 23* (1990), 597–605.

[29] Liu, P. C., Gross, D. R., and Hwang, N. H. C. Intravascular pressure and velocity fluctuations in pulmonic arterial stenosis. *Journal of Biomechanics 13* (1980), 291–300.

[30] Mayo, W. Spectrum measurements with laser velocimeters. In *Dynamic Measurements in Unsteady Flows; Proc. Dynamic Flow Conf.* (Marseille, France, 1978).

[31] Merkli, P., and Thomann, H. Transition to turbulence in oscillating pipe flow. *Journal of Fluid Mechanics 68* (1975), 567–575.

[32] Mittal, R., Simmons, S. P., and Udakumar, H. S. Application of large-eddy simulation to the study of pulsatile flow in a modeled arterial. *Journal of Biomechanical Engineering 123* (2001), 325–332.

[33] Montenegro, M. R., and Eggen, D. A. Topography of atherosclerosis in the coronary arteries. *Lan. Invest. 8* (1968), 586–593.

[34] Nakamura, M., and Sawada, T. Numerical Study on the Flow of a non-Newtonian Fluid Through an Axisymmetric Stenosis. *Journal of Biomechanical Engineering 110* (1988), 137–143.

[35] Nerem, R. M., and Seed, W. A. An in vivo study of aortic flow disturbances. *Cardiovascular Research 52* (1972), 137–160.

[36] Nerem, R. M., Seed, W. A., and Wood, N. B. An experimental study of the velocity distribution and transition to turbulence in the aorta. *Journal of Fluid Mechanics 52* (1972), 137–160.

[37] Ojha, M., Iguchi, M., Kakehachi, K., and Masuda, T. Pulsatile flow through constricted tubes: an experimental investigation using photochromic tracer method. *Journal of Fluid Mechanics 203* (1989), 173–197.

[38] Orlansky, I. A simple boundary condition for unbounded hyperbolic flows. *Journal of Comput. Phys. 21* (1974).

[39] Ovchinnikov, V., Piomelli, U., and Choudhari, M. M. Inflow Conditions for Numerical Simulations of Bypass Transition. *AIAA paper*, 591 (2004).

[40] Peixinho, J., Nouar, C., Desaubry, C., and Theron, B. Laminar transitional and turbulent flow of yield stress fluid in a pipe. *Journal of Non-Newtonian Fluid Mech. 128* (2005), 172–184.

[41] Pinho, F. T., and Whiteflaw, J. H. Flow of non-Newtonian fluids in a pipe. *Journal of Non-Newtonian Fluid Mechanics 34* (1990), 129–144.

[42] Poelma, C. *Experiments in particle-laden turbulence*. PhD thesis, Technische Universiteit Delft, 2004.

[43] Poelma, C., Westerweel, J., and Ooms, G. Turbulence statistics from optical whole-field measurements in particle-laden turbulence. *Exps. Fluids 40* (2005), 663.

[44] Rogallo, R. S. Numerical experiments in homogeneous turbulence. Technical Memo 81315, NASA, 1981.

[45] Rosenfield, M., Rambod, E., and Gharib, M. Circulation and formation number of laminar vortex rings. *Journal of Fluid Mechanics 376* (1998), 297–318.

[46] Rudman, M., and Blackburn, H. M. The Effect of Shear Thinning Behaviour on Turbulent Pipe Flow. In *Third International Conference on CFD in the Minerals and Process Industries* (Australia, 2003).

[47] Rudman, M., Blackburn, H. M., Graham, L. J. W., and Pullum, L. Turbulent pipe flow of Non-Newtonian fluids. *Journal of Non-Newtonian Fluid Mechanics 18*, 1 (2004), 297–318.

[48] Sabbah, H. N., and Stein, P. D. Effect of Erythrocytic Deformability upon turbulent blood flow. *Biorheology 13* (1976), 309–314.

[49] Sallam, A. M., and Hwang, N. H. C. Human Red Blood Cells Hemolysis In a Turublent Shear Flow. *Biorheology 21* (1984), 783–797.

[50] Schwartz, C. J., and Mitchell, J. R. A. Observations on Localizations of Arterial Plaques. *Circ. Res 11* (1972), 63–73.

[51] Scotti, A., and Piomelli, U. Turbulence models in pulsating flows. *AIAA paper*, 729 (2001), 537–540.

[52] Seed, W. A., and Wood, N. B. Velocity patterns in the aorta. *Cardiovascular Research 5* (1971), 319–330.

[53] Sherwin, S. J., and Blackburn, H. M. Three-dimensional instabilities and transition of steady and pulsatile axisymmetric stenotic flows. *Journal of Fluid Mechanics 533* (2005), 297–327.

[54] Siouffi, M., Deplano, R., and Pelissier, R. Experimental analysis of unsteady flows through a stenosis. *Journal of Biomechanics 31* (1998), 11–19.

[55] Stein, P. D., Sabbah, H. N., and Blick, E. Contribution of Erythrocytes to Turbulent Blood Flow. *Biorheology 12* (1975), 293–299.

[56] Stroud, J. S., Berger, S. A., and Saloner, D. Numerical Analysis of Flow Through a Severely Stenotic Carotid Artery Bifurcation. *Journal of Biomechanical Engineering 124* (2002), 9–20.

[57] Swarztauber, P. N. Direct Method for the discrete solution of separable elliptic equations. Report TF-63, ThermoSciences Div.,, Stanford University, 1974.

[58] Swarztauber, P. N. Fast Fourier Transforms Algorithms for Vector Computers. *Parallel Computing* (1984), 45–63.

[59] Varghese, S. S., and Frankel, S. H. Numerical modeling of pulsatile turbulent flow in stenotic vessels. *Journal of Biomechanical Engineering 125* (2003), 335–360.

[60] Wallace, J. M., Eckelmann, H., and Brodkey, R. S. The wall region in turbulent shear flow. *Journal of Fluid Mechanics 54* (1972).

[61] Yang, J. *An Embedded-Boundary Formulation for Large-Eddy Simulation of Turublent Flows Interacting with Moving Boundaries*. PhD thesis, University of Maryland, 2005.

[62] Yoganathan, A. P., and Jones, S. C. Fluid Mechanics of Heart Valves. *Ann. Rev. Biomed. Eng. 6* (2004), 331–362.

[63] Zhao, W., Frankel, S. H., and Mongeau, L. G. Effects of trailing jet instability on vortex ring formation. *Physics of Fluids 12* (2000), 589–596.

[64] Zhou, J., Adrian, R. J., Balachandar, S., and Kendall, T. M. Mechanisms for generating coherent packets of hairpin vortices in channel flow. *Journal of Fluid Mechanics 387* (1999), 353–396.